QUANTUM CRITICALITY IN CORRELATED METALS, A GRÜNEISEN PARAMETER STUDY

Cover powered by Beatriz Zorzo Talavera
bezt architecture

A full color version of this document is available at
http://www.science.uva.nl/research/cmp/devisser/

Quantum criticality in correlated metals, a Grüneisen parameter study

ACADEMISCH PROEFSCHRIFT

ter verkrijging van de graad van doctor
aan de Universiteit van Amsterdam
op gezag van de Rector Magnificus
prof. dr. D. C. van den Boom
ten overstaan van een door het college voor promoties
ingestelde commissie,
in het openbaar te verdedigen in de Agnietenkapel
op donderdag 30 september 2010, te 10.00 uur.

door

Alessia Gasparini

geboren te Venetië, Italië

Promotiecommissie:

Promotor:	Prof. dr. M. S. Golden
Co-promotor:	Dr. A. de Visser
Overige leden:	Dr. J.-S. Caux
	Dr. N. H. van Dijk
	Prof. dr. P. Gegenwart
	Prof. dr. T. Gregorkiewicz
	Prof. dr. K. Schoutens

Faculteit der Natuurwetenschappen, Wiskunde en Informatica

The author can be reached at
a.gasparini@nki.nl

The research reported in this thesis was carried out at the Van der Waals-Zeeman Institute for Experimental Physics, University of Amsterdam. Some of the experiments have been carried out in the University of Karlsruhe, Germany, and in the High Field Magnet Laboratory of Nijmegen. The work was part of the research program of the Stichting voor Fundamenteel Onderzoek der Materie (FOM), which is financially supported by the Nederlandse Organisatie voor Wetenschappelijk Onderzoek (NWO).

Taliato da sotto, da questa nuova prospettiva, l'ulivo gli parse più grande e più intricato. Vide la complessità di ramature che non aveva prima potuto vedere standoci dintra.

A. Camilleri

Turn off your TV. Can you say brainwashing?

SOAD

to my family

Table of Contents

Symbols and Abbreviations

Latin symbols

c	specific heat
E_{F}	Fermi energy
T_{K}	Kondo temperature
T_{C}	Curie temperature
T_{sc}	superconducting transition temperature
k_{B}	Boltzmann constant
R	gas constant

Greek symbols

α	coefficient of linear thermal expansion
β	coefficient of volume thermal expansion
Γ	Grüneisen ratio
Δ	energy gap
ε	dielectric constant
Θ_{D}	Debye temperature
κ	compressibility
λ	magnetostriction coefficient
ν	critical exponent
ξ	correlation length
ρ	resistivity
τ	correlation time
ψ	wave function
χ	susceptibility
ω	frequency
z	dynamical exponent

Abbreviations

QCP	quantum critical point
QPT	quantum phase transition
PM	paramagnetism
AFM	antiferromagnetism
FM	ferromagnetism
SC	superconductivity
BCS	Bardeen-Cooper-Schrieffer
SDW	spin density wave
SCFM	superconducting ferromagnet
HTSC	high temperature superconductor
RKKY	Ruderman-Kittel-Kasuya-Yosida
FL	Fermi liquid
nFL	non-Fermi liquid
HF	Heavy fermion
CEF	crystalline electric field
RRR	residual resistance ratio
ZF	zero field

1 Introduction

In correlated metals the electron-electron interactions are not negligible, as it is instead assumed in the Fermi gas model used to describe the (nearly) free electrons in metals. Electrons in correlated metals are successfully described by the Fermi liquid (FL) theory, based on the concept of quasi-particles [1, 2, 3, 4]. Nevertheless at a quantum critical point (QCP) the FL description breaks down and the system shows a so-called non-Fermi liquid (nFL) behaviour. QCPs, which form an intriguing novel topic in the field of correlated metals, are phase transitions that take place at $T = 0$. These are driven by quantum fluctuations rather than by thermal fluctuations, as in the case of a classical phase transition. A system can be driven to a QCP by tuning a non-thermal control parameter such as pressure, magnetic field or doping. Theoretical models of QCPs are based on the idea that static and dynamic of the order parameter couple at the QCP [5, 6, 7]. The classical description of a phase transition in terms of critical fluctuations is still valid for the quantum case if $d + z$ dimensions are considered, where d is the physical dimension of the system while z, the dynamical critical exponent, accounts for the dynamics (Hertz-Millis model).

The most studied quantum phase transitions (QPTs) in correlated metals involve magnetism. Most of these metals are Ce, Yb or U based systems (mainly heavy fermions (HFs)) [8] where the itinerant magnetism is due to the f-electrons and the QCP is caused by a competition between Kondo screening and the Ruderman-Kittel-Kasuya-Yosida (RKKY) interaction [9]. In this simple picture, the magnetic order is suppressed when the local f-moments Kondo screening by the conduction electrons becomes dominant compared to the RKKY f-moments long-range interaction; which is mediated by the conduction electrons as well. The suppression of the magnetic order leads to the observation of nFL behaviour in transport and thermal properties. Experimental proof of the Hertz-Millis type of QCP has been reported in the literature for correlated metals [4, 10, 11]. For instance, $CeNi_2Ge_2$ is a nFL

compound where the resistivity data indicate the system is in the close vicinity of a QCP [12]. The specific heat divided by the temperature presents a strong increase below 6 K and nFL behaviour over one decade in temperature [13], consistent with the Hertz-Millis predictions for itinerant 3D spin density wave (SDW) fluctuations at a zero-field antiferromagnetic (AFM) QCP.

Although the Hertz-Millis theoretical model is well established as a good description of quantum criticality, some compounds have shown deviations from the model. The most interesting ones reported [14] are $YbRh_2Si_2$, in field [15, 16] and with Ge-doping [17, 18], and $CeCu_6$ doped with Au [4]. In $YbRh_2Si_2$ the (already low) AFM transition temperature is suppressed to zero by applying a small external magnetic field [16]. In parallel, by replacing Si with Ge, an AFM QCP is reached with much smaller magnetic field [17]. The comparison of the two QCPs allowed to exclude the critical behaviour is an artefact due to the external magnetic field. The resistivity at the doping driven QCP is linear in temperature up to 8 K [17], demonstrating the robustness of the non-Fermi liquid behaviour up to two decades in temperature. Although the specific heat presents evidence of a bulk 'itinerant' QPT [19], the temperature dependence of the bulk susceptibility and the nuclear magnetic resonance (NMR) spin-lattice relaxation rate cannot be explained with this model [20]. The case of $CeCu_{6-x}Au_x$ attracted much attention as well because of the unexpected results. While $CeCu_{6-x}Au_x$ exhibits 3D AFM ordering, specific heat and resistivity data are not consistent with such a scenario [4]. Moreover inelastic neutron scattering indicates quasi-2D critical fluctuations [21], but the fractional exponent in the neutron E/T scaling cannot be explain with a 2D SDW picture [22]. These examples highlight the need of a new framework when the Hertz-Millis model of quantum criticality (so-called 'itinerant' quantum criticality) breaks down. A new model, so called 'local' quantum criticality, is proposed [22]. To compare it with the classical criticality and the Hertz-Millis quantum criticality models, where the critical fluctuations extend in space for the former and in space and time for the latter, the local quantum criticality model considers critical fluctuations of the order parameter in time but not in space.

A powerful detection tool for quantum criticality is the Grüneisen ratio, which is proportional to the ratio of the thermal expansion over the specific heat, $\Gamma \propto \beta/c$. It has been shown that the Grüneisen ratio diverges at any QCP, regardless of the type of quantum criticality [23]. When the control parameter is fixed and the temperature is changed, the temperature exponent of $\Gamma \propto T^{-\nu z}$ provides important information regarding critical exponents of the system, such as the correlation length critical exponent ν and the dynamical critical exponent z. These exponents characterize the QCP: while ν provides

the spatial degree of correlation, z gives the temporal one. The divergence of the Grüneisen ratio has been experimentally proved for several compounds. For instance, it has been shown that the Grüneisen ratio diverges for both $CeNi_2Ge_2$ and $YbRh_2Si_2$ [13]. While the divergence of the former compound shows $\nu z = 1$, as predicted for a Hertz-Millis type of QCP, the latter presents $\nu z < 1$, consistent with a scenario where local critical excitations coexist with critical spin fluctuations [20].

Even more intriguing is the observation that the zero temperature instabilities influence the electronic properties of non-zero temperature phases, as observed in the case of unconventional superconductivity (SC). According to the standard model of superconductivity (Bardeen, Cooper and Schrieffer, BCS), superconductivity is due to conduction electrons that form a two electron system (quasi-particle) called Cooper pair, due to an attractive interaction mediated by the lattice. The two electrons forming a Cooper pair have anti-parallel spin and zero angular momentum (spin-singlet state). An unconventional (or non s-wave) superconductor is a system that cannot be described by the standard BCS model. An intriguing example of unconventional superconductivity is the triplet superconductivity, as discovered in UGe_2 in 2000 [24, 25]. In the past decade three similar systems have been discovered: URhGe [26, 27], UIr [28] and UCoGe [29]. In these systems the superconducting phase is formed in the presence of ferromagnetic (FM) order, hence the name superconducting ferromagnets (SCFMs). Since the presence of an internal magnetic field obstruct the formation of anti-parallel spins of the Cooper pair, SCFMs are described in terms of electron pairs with parallel spin (spin-triplet state) [30]. Moreover, the electron pairing is believed to be mediated by the exchange of longitudinal ferromagnetic spin fluctuations, which are enhanced in the vicinity of a QCP. Other examples of unconventional superconductivity are found amongst the HF systems. Superconductivity with a non-phononic pairing mechanism is observed in materials like $CeCu_2Si_2$ [31] and $CeCu_2Ge_2$ [32]. The discovered of SC in $CeCu_2Si_2$ at ambient pressure was recently linked to the presence of a 3D SDW AFM QCP at very low pressure for the Ge-doped system [33]. The proposed superconducting glue in this case are the quantum critical spin density wave fluctuations [14]. A last example of unconventional SC, more related to technological applications of superconductivity, are the high temperature superconductors (HTSCs), such as the cuprates [34] or the iron pnictides [35, 36]. For both cuprates and pnictides, the study of pressure and doping phase diagrams uncovered the presence of QCPs in close relation to the high temperature SC phases. Experiments provided evidence of unconventional d-wave superconductivity, as for instance showed by the symmetry of the superconducting gap function. Although great effort is devoted to the

study of these systems, the pairing mechanism in the HTSCs is still an open issue, where the most likely scenario is a spin density wave pairing mediation.

In this thesis the thermal properties of specific systems, such as correlated metals presenting AFM or FM quantum critical points, are studied. The Grüneisen ratio is used to characterize these systems. The thermal properties of an unconventional superconductor, close to a FM QCP, are also reported.

In *chapter 2* a brief overview of the current literature regarding QCPs and unconventional superconductivity is described. The classical vs. quantum phase transition case is discussed, together with the relevant aspect of models for superconducting ferromagnetic systems.

In *chapter 3* the experimental techniques used during this thesis work are reviewed and their implementation is presented. Cryogenics techniques down to 30 mK are combined with resistivity, ac-susceptibility, specific heat and thermal expansion measurements methods. In particular, the parallel-plate capacitor dilatometry technique is discussed and the calibration of the dilatometer is presented down to low temperatures ($\sim$ 30 mK).

In *chapter 4* the case of an AFM QCP is considered. In the heavy fermion system $CeRu_2Ge_2$ AFM is suppressed when Ru is replaced by 76 at.% Fe [37]. Inelastic neutron scattering experiments revealed that the Ce moments, responsible for the AFM, become increasingly shielded by the conduction electrons when lowering the temperature. This results in a long-range incommensurate magnetic order at low temperatures [37]. Nevertheless it was proved that the random fluctuations change the overlap between conduction electrons and local moments and this causes part of the moments to survive down to the lowest temperature and others to be fully shielded. Such a behaviour differs from the Hertz-Millis type [6] and from the local moment model [22] and a new scenario is proposed in ref. [37]. It is therefore extremely interesting to use the Grüneisen ratio in order to study the critical exponents, ν and z, of the $Ce(Ru_{0.24}Fe_{0.76})_2Ge_2$ system. As AFM order was still present in the sample, a magnetic field is applied along the easy axis to suppress AFM and the thermal properties in field are studied, in a similar way as was previously done for $YbRh_2(Si,Ge)_2$ [17].

In *chapter 5* an itinerant FM QCP is studied using the Grüneisen parameter. The unconventional superconductor URhGe [26] presents a 3D FM SDW QCP when doped with 38 at.% of Ru (critical concentration) [38]. This offers the opportunity of studying one of the few ferromagnetic systems with evi-

dence of a Hertz-Millis type of quantum criticality. The thermal properties of several polycrystalline samples of the U(Rh,Ru)Ge series are reported in order to study the evolution of the Grüneisen ratio towards quantum criticality. Particular attention is given to a single crystalline sample $URh_{0.62}Ru_{0.38}Ge$ prepared at the critical concentration for suppression of FM order. The thermal properties and the Grüneisen ratio of the single crystal at the critical concentration are studied in order to characterize the nature of the quantum criticality.

Chapter 6 focuses on the recently discovered superconducting ferromagnet UCoGe [29]. Experimental evidence allowed to conclude that this system presents unconventional triplet SC [29, 39]. Experiments on Si-doped samples [40] and under hydrostatic pressure [41, 42] revealed the presence of FM and SC QCPs, supporting the hypothesis that SC is mediated by FM spin fluctuations, enhanced in the vicinity of the QCP. The thermal expansion measurements reported in this chapter are the first to prove bulk SC in polycrystalline as well as in single crystalline samples. Moreover, thermal expansion measurements of single crystalline samples of UCoGe in applied magnetic field are carried out in order to study the bulk response to field of FM and SC along the crystallographic axes.

2 Theoretical aspects

Nossignori. Per me, io sono colei che mi si crede!

L. Pirandello

In this chapter a brief review of the present literature describing quantum phase transitions (QPT) and their associated quantum critical points (QCPs) [4, 14, 43, 44, 45] is presented, together with the theory proposed by Zhu *et al* [23] on the divergence of the Grüneisen ratio at the QCP. Since spin fluctuations, enhanced at the QCP, are considered to be the glue for unconventional superconductivity, the state of the art of these scenario's are reviewed as well.

2.1 Introduction

Several thermodynamic quantities are presented in the succeeding chapters. In the following section we shall concentrate on several different contributions present in the specific heat and in the thermal expansion, since these will be used to discern the non-critical contributions in the quantum critical regime. The Landau theory for classical phase transitions and an overview of the Ehrenfest relation are presented as well.

2.1.1 Specific heat

The thermal contribution of a crystal lattice is well described by the Debye model [46]. The model considers the collective vibrations of the lattice (phonons) up to a cut-off frequency ω_{D}. ω_{D} is defined as the frequency at which the total number of states, with density $Z(\omega)$, is equal to $3sN$ with N the Avogadro's number and s the number of atoms per formula unit. The De-

bye temperature is then defined as $\Theta_D = \hbar\omega_D/k$, where k_B is the Boltzmann constant. In solids Θ_D is typically of the order of 200-400 K.

For an isotropic material the internal energy in the Debye model takes the following form:

$$E(T) = E_0 + 9Nsk_BT\left(\frac{T}{\Theta_D}\right)^3 \int_0^{\Theta_D/T} \frac{x^3 dx}{e^x - 1}. \tag{2.1}$$

where E_0 is the zero point contribution to the internal energy. The Debye temperature Θ_D is:

$$\Theta_D = \frac{\hbar c}{k_B}\left(\frac{6\pi^2 Ns}{V}\right)^{1/3} \tag{2.2}$$

where V is the molar volume and c= ω/k is the propagation speed in the medium of the phonons with wave vector k and frequency ω. The specific heat per molar volume c_{lat} is then derived by taking the derivative of E with respect to the temperature:

$$c_{lat}(T) = 9Nk_Bs\left(\frac{T}{\Theta_D}\right)^3 \int_0^{\Theta_D/T} \frac{x^4 e^x dx}{(e^x - 1)^2} \tag{2.3}$$

At low temperatures, when $T \ll \Theta_D$, the integral can be solved expanding its upper limit to infinity, providing an expression for the lattice contribution to the specific heat:

$$c_{lat}(T) = \frac{12\pi^4}{5} Nk_Bs\left(\frac{T}{\Theta_D}\right)^3 \tag{2.4}$$

This is in good agreement with experimental data [47, 48]. Such a description alone fails at very low temperatures, where the contribution of the conduction electrons becomes important. At very low temperatures the Fermi distribution around the Fermi energy E_F drops more rapidly to zero and the electrons need less energy to hop to an unoccupied state. A bigger number of electrons can therefore absorb thermal energy. The contribution of the electrons to the specific heat is linear in temperature:

$$c_{el}(T) = \frac{\pi^2}{2} Nsk_B \frac{T}{T_F} \tag{2.5}$$

where $T_F = E_F/k$ is the Fermi temperature. The specific heat of solids at low temperatures presents therefore a T^3-term due to the lattice contribution and a T-term due to the electronic contribution:

$$c(T) = \gamma T + \beta T^3 \tag{2.6}$$

where $\gamma = \pi^2 N s k_B / 2T_F$ and $\beta = 12\pi^4 N k_B s / 5\Theta_D^3$. Deviations from this behaviour are observed for metals which are not well described by the free electron model, such as magnetic metals [46].

The behaviour of a metal in a magnetically ordered state can be described by magnons. Similarly to the phonon, the magnon is a quantized bosonic particle that represents the propagation of the spin oscillation around its zero temperature value. Since magnons have the same distribution as phonons, the same Debye model can be applied, giving for the heat capacity:

$$\text{FM} \qquad C_M = s_f R \left(\frac{k_B T}{2JS}\right)^{3/2} \tag{2.7}$$

$$\text{AFM} \qquad C_M = s_{af} R \left(\frac{k_B T}{2J'S}\right)^{3} \tag{2.8}$$

where s_f and s_{af} depend of the lattice structure, S is the spin, J and J' are the magnitudes of the exchange interaction. In the case of strongly anisotropic materials, a gap could open in the energy spectrum because of the interaction of the charge distribution and the crystalline electric field (CEF). This gives an additional exponential factor:

$$\text{FM} \qquad C_M \propto T^{3/2} e^{-\Delta/k_B T} \tag{2.9}$$

$$\text{AFM} \qquad C_M \propto T^{3} e^{-\Delta/k_B T}. \tag{2.10}$$

where Δ is the energy gap. Several of the systems close to a QCP are heavy fermion (HF) systems [8]. Heavy fermions are materials with an enhanced electronic mass m^*, due to the high density of states at E_F. For these systems the electronic specific heat has the same expression as the one of the free electron gas but with an enhancement of the coefficient of electronic specific heat γ. In fact the specific heat is one of the most important experimental quantities to determine whether a system is a HF since the enhanced electron mass is directly reflected in γ.

2.1.2 Thermal expansion and Grüneisen ratio

The thermal expansion coefficient quantifies the tendency of solids to change their volume V with a change of the temperature T at constant pressure p. Thermodynamically the coefficient of volume thermal expansion is:

$$\beta = \frac{1}{V}\left(\frac{\partial V}{\partial T}\right)_p \tag{2.11}$$

Experimentally and in case of a solid, it is more straightforward to measure the coefficient of linear thermal expansion:

$$\alpha = \frac{1}{L}\left(\frac{\partial L}{\partial T}\right)_p \tag{2.12}$$

where L is the linear dimension of the solid, and subsequently to add up the values along three perpendicular directions obtaining $\beta = \sum_i \alpha_i$, where i indicates one of the three orthogonal directions.

In order to describe the thermal expansion in a solid as a function of the temperature, it is useful to have a description similar to the one presented in the previous section for the specific heat. The model that led to eq. 2.1 is derived in the harmonic approximation. While this is a good approximation for the specific heat at low temperatures, it is not for the thermal expansion since the latter is dominated by anharmonic effects [47]. Indeed, in a rigorously harmonic crystal the coefficient of thermal expansion must vanish, since the pressure required to maintain a given volume does not vary with temperature.

Since the phonon frequency of a real crystal depends on the equilibrium volume, we need to make the occupancy of the normal mode with wave vector k in branch s dependent on the volume. We therefore introduce $n_s(k)$, defined as $n_s(k) = (e^{\hbar\omega_s/k_\mathrm{B}T} - 1)^{-1}$ in order to describe the contribution of the normal-mode ks to the thermal properties. Next we define the negative of the logarithmic derivative of the frequency of the mode ks with respect to the volume:

$$\Gamma_{ks} = -\frac{\partial(\ln\omega_s(k))}{\partial(\ln V)} \tag{2.13}$$

as the Grüneisen parameter for the mode ks and, weighting this last expression by the specific heat contribution for each normal mode $c_s(k)$, an overall quantity:

$$\Gamma = \frac{\sum_{k,s}\Gamma_{ks}c_s(k)}{\sum_{k,s}c_s(k)} \tag{2.14}$$

called the Grüneisen parameter. With these definitions, it can be shown that:

$$\beta = \frac{\Gamma c}{B} \tag{2.15}$$

where $B = 1/\kappa_\mathrm{T}$ is the bulk modulus, inverse of the compressibility at constant temperature $\kappa_\mathrm{T} = -1/V(\partial V/\partial p)_T$, and c the specific heat. In case of one relevant energy scale, the Grüneisen ratio is constant [47, 49]. Since B is only

weakly temperature dependent, $\beta(T)$ has the same temperature dependence as $c(T)$, which at very low temperatures results in:

$$\beta(T) = aT + bT^3 \tag{2.16}$$

As previously, the T-term is the electronic contribution while the T^3-term is the phononic contribution. The same estimation is valid in case the specific heat deviates from this description and other contributions are present. As in the case of the specific heat, the thermal expansion deviates from this description for HFs and magnetic materials. Since for each model a single energy scale is used, the thermal expansion still presents the same temperature dependence as the one for the specific heat.

The Grüneisen ratio defined in eq. 2.14 is rather cryptic. The Grüneisen ratio itself expresses the system's volume dependence to some external parameters, like temperature or magnetic field [50]. Intrinsically it gives an estimate of the dominant energy scale of the system: when Γ is constant to a characteristic value, this indicates that the system is described by a single energy scale.

2.1.3 Classical phase transitions

In order to describe a second order classical phase transition, the Landau description is used. In the proximity of the transition temperature T_c and assuming that the free energy F is analytical and an even function, F can be Taylor-expanded as:

$$F = \alpha\Phi^2 + \frac{\beta}{2}\Phi^4 + O(\Phi^6) \tag{2.17}$$

where Φ is the order parameter characteristic of the transition under investigation. Since the symmetry of the system breaks once it undergoes a phase transition, the order parameter is used for a thermodynamical description with symmetry considerations. This validates our assumption of a symmetric free energy function F. In the disordered phase the order parameter is zero but its fluctuations are non-zero. The order parameter fluctuations are described in terms of field theory (called Φ^4-theories). In the ordered phase, for $T < T_c$, the order parameter Φ is a finite quantity. Examples of order parameters are the magnetization for ferromagnetism or the energy gap function for superconductivity [46, 47].

In addition, the correlation function contains other important information [51]. Especially it provides the correlation length ξ, that represents a sort of spatial memory of the system and gives the spatial level of correlation of the order parameter. Similarly the correlation time $\tau_c = \xi^z$ gives the temporal

level of correlation of the order parameter and is related to ξ through the dynamical exponent z. The typical energy scale associated with the order parameter fluctuations is $\hbar\omega_c$, where $\omega_c \propto 1/\tau_c$. The correlation length diverges at the critical temperature as:

$$\xi \sim |t|^{-\nu} \tag{2.18}$$

where ν is the critical exponent associated to the correlation length and $t = |(T - T_c)/T_c|$ measures the distance from the critical point situated at T_c. As the correlation length, and consequently the correlation time, diverges at the phase transition, the typical energy scale goes to zero (critical slowing down).

It is important to notice that, for a classical phase transition, the kinetic and the potential part of the Hamiltonian H commute, therefore the partition function Z factorizes $Z_{cl} = Z_{kin}Z_{pot}$. This indicates that in a classical system static and dynamic decouple and that a classical phase transition can be studied using effective time-independent theories. Moreover, since close to the transition the correlation length is the only relevant energy scale, the physical properties do not change if a rescaling with a common factor is applied. This gives the homogeneity relation for the singular part of the free energy f for a system in d dimensions and for a given scale factor b:

$$f(t, B) = b^{-d} f(tb^{1/\nu}, Bb^{y_B}) \tag{2.19}$$

where B is the field conjugate to the order parameter and $y_B > 0$ is a critical exponent [44, 52, 53].

2.1.4 Ehrenfest relation

In a system the maximum usable thermodynamic energy is given by the Gibbs free energy G [51]. When the systems incurs a thermodynamic transformation, G changes as the work exchanged by the system with its surroundings, minus the work of the pressure forces, giving[1]:

$$dG = -SdT + Vdp \tag{2.20}$$

where S is the entropy. The Gibbs free energy is used to characterize the phase transitions. At a phase transition, $dG = 0$. The order of the transition is then defined by the order of the lowest derivatives of G that are discontinuous at

[1] For the sake of completeness, $dG = -SdT + Vdp + \sum_i \mu_i dN_i + \sum_i X_i da_i$ where μ_i and N_i are the chemical potential and the number of particles of the i-component and X_i an external forces working on the a_i parameter of the system. In the presence of a magnetic field B and with exchange of particles between the one component system and the environment, we consider $dG = -SdT + Vdp + \mu dN - MdB$, where M is the magnetization of the system.

the transition temperature. We classify phase transitions as first order when the first derivatives of G are discontinuous. We classify phase transitions as second order when the first derivatives of G are continuous, while the second derivatives are discontinuous. In the case of a second order phase transition, since the first derivatives of G are continuous and therefore the Clausius-Clapeyron relation [54] cannot be applied, the Ehrenfest relation is used:

$$\frac{dT_{\mathrm{C,s}}}{dp} = \frac{\Delta\alpha V_{\mathrm{m}}}{\Delta(c_{\mathrm{p}}/T_{\mathrm{C,s}})} \tag{2.21}$$

where V_{m} is the molar volume, $T_{\mathrm{C,s}}$ is the Curie or the superconducting transition temperature, $\alpha = V^{-1}(\partial V/\partial T)_p$ is the linear coefficient of thermal expansion and $c_{\mathrm{p}} = T(\partial S/\partial T)$ is the molar specific heat at constant pressure. The Ehrenfest relation is derived by expanding the infinitesimal entropy change dS in terms of T and p

$$dS = \left(\frac{\partial S}{\partial T}\right)_p dT + \left(\frac{\partial S}{\partial p}\right)_T dp$$

and considering that the entropy changes above and below the transition are equal ($dS_1 = dS_2$), together with the use of the Maxwell relations.

2.2 Quantum criticality

The renormalization theory with critical exponents is a well established model to describe classical phase transitions [51, 55]. Different phenomena such as the evaporation of water at its critical pressure and the demagnetization of iron when its temperature is raised have an universal description [45]. The same degree of universality is wished to be obtained for their quantum counterpart, the so called quantum phase transitions (QPTs).

QPTs are phase transitions that take place at $T = 0$ (see fig. 2.1). They are controlled by a non-thermal external parameter r such as pressure or magnetic field. Since at $T = 0$ the thermal fluctuations are negligible, the phase transition at r_{c} is driven by quantum fluctuations associated with Heisenberg's uncertainty principle. The classical description of the phase transitions in terms of correlation function remains valid with the exception that $t = (r - r_{\mathrm{c}})/r_{\mathrm{c}}$. For pressure induced QCPs $r = p$, while $r = H$ for a QCP induced by magnetic field tuning. Therefore the correlation length diverges as:

$$\xi \sim |t|^{-\nu} \tag{2.22}$$

and the correlation time τ as ξ^z. In contrast to the classical case, at the quantum phase transition the kinetic and potential parts of the Hamiltonian do

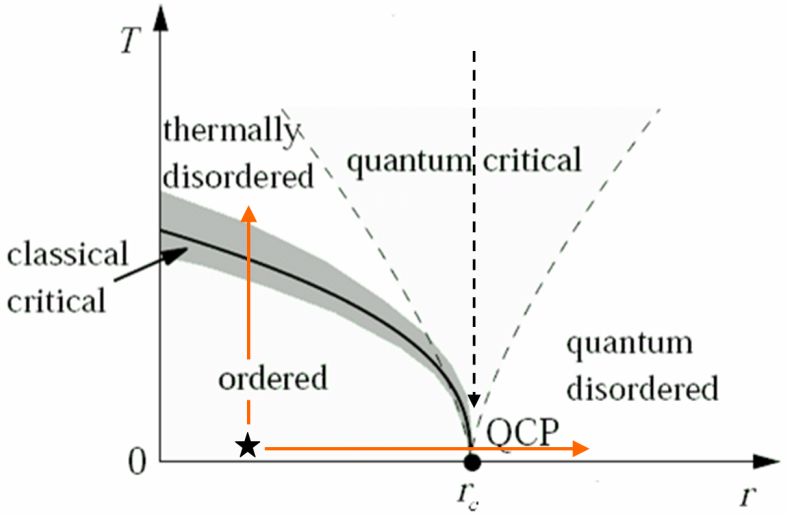

Figure 2.1: Sketch of the $T - r$ phase diagram in the vicinity of a QCP for a material with an ordered phase. The horizontal axis r represents the control parameter used to tune the system through the quantum phase transition, while the vertical axis T is the temperature. The solid line marks the finite-temperature boundary between the ordered and (thermally) disordered phase. Next to this line (gray region) the critical behaviour is classical. The classical transition temperature T_c is suppressed by tuning r and the QPT takes place at r_c. At $\star$ the ordered phase can be escaped by both increasing the temperature (vertical solid arrow) and changing the control parameter (horizontal arrow). For $T > T_c$ a thermally disordered state is reached, while for $r > r_c$ a quantum disordered state is reached. For $r \sim r_c$ and $T > 0$ a region of quantum criticality is present, where both thermal and quantum fluctuation are important [56, 57]. Here the dashed arrow indicates the most common experimental probing method, when $r = r_c$ and the temperature is varied. Picture adapted from refs. [4, 44].

not commute, which implies that the partition function $Z = \mathrm{Tr} e^{-H/k_\mathrm{B}T}$ does not factorize. At a QCP statics and dynamics are coupled. By introducing an imaginary time direction $-i\Theta/\hbar = \tau = 1/k_\mathrm{B}T$, where Θ is the real time, the canonical density operator $e^{-H/k_\mathrm{B}T}$ in the partition function looks like a time evolution operator in imaginary time τ. The classical homogeneity function (eq. 2.19) can then be rewritten for the quantum case as:

$$f(t, B) = b^{-d+z} f(tb^{1/\nu}, Bb^{y_B}). \tag{2.23}$$

The introduction of an imaginary time dimension permits to describe a quantum phase transition in d space dimensions as its classical counterpart in $(d + z)$ space dimensions. The dynamical properties of the quantum system are characterized by a fundamental time scale, the phase coherence time τ_ϕ, which has no classical counterpart [43]. Since τ_ϕ diverges when $T \to 0$ for all parameter values, the quantum system has perfect phase coherence even in the disordered phase [44].

It is natural to ask how quantum mechanics influences the asymptotic critical behaviour for $T > 0$ [4, 44]. Two energy scales have to be compared: $\hbar\omega_\mathrm{c}$, the typical energy scale of the long-distance order parameter fluctuations, and $k_\mathrm{B}T$, the thermal energy of the system. Quantum mechanics will be important as long as $\hbar\omega_\mathrm{c} >> k_\mathrm{B}T$, while when the thermal energy is larger than $\hbar\omega_\mathrm{c}$ the description will be purely classical. This brings the (also experimentally) important conclusion that quantum criticality can be studied not only by varying the control parameter r at $T = 0$ but also at $r = r_\mathrm{c}$ by varying the temperature, since in the quantum critical region both thermal and quantum fluctuations are important (see fig. 2.1). In fact in the region at r_c and at $T \neq 0$ the system looks critical but is driven away from criticality by the thermal fluctuations [44, 57].

2.2.1 Quantum phase transitions in fermion systems

Here we briefly discuss the proposed scenario for bulk quantum phase transitions taking place in fermion systems. We consider bulk quantum phase transitions, where the degrees of freedom of the whole sample become critical at the transition, as a model for our systems. In the model we deal with 'clean' systems, where translational invariance is unbroken and quenched disorder is absent [4, 44]. This is not always the case for real system, but the effect of disorder is possibly not dominant.

The general description of a quantum phase transition in Fermi liquids (FLs) was initially a study of the ferromagnetic QPT using the renormalization group method [5]. Subsequently this work was extended and it is now known as the

Hertz-Millis theory (for so-called 'itinerant' QCPs) [6]. The description presented in the previous section is used to describe spin-density wave transitions (SDW scenario), with only one type of critical degree of freedom, the long-wavelength fluctuation of the order parameter. More specific, a QCP exists due to the competition between the Kondo effect and the RKKY interaction, made explicit by the Doniach diagram [9]. In addition, the predicted behaviour of the principal properties of the system (such as specific heat and resistivity) were evaluated by Moriya [7].

This description for the 'conventional' phase transition appeared nevertheless to fail in some cases [45, 58] (e.g. in the case of $CeCu_6$ doped with gold [4]). The scientific community reacted with different opinions. Some said that the model could be saved if the complexity of the materials was taken into account, others tried to see it as a failure of Hertz's theory while there were those who sought for a new framework for these materials [45]. As for the last option, a new microscopic model (local quantum criticality) was presented [22]. This model considers local degrees of freedom instead of long-wavelength fluctuation of the order parameter. The effect of the quantum fluctuations (dynamics) is to couple the fermionic bath to the fluctuation of the magnetic field. On a macroscopic point of view, and as a comparison with the previously discussed scenarios, next to the classical criticality (which is a growth of global order in space) and the Hertz's theory of quantum criticality (which includes the imaginary time dimension), local quantum criticality considers growth in time but not in space [45]. Unfortunately a general quantitative prediction of most of the experimental quantities for local quantum criticality is not yet available. Nevertheless the model predicts a fractional exponent in the ϵ/T scaling in neutron scattering (which followed from the case of $CeCu_{6\text{-}x}Au_x$ [22]) as well as in the Grüneisen diverging function (as we see in the next equation 2.25) [59].

2.2.2 Grüneisen ratio at the quantum critical point

The Grüneisen ratio gives an estimation of the energy scale E^* that dominates in a certain temperature range. When a system is in the temperature range where an effect (as for instance phononic vibrations or magnetic fluctuations) dominates, specific heat $c(T)$ and thermal expansion $\alpha(T)$ present the same temperature dependence. Hence the Grüneisen ratio $\Gamma(T)$ is constant with a value typical of the dominant energy scale. A common case is the Grüneisen ratio of a solid at high temperatures ($T \sim \Theta_D$), when $\Gamma = 2$ [49] due to the phonon dominant energy scale ($E^* = E_D$).

Such a regular dependence is obtained assuming that there is a single energy scale present in the system. In the quantum critical regime an energy scale

vanishes, as mentioned in sec. 2.1.3. It has been shown that therefore the Güneisen ratio diverges at every QCP [23]. Here we present the main steps of ref. [23]. As discussed in the first part of sec. 2.2, the regime of quantum criticality is achievable at $T \to 0$ varying the control parameter r, or at $r = r_c$ lowering the temperature T towards zero (see fig. 2.1). Accordingly, when pressure is the control parameter, the Grüneisen ratio diverges as:

$$\Gamma_{cr}(T \to 0, r) = -G_r \frac{1}{V_m(p - p_c)} \tag{2.24}$$

and

$$\Gamma_{cr}(T, r = r_c) = -G_T T^{-1/\nu z} \tag{2.25}$$

where ν, the critical exponent of the order parameter, and z, the dynamical exponent, are defined in the previous section 2.2. The pre-factor G_T is a function containing non universal parameters as T_0 and p_c and G_r is a function of only the critical exponents ν and z and the dimensionality d. Eqs. 2.24 and 2.25 follow from the scale invariance presented in eq. 2.23 (for the detailed derivation see ref. [23]). It is important to notice that the power law of the $\Gamma(T)$ divergence in eq. 2.25 provides important information, giving νz when α and c are measured as a function of the temperature.

Only pre-factors are needed to correct eqs. 2.24 and 2.25 when doping, the so-called chemical pressure, is used as control parameter. This is true only if doping x and pressure p can be quantitatively related as $(p - p_c) = c(x - x_c)$. If pressure is replaced by an external magnetic field H, the magnetocaloric effect $(\partial M/\partial T)_H$ has to be considered instead of α in calculating Γ, giving:

$$\Gamma_{H,cr}(T \to 0, r) = -G_r \frac{1}{H - H_c} \tag{2.26}$$

Again, in the $T \to 0$ limit, the pre-factor G_r is universal. The T dependence of H_{cr} at $r = r_c$ is given by eq. 2.25 as well.

As discussed in ref. [23], scaling is applicable under certain conditions:

i Sometimes non-critical contributions can dominate, like in the case of a AFM SDW QCP (see tab. 2.1). Since the divergence pertains to the critical contribution $\Gamma_{cr} \sim \alpha_{cr}/c_{cr}$, the critical component has to be carefully discerned from the other components.

ii The scaling ansatz used in ref. [23] to derive $\Gamma_{cr}(T, r)$ is valid below the upper critical dimension ($d + z < 4$ in the Φ^4 theories). At the upper critical dimension, logarithmic corrections to scaling arise. Above the upper critical dimension, the scaling argument can be spoiled by the presence of so-called 'dangerously irrelevant operators'.

iii At the QCP more than a single diverging time scale can be present. This can indeed lead to a breakdown of simple scaling relations [60]. In this case more scaling dimensions have to be considered in order to result in a divergence of the Günesein ratio.

In ref. [23] the case of SDW QCPs is widely discussed, since many magnetic materials presenting QCPs are itinerant ferromagnets and these are mainly systems above the upper critical dimension. We refer to this paper for a more detailed description. The results for $\alpha_{\rm cr}(T)$, $c_{\rm cr}(T)$ and $\Gamma_{\rm cr}(T)$ at $r = r_{\rm c}$ are presented in tab. 2.1. In the following chapters we analyse one system with d=3 and z=2 (AFM QCP in $Ce(Ru,Fe)_2Ge_2$, chap. 4) and one system with d=3 and z=3 (FM QCP in U(Rh,Ru)Ge, chap. 5). In fig. 2.2 we present the behaviour $\Gamma_{\rm cr}(T)$ for d=3 and z=3, in order to simplify the description in chap. 5. In the plot three curves are shown. These curve represents $(T^{2/3}\log(T_0/T))^{-1}$, where T_0 is the temperature where the logarithmically diverging function of the specific hear is predicted to be zero. In all three curves the same T_0 is used. Note that we are interested only in the temperature range $T \ll T_0$, e.g. where the predicted function for the critical specific heat $c_{\rm cr} > 0$. In this temperature range $\Gamma_{\rm cr}(T)$ has a minimum at $T_{\rm min} = T_0 e^{-3/2}$.

	d=2 z=2	d=2 z=3	d=3 z=2	d=3 z=3
$\alpha_{\rm cr} \sim$	$\log\log(1/T)$	$\log(1/T)$	$T^{1/2}$	$T^{1/3}$
$c_{\rm cr} \sim$	$T\log(1/T)$	$T^{2/3}$	$-T^{3/2}$	$T\log(1/T)$
$\Gamma_{\rm cr} \sim$	$\frac{loglog(1/T)}{Tlog(1/T)}$	$T^{-2/3}\log(1/T)$	$-T^{-1}$	$(T^{2/3}\log(1/T))^{-1}$

Table 2.1: Theoretical prediction for the SDW QCPs in the quantum critical regime $r - r_{\rm c} \ll T^{2/z}$. Table adapted from ref. [23].

2.3 Superconducting ferromagnets

Up to now, four superconducting ferromagnets (SCFMs) have been discovered. These are listed in table 2.2 together with several of their characteristic parameters. As the name suggests, SCFMs become superconducting in the ferromagnetic phase. Their superconductivity is unconventional, i.e. it cannot be described by the standard Bardeen, Cooper and Schrieffer (BCS) model [64].

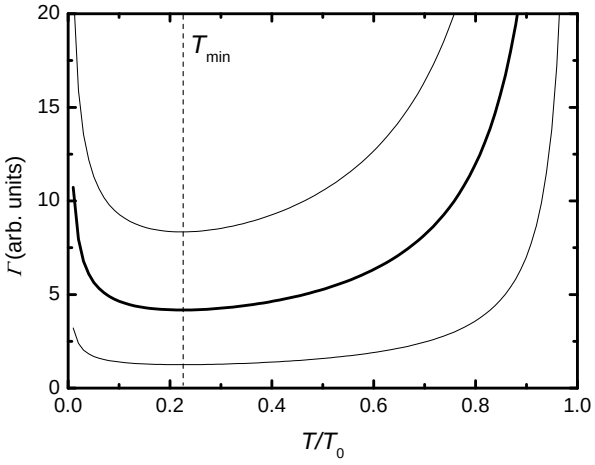

Figure 2.2: Predicted behaviour of $\Gamma_{\rm cr}(T)$ (d=3 and z=3) for $T \to 0$ and $r = 0$. The thick solid line represents $\Gamma = (T^{2/3}\log(T_0/T))^{-1}$. The top line represents 0.5Γ, while the lower line represents 2Γ. The horizontal axis is normalized to T_0. The vertical asymptote of the function is at $T = T_0$ and the vertical dashed line indicates $T_{\rm min}$.

In the BCS model, two electrons with energy $E \sim E_{\rm F}$ and with antiparallel spins form a state (Cooper pair) under the influence of an attractive force due to lattice vibrations. A two-electron system can have $S = 0$ or 1 and $L = 0$, 1, 2, 3, ... The Cooper pair is a quasi-particle with quantum numbers that are superpositions of the electrons quantum numbers and obeys the Pauli principle. Since the wave function is shown to be antisymmetric, it has to be formed by a combination of odd-spatial part and even-spin part or vice versa. It could therefore be in a spin-singlet state ($S = 0$) represented as:

$$\phi_s = \frac{1}{\sqrt{2}}\left(|\uparrow\downarrow\rangle - |\downarrow\uparrow\rangle\right) \tag{2.27}$$

with $L = 0$ (s-wave) or $L = 2$ (d-wave), or in a spin-triplet state ($S = 1$) represented as:

$$\phi_t = \begin{cases} |\uparrow\uparrow\rangle & \text{(ESP)} \\ \frac{1}{\sqrt{2}}\left(|\uparrow\downarrow\rangle + |\downarrow\uparrow\rangle\right) & \\ |\downarrow\downarrow\rangle & \text{(ESP)} \end{cases} \tag{2.28}$$

with $L = 1$ (p-wave) or $L = 3$ (f-wave) and where ESP denotes the equal-spin pairing states. A standard Cooper pair has $S = 0$ and $L = 0$. Every

	structure	T_C (K)	T_{sc} (K)	p_c (kbar)	m_0 (μ_B/U atom)	γ (J/mol K^2)
UGe_2 [24, 25]	orthorhombic	53	0.8[a]	16.5	1.5$\|a$	0.032
URhGe [26, 27]	orthorhombic	9.5	0.25	-	0.42$\|c$	0.160
UIr [28, 61, 62]	monoclinic	45	0.1[b]	24	0.50$\|$[10-1]	0.049
UCoGe [29, 39, 42]	orthorhombic	3	0.6	14	0.07$\|c$	0.057

Table 2.2: List of superconducting ferromagnets, in order of discovery, together with their characteristic parameters. T_C and T_{sc} are the FM and SC transition temperatures, respectively, while p_c is the critical pressure for suppression of FM, m_0 is the ordered moment and γ is the Sommerfeld coefficient of the electronic specific heat. For a description of those materials one should refer to ref. [63] or directly to the original references reported in the table.

[a] At a pressure of 1.2 GPa
[b] At a pressure of 2.7 GPa

material that presents superconductivity with electron pairing having $S \neq 0$ and $L \neq 0$ is called a non s-wave or an unconventional superconductor. Another peculiarity of unconventional SC is that the energy gap function has a lower symmetry than the Fermi surface (and therefore of the crystal lattice). Unconventional superconductivity has been found in several materials in the last forty years, by instance in ^{3}He [65, 66], heavy fermions [31, 67, 68, 69, 70, 71, 72, 73, 74, 75] and high temperature superconductors (HTSCs) (cuprates [34] or the recently discovered iron pnictides [35, 36]).

2.3.1 Coexistence of superconductivity and itinerant ferromagnetism

Since a magnetic field destroys conventional superconductivity, as magnetic impurity atoms do, the standard BCS theory cannot describe the coexistence of magnetism and SC. Therefore the superconductivity in the SCFMs should be non s-wave. Nevertheless, around 1980, several compounds presented competing superconducting and antiferromagnetic ground states (as for instance the HF SC UPt_3 [72, 73]) and it was theoretically recognized that under special conditions SC may coexist with AFM. In this case the AFM electron spins arrange themselves in an antiparallel configuration, hence the singlet pairing is still possible. Around the same time, ESP states were theoretically predicted for superconductivity in itinerant ferromagnets (p-wave SC) [30], with the pairing interaction mediated by the exchange of longitudinal spin fluctuations. Twenty years later, this prediction was experimentally confirmed with the discovery of high pressure SC in the ferromagnetic UGe_2 [24, 25]. Although the pairing glue of unconventional SC is still an open issue, the low-

energy excitations known as spin fluctuations seem to be the best candidate.

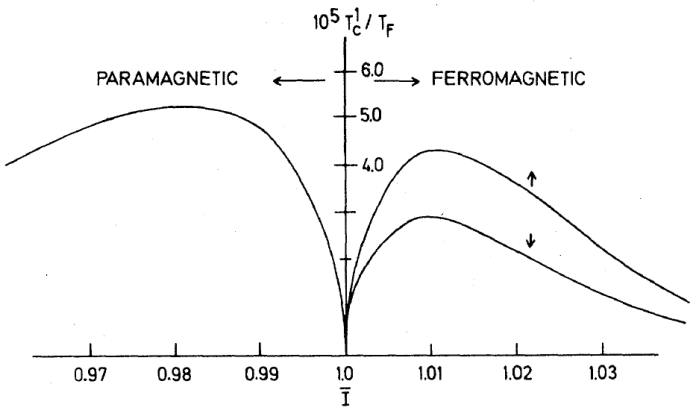

Figure 2.3: The p-wave superconducting transition temperature $T_{\rm sc}$ as a function of the Stoner parameter $\bar{I}$, in the paramagnetic (PM) and ferromagnetic (FM) phases. $T_{\rm sc}$ is scaled and normalized by the Fermi temperature $T_{\rm F}$. The arrows indicate the spin up ($\uparrow$) and spin down ($\downarrow$) phases as the relative ESP superconducting transition takes place. Picture taken from ref. [30].

In the scenario of ref. [30] the same electrons are responsible for both SC and FM that coexist near to a FM QCP. The magnetic behaviour is described by a mean-field theory in terms of a Hubbard exchange parameter $\bar{I}$ and a Stoner enhancement factor $S = (1 - \bar{I})^{-1}$. Fig. 2.3 describes the prediction of the model for the superconducting transition temperature $T_{\rm sc}$ in the PM as well as in the FM region as a function of the exchange parameter $\bar{I}$. In this model superconductivity is destroyed at the FM QCP, while it appears both in the paramagnetic (PM) ($\bar{I} < 1$) and in the FM ($\bar{I} > 1$) phases. $T_{\rm sc}$ for the spin up and spin down states is predicted not to be the same, although this has not yet been experimentally observed. Whether both phases are present depends sensitively on the details of the band structure. The model predicts that SC would reappear in the PM phase and, in the absence of a magnetic field, all three components of ϕ_t would have the same $T_{\rm sc}$. The SC phase in the PM region has not been experimentally observed yet. In the case of UGe_2 and UIr, a possible explanation is that in the FM phase the ferromagnetic spin waves (magnons) couple to the longitudinal magnetic susceptibility, which enhances the SC transition temperature to values experimentally available [63, 76]. The description in fig. 2.3 leads to the generic phase diagram presented in fig. 2.4 (left panel).

For UCoGe under pressure, the experimental phase diagram [42] consis-

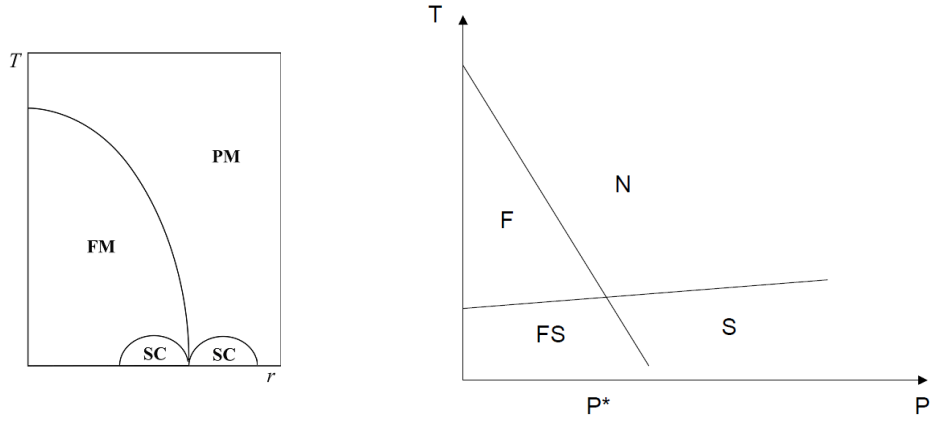

Figure 2.4: [left] The generic phase diagram for a SCFM as follows from the model presented in ref. [30]. SC appears at the left and right sides of the QCP. In the left lobe, SC coexists with FM. The right SC lobe has never been experimentally observed. Picture adapted from ref [76]. [right] Schematic pressure-temperature phase diagram of the superconducting ferromagnet UCoGe [77]. N is the normal paramagnet phase, F is the ferromagnet phase, S is the paramagnet superconducting phase and FS is the multi-domain ferromagnet superconducting phase. All the lines represent second-order phase transitions

tently differs from the theory proposed by ref. [30]. When pressure is applied, FM is suppressed at p_c. Interestingly the SC transition temperature not only is enhanced but also remains non-zero for $p > p_c$ (in the PM phase). For higher pressure SC is depressed. With symmetry considerations, ref. [77] presents a theoretical model where the behaviour of UCoGe is compared to the case of ^{3}He and explained in terms of two band superconductivity with triplet pairing. The model is schematically presented in fig. 2.4 (right panel). In a two band FM the superconducting state is still believed to be formed by either spin-up electrons from one band or by the spin-down electrons from the other band [78]. An analysis of the free energy F shows that T_C should decrease when magnetic field is applied perpendicular to the direction of the spontaneous magnetization (as for T_{sc} [39]) [79].

3 Experimental methods

[...] le loro idee camminano sulle nostre gambe

This chapter is dedicated to the description and discussion of the experimental techniques used during the thesis work. All the samples have been prepared and measured in Amsterdam, at the van der Waals-Zeeman Institute. They have been characterized by means of back-scattering Laue diffraction, EPMA (Electron Probe Micro-Analysis), electrical resistivity and ac-susceptibility. Thermal expansion, magnetostriction and specific heat have been investigated. In addition, low temperature specific heat (at the University of Karlsruhe, Germany) and high field magnetoresistance (at HFML, Nijmegen) measurements have been carried out.

3.1 Cryogenics techniques

To perform measurements at low temperatures, several cryostats have been used:

A home-made ^{4}He bath cryostat (the so called glass-dewar system, since the liquid N_2 and ^{4}He reservoirs are made of glass) in the temperature range 2 - 300 K. A thermal expansion insert can be fitted in this cryostat for operation in the temperature range 2 - 200 K. The temperature is controlled by a carbon-glass thermometer and a manganin wire as heater.

A ^{3}He refrigerator, Heliox VL (Oxford Instruments) [80], in the temperature range 0.23 - 15 K with a 14 T superconducting magnet. At the tail of the insert, a multi-purpose sample platform is mounted: at this level the temperature is controlled by a RuO_2 thermometer and a heater

(manganin wire). Both the thermometer and the heater are connected to an ORPX resistance bridge (Barras Provence). Resistivity, magnetoresistance, ac susceptibility, thermal expansion and magnetostriction measurements are reported.

A ^{3}He/^{4}He dilution refrigerator, Kelvinox MX100 (Oxford Instruments) [81], in the temperature range 30 mK - 1 K with an 18 T superconducting magnet and a field compensation coil at the level of the mixing chamber. A multi-purpose sample platform is mounted with a temperature control set-up (thermometer-heater) like the one used in the Heliox. In this thesis, thermal expansion and magnetostriction measurements carried out in this cryostat are performed.

A dewar with a home-built ^{3}He refrigerator for specific heat measurements down to 0.5 K with a 17 T superconducting magnet [82]. The temperature is measured with a special parallel resistor as thermometer with a very low field dependence [83]. The cryostat is a closed ^{3}He system with a storage gas vessel at room temperature T_{room} and a cryopump for evaporative cooling.

A bottom loading ^{3}He/^{4}He dilution refrigerator (University of Karlsruhe, Germany) for specific heat data in the range $0.10 < T < 1$ K in small applied magnetic fields.

The Heliox and Kelvinox inserts are controlled by LabVIEW [84] programs provided by Oxford Instruments. To integrate these instrument controls, additional LabVIEW programs have been written to implement resistivity (and magnetoresistance), susceptibility and thermal expansion (and magnetostriction) data acquisition. In the thermal expansion programs, communication between the different instruments and automatic stabilization of the temperature have been implemented.

3.2 Sample preparation

All the samples in this thesis have been prepared in Amsterdam at the van der Waals-Zeeman Institute (WZI, UvA) using high purity elements (3N for U, Rh and Ru, 4N for Co and 5N for Ge). We used natural Uranium (Goodfellow) for the U(Rh,Ru)Ge samples and depleted Uranium (Brunswick) for the UCoGe samples.

The polycrystals are prepared in a home built mono-arc furnace. The chamber is evacuated to a pressure of 10^{-7} mbar after which the melting process takes place in an argon atmosphere of 0.5 bar. The samples are molten and

flipped several times to increase the homogeneity. The sample mass is typically 3-4 g.

The single crystals are grown by Dr. Y. K. Huang using the Czochralski method in a tri-arc furnace, from a polycrystalline batch of $\sim$ 15 g. The single crystallinity is checked using X-ray back-scattering Laue diffraction. The same technique is afterwards used to orient the single crystalline samples. The incident beam is WL_α radiation with wavelength $\lambda = 1.4801$ Å and the back scattered X-ray is recorded on films Polaroid 57.

Different sample shapes are obtained using an AGIEPLUS spark erosion machine with a position accuracy of 5 μm. Bars and cubes are cut by use of a conductive wire (copper saw). The opposite surfaces of the cubic samples are then made plane parallel (for thermal expansion experiments) using a rotating disk passing over the surface. For the resistance measurements the surface defected by spark erosion is removed by polishing (the final polishing is made with a grinding disc of 800 μm). The typical dimensions are $1 \times 1 \times 5$ mm^3 for the bars and $5 \times 5 \times 5$ mm^3 for the cubic samples.

The U(Rh,Ru)Ge (only for the polycrystalline samples) and UCoGe samples are wrapped in Ta foil and annealed in evacuated water free quartz tubes ($p = 10^{-7}$ mbar) using different annealing procedures to improve the sample quality. All the U(Rh,Ru)Ge polycrystalline samples were annealed under high vacuum in quartz tubes for 10 days at 875 °C. The UCoGe single crystals were annealed at temperatures between 850 °C and 1250 °C, from one to three weeks (the details will be discussed in chapter 6).

The phase homogeneity and stoichiometry of the samples are investigated with Electron Probe Micro Analysis (EPMA). A JEOL JXA-8621 equipment present in the WZI has been used.

3.3 Sample characterization

The samples are characterized by means of electrical resistivity and ac susceptibility techniques. The resistivity is used to investigate the quality of the samples (via the residual resistance ratio, $RRR = R_{T_{\rm room}}/R_{1\ \rm K}$) and the superconducting and ferromagnetic properties for UCoGe samples. In $Ce(Ru,Fe)_2Ge_2$ and in U(Ru,Rh)Ge the resistivity technique is used to investigate the critical behaviour of the systems. The ac susceptibility technique has been used as a sensitive probe for magnetic ordering.

The resistivity of the samples is measured using a standard four point method (see fig. 3.1). The current and voltage leads are thin copper wires ($\varnothing = 30$ μm) of which one end is soldered to the contact point on the copper sample holder. The other end is connected to the sample using conductive

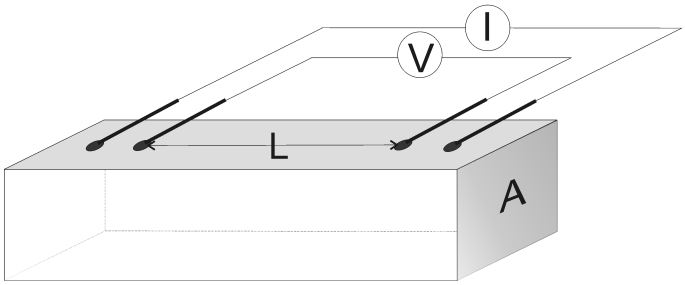

Figure 3.1: Schematic four point resistivity method. Typically the length **L** is a few mm (1.5 to 5 mm) and the area **A** is 1 mm^2. V indicates the wires where a voltage is applied while I indicates those where the current is measured. The total resistance of the sample is in the order of about ~ 10 mΩ.

silver paint. In this way a contact resistance of a few Ω can be achieved. This value is low enough to prevent Joule heating even at the lowest temperature ($P_J \sim 0.01$ μW, three order of magnitude smaller than the cryostat cooling power). Surface conditions like roughness or cracks can increase the contact resistance by one order of magnitude.

The resistance is measured in the temperature range 0.24-9 K using a Linear Research AC Resistance Bridge model LR700 operating at a frequency of 16 Hz and excitation currents of $30-100$ μA. The temperature is swept from ~ 9 K downwards at the rate 0.05 K/min. For magnetoresistance data, the field sweep rate is typically 0.02 T/min upwards and 0.05 T/min downwards.

The ac-susceptibility is measured with a mutual inductance transformer method [86]. A driving magnetic field $H_{\rm ac}$ is provided by a current in the primary coil, made of superconducting wire (see fig. 3.2). A current is induced in the secondary coils. The secondary coils are wound in opposite directions as to compensate the induced voltage. A sample can be placed in one of the two coils, destroying the balance: the voltage which is observed at the output of the coils, $V_{\rm ac}$, gives therefore a direct measure of the magnetization of the sample, $M_{\rm ac}$. The ac-susceptibility can be calculated from the driving field $H_{\rm ac}$ and the induced magnetization $M_{\rm ac}$ using:

$$M_{\rm ac} = \chi_{\rm ac} H_{\rm ac} sin(\omega t)$$

where $\omega = 2\pi f$ and f is the driving frequency [87]. In this thesis $\chi_{\rm ac}$ is measured with the LR700 bridge at a driving field in the order of 10^{-5} T and a fixed frequency $f = 16$ Hz.

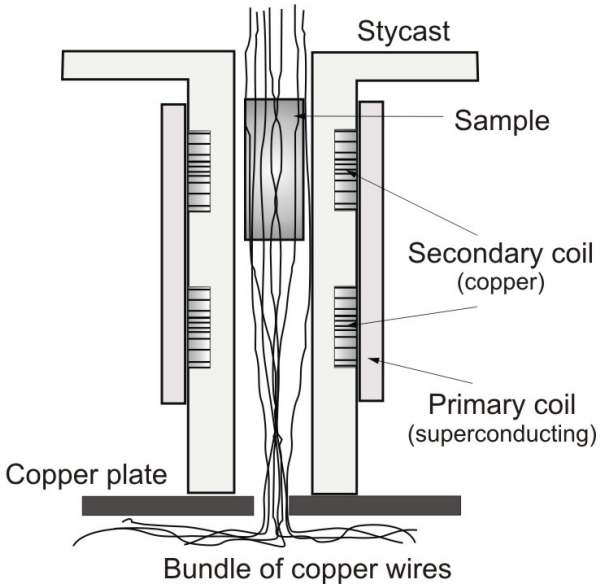

Figure 3.2: Schematic view of the mutual inductance transformer coil used in ac-susceptibility measurement. Picture taken from ref. [85].

3.4 Dilatometry

3.4.1 Thermal expansion

To measure the thermal expansion coefficient, we use a three terminal capacitance method [89]. A schematic drawing of the measuring principle is presented in fig. 3.3(a). The equivalent electronic circuit is in fig. 3.3(b): the measured capacitance is C_{12} and the other two grounded capacitances, C_{g1} and C_{g2}, are used to shunt the noise.

A simple relation connects the measured capacitance C and the gap distance d between the plates:

$$d = \frac{\varepsilon A}{C} \tag{3.1}$$

where $\varepsilon = \varepsilon_0 \varepsilon_r$ with ε_r the dielectric constant of the medium between the plates and A is the area of the plates.

The three terminal capacitance method is so far the most sensitive method to measure thermal expansion ($\Delta l/l = 10^{-10}$), better than optical methods (best sensitivity $\Delta l/l = 10^{-9}$) which have on their side a better accuracy [49] . Nevertheless, for thermal expansion, sensitivity is needed to detect the

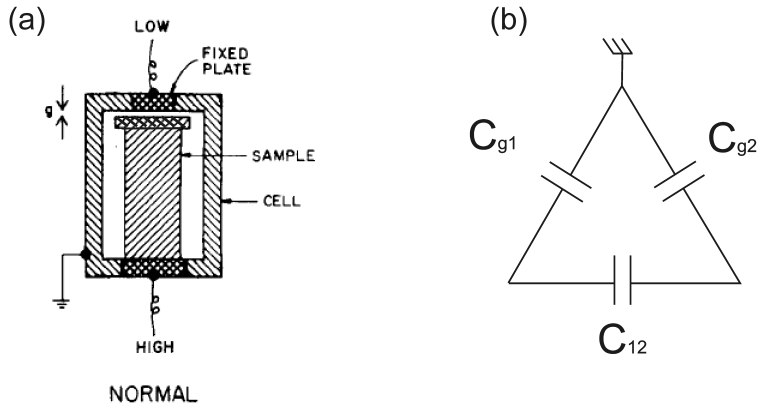

Figure 3.3: (a) Schematic drawing of the three terminal capacitance method in the normal configuration (from ref. [88]). The capacitance is measured between two plates (at LOW and HIGH voltage) with a gap distance g. The HIGH plate is connected to the sample. The body of the cell is connected to ground. (b) Equivalent circuit for the normal configuration [89]: C_{12} is the capacitance between plates in (a). C_{g1} and C_{g2} are shunt capacitances, from the plates to ground.

difference in gap distance more than the gap distance itself. The sensitivity of the cell varies proportional to the square of the distance between the plates as

$$\Delta d = -\frac{\varepsilon A}{C^2}\Delta C. \tag{3.2}$$

Using eq. 3.2 we can easily see that a big capacitance, for a fixed resolution of the bridge ΔC, allows to measure smaller values of Δd. On the other hand a big capacitance value implies less precision of the reading device. A compromise between these two different effects has been found for typical values of $C \sim$10 pF.

The cells used in this work employs the three-terminal capacitance method for a parallel-plate capacitor of area A (fig. 3.4). The cell, constructed of oxygen free high conductivity copper (OFHC Cu), was designed and made at the University of Amsterdam [90]. The distance d between the upper plate and the lower plate is determined by three copper spacers (6) with thickness in the order of 40-120 of μm (only one is shown in the figure). The upper plate (1) is fixed to the cell and isolated from the guard ring (5) by a thin layer of kapton (25 μm). The lower plate (2) is connected to a disk (8) by three rods (only one is shown), which pass through the bottom of the cell. The sample is clamped between the lower plate and the bottom of the cell by tightening a screw (4) which exerts a small force on the plate-like spring (9). In this way

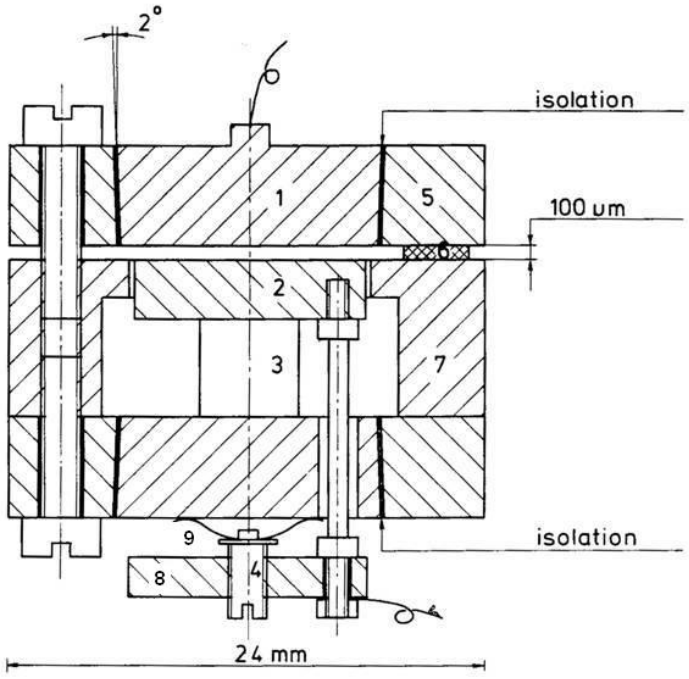

Figure 3.4: Schematic drawing of the Amsterdam cell. 1. upper plate 2. lower plate 3. sample 4. spring and screw 5. guard ring (upper plate) 6. copper foil 7. guard ring (lower plate)

a change of the sample length results in changes of the distance between the upper and lower plates and therefore a change of the capacitance value.

This kind of cell has the advantage that it is small (diameter 24 mm) and easy to mount in the cryostat. Moreover the shape of the sample is not crucial as long as there are two plane parallel surfaces. However, a drawback is that the sample length is fixed at 5 mm. For smaller samples this problem can be overcome by using a copper spacer to adjust the total length to 5 mm.

The capacitance is measured with an Andeen-Hagerling capacitance bridge. For this bridge a high stability is ensured by an oven controlled temperature of the reference capacitor. In the experiments in the Heliox and Kelvinox the model AH2500 is used, while for the experiments in the glass-dewar system the model AH2700A is used with a variable frequency option (50 Hz-20 kHz). For both models a 1 kHz-15 Volt configuration has been used. The nominal resolution for both bridges is 10^{-7} pF, the real resolution can be even one order of magnitude bigger (other noise sources, like remaining vibrations or

bad grounding). Therefore the wires have to be carefully connected to the sample platform. Using an averaging procedure (typically 60-120 sec) a $\Delta l/l = 2 \cdot 10^{-10}$ for a sample of 5 mm can be obtained. This enables us to measure length changes as small as 10^{-2} Å.

The cell is attached to the same sample platform which holds the thermometer and the heater. One cell is used for the Heliox and Kelvinox (cell-1), while a second cell is used in the glass-dewar system (cell-2). The effective value of εA was measured at room temperature for each cell, considering the dielectric constant in helium $\varepsilon_r \sim 1$. The effective value was determined from the slope of the capacitance C plotted as function of $1/d$, obtained by using copper foils of different thickness [50]. This experimental method overcomes errors due to stray capacitances assuming the area A as ideal. The values are $\varepsilon A = 9.73 \cdot 10^{16}$ Fm for cell-1 and $\varepsilon A = 9.45 \cdot 10^{16}$ Fm for cell-2 with an error of $\pm$ 3%.

The linear thermal expansion coefficient is defined as $\alpha = L^{-1}\Delta L/\Delta T$, where L is the length of the sample. α is measured using a step-wise heating method (glass-dewar system up to 20 K, Heliox up to 15 K and Kelvinox up to 1 K) as well as a continuous heating method (for the glass-dewar system, T > 10 K). For the step-wise method, steps of 10 mK up to 0.5 K have been taken. Specific LabVIEW software has been written to check for the stability of temperature and capacitance and to select the next temperature after the data point was recorded, for automatization of the process. In the case of the continuous method a typical rate of ∼10 K/h was used, i.e. slow enough to garantee that the temperature is homogenous over the system cell-thermometer. The volumetric thermal expansion coefficient is then calculated as $\beta = \sum_i \alpha_i$, with $i = a, b, c$ (the crystallographic cyrstal axes of single crystalline samples) or $i = x, y, z$ (the three orthogonal direction of the cubic polycrystalline sample[1]).

The thermal expansion coefficient of the sample is given by:

$$\alpha = -\frac{1}{L}\left(\frac{\Delta d}{\Delta T}\right)_{\text{cell+sample}} + \frac{1}{L}\left(\frac{\Delta d}{\Delta T}\right)_{\text{cell+Cu}} + \alpha_{\text{Cu}}. \tag{3.3}$$

The first term corresponds to a change of the gap distance with the sample mounted. The second term is the so called cell-effect, measured with a 5 mm copper piece in the cell instead of the sample: this term ideally measures the thermal expansion of the thin copper spacers (6), however it appeared that other contributions are present (see 3.4.2). The last term is the thermal expansion of copper [88], which corrects for the contribution from the walls of the cell.

[1] In principle just one direction of the polycrystal could be enough.

3.4.2 The cell effect

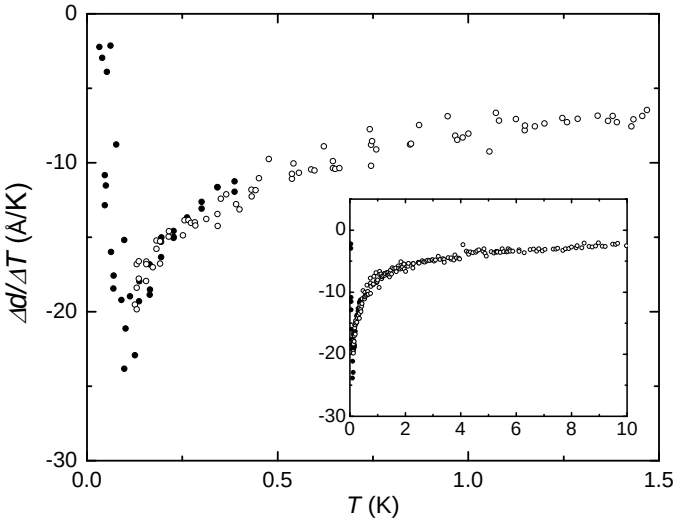

Figure 3.5: Cell effect for cell-1. The y-axis shows the change in gap distance with a change of the temperature, in Å/K: to calculate the cell-effect for the specific sample this value has to be divided by the sample length, with a proper conversion factor. The cell-effect becomes important at $T \leq 2$ K. A fit (not shown) is used to correct the data in the increasing part of the curve (0.1 K $< T <$20 K) while in the range 30 mK$< T <$ 100 mK the data themselves are interpolated to be subtracted from the raw data.

The origin of the cell effect is still quite puzzling but the effect is well reproducible and therefore a correction curve for both cells can be constructed (see fig. 3.5 for cell-1 and fig. 3.6 for cell-2). In the temperature range 5-150 K the correction due to the cell effect is in general small ($< 1\%$ of the $\alpha(T)$ of a typical sample). At high temperatures some irreproducibilities are found (near 220 K) which limits the use of the cell up to $\sim$ 200 K (typically 150 K). These irreproducibilities are likely related to the kapton in the cell, used to isolate the plates from the guard ring [91]. For $T \sim$1 K the correction becomes comparable to the $\alpha(T)$ of the sample. Surprisingly, upon lowering the temperature below 1 K, the cell effect shows a large pronounced minimum (at 100 mK, fig. 3.6). Also this effect reproduces well and the thermal expansion data reported in chapter 6 have been corrected for it.

The origin of the minimum is unclear, but possibly it is due to excitations in

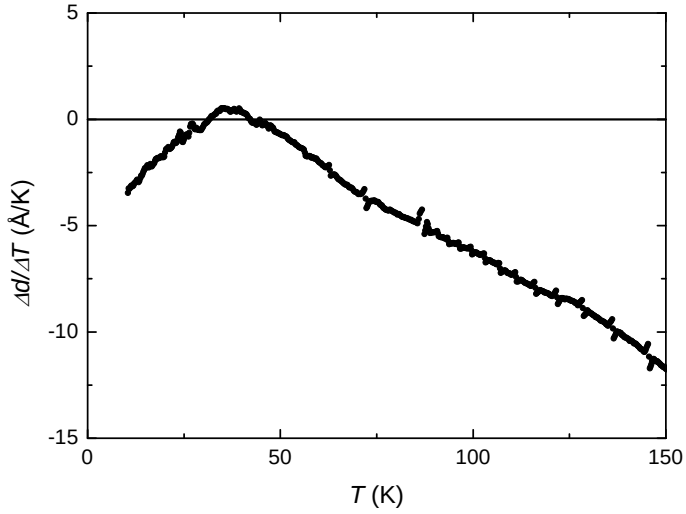

Figure 3.6: Cell effect for cell-2. Different effects are probably competing, considering the abrupt change around 30 K, where the cell effect is almost zero. To compensate for this cell effect, interpolated data are subtracted from the samples data sets.

a two level system (Schottky anomaly [46]). For the easiest case of a two levels system with energies ε_1 and ε_2 separated by an energy gap $\Delta = (\varepsilon_1 - \varepsilon_2)/k_{\mathrm{B}}$, the specific heat is:

$$c_{\mathrm{Sch}} = R\left(\frac{\Delta}{T}\right)^2 \frac{e^{\Delta/T}}{(1+e^{\Delta/T})^2} \tag{3.4}$$

where R=8.314 J/mol K is the gas constant. A similar behaviour applies for the thermal expansion. A magnetic field changes the energy gap Δ and therefore the contribution of the Schottky anomaly. A tentative comparison of the cell-effect with the Schottky anomaly is made in fig. 3.7, at low temperature and for $B = 0, 3$ and 5 T. The shape of the anomaly present in the data is similar to the predicted anomaly of a two level system for a temperature range that increases with the field, but the match between data and fit is not completely satisfactory which could suggest the presence of a multi level Schottky system [2]. This suggests that the fit of the data with a Schottky

[2]We could as well have made a kapton sample to be measured in the cell (see ref. [91] for high T data)

anomaly function could be correct but that maybe more than two levels are present.

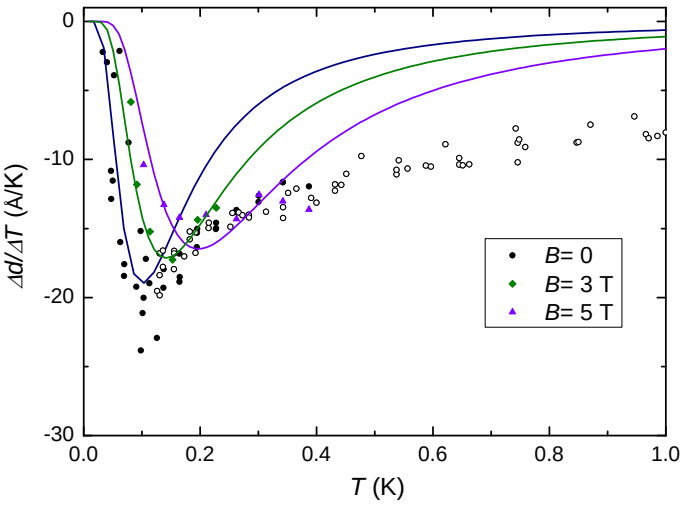

Figure 3.7: Cell effect at low temperature, in $B = 0, 3$ and 5 T. In the same color as the data, the Schottky fitting function for each data set. The temperature range where the data are well fit by the curve increases with the field.

3.4.3 Magnetostriction

The linear magnetostriction $\lambda = \Delta L/L$ is measured for a sample in the capacitance cell by slowly sweeping the magnetic field B and recording the change in capacitance. The magnetic field rate ($dB/dt = 0.05 - 0.02$ T/min) is slow enough for heating (due to the eddy currents) to be negligible. The coefficient of linear magnetostriction is denoted as $\tau = d\lambda/dB$. The cell effect in the magnetostriction data is negligible, having a contribution in the order of 10^{-8} (data not shown), from two to four orders of magnitudes smaller than the magnetostriction of the samples.

3.5 Specific heat

In the temperature range 0.5-50 K the specific heat is measured in the 17 T system, using a semi-adiabatic method. A heat pulse (providing a known amount of heat Q with a duration of 15-30 seconds) heats up the sample with

a temperature step ΔT. The heat capacitance is calculated as $C = Q/\Delta T$. The samples have a typical mass of 3 g and these are placed in a copper clamp in a gold-plated cold-rolled silver sample holder. The accuracy in the whole temperature range is 2% [92].

In the low temperature range 0.1-1 K, a heat pulse technique especially designed for small sample has been used [93]. The sample, with a mass of around 0.1 g, is placed on a Si plate which is heated with a short heat pulse ($0.01 - 0.1$ ms).

For both techniques, a correction for the sample holder was taken into account.

4 Field induced quantum criticality in $Ce(Ru,Fe)_2Ge_2$

Caterpillar: Who are you?
This was not an encouraging opening for a conversation [...]
"I ca'n't explain myself, I'm afraid Sir," said Alice, "because I'm not myself, you see."

L. Carroll

In this chapter we investigate the antiferromagnetic quantum critical point (AFM QCP) in the heavy fermion system $CeRu_2Ge_2$ when Ru is doped with 76 at.% Fe [37]. The parent compound $CeRu_2Ge_2$ was studied intensively, because it is a prominent member of the family of the Ce 1:2:2 compounds. Recently, doping studies in $CeRu_2Ge_2$ attracted attention, because of the possibility to induce a magnetic QCP. Neutron scattering experiments on $Ce(Ru_{0.24}Fe_{0.76})_2Ge_2$ demonstrated a peculiar type of quantum criticality, where both local and long-range fluctuations of the local moments are present, but only the latter are critical [22, 37]. Here we further investigate the quantum critical behaviour in $Ce(Ru_{0.24}Fe_{0.76})_2Ge_2$ by specific heat, thermal expansion and resistivity measurements. We study the thermal properties of a single crystalline sample $Ce(Ru_{1-x}Fe_x)_2Ge_2$ with the nominal concentration x_{cr}=0.76 [94, 95]. The presence of weak antiferromagnetic order in the sample ($T_N \sim 1.2$ K) gives the opportunity to focus on the field-induced AFM QCP: magnetoresistance and magnetostriction measurements are used to detect the transition from the AFM to a polarized state. Resistivity, specific heat and thermal expansion measurements are subsequently carried out in several magnetic fields ($B \leq 6$ T) and the behaviour in the ordered and in the polarized phases is analyzed.

4.1 Introduction

As a member of the Ce 1:2:2 family, the correlated metal system $CeRu_2Ge_2$ was already studied in the eighties. The physics of Ce-based compounds attracted much attention because of the discovery of unconventional superconductivity in $CeCu_2Si_2$ in 1979 [31]. The ground state of the Ce-based heavy fermion (HF) systems is generally determined by the hybridization phenomena of the local 4-f electrons interacting with the s, p or d electronic bands [96]. HF properties naturally arise from a Kondo resonance peak at the Fermi energy E_F [8].

Initially, $CeRu_2Ge_2$ was widely studied because of its similarities to $CeCu_2Si_2$ and the hope to find a second Ce-based heavy fermion superconductor [97]. Later, when no sign of superconductivity was found, $CeRu_2Ge_2$ attracted attention because of the suggestion that it could be driven to a state with strongly enhanced electronic effective masses by applying chemical or hydrostatic pressure [98]. The observation that $CeRu_2Ge_2$ is on the verge where the Kondo effect suppresses the RKKY interaction [99] let to detailed pressure and doping studies, as discussed further on.

$CeRu_2Ge_2$ belongs to the CeM_2X_2 family (where M is Cu, Ag, Au, Ru, or Ni and X is Si or Ge) just like the famous heavy fermion superconductor $CeCu_2Si_2$ [31] and the heavy fermion system $CeCu_2Ge_2$ [70, 71]. This Ce-based ternary family of compounds includes systems with very different ground states (some examples are listed in ref. [100]). $CeRu_2Ge_2$ crystallizes in the tetragonal $ThCr_2Si_2$ structure [101]. The conventional unit cell contains two formula units and the lattice parameters are $a = 4.256$ Å and $c = 10.000$ Å [99] (see fig. 4.1).

In early works on this system, specific-heat data taken on a sample with nominal composition $CeRu_{2.16}Ge_2$ show a phase transition peak below 10 K (with a weak shoulder on the high temperature side of the peak) and a Schottky-peak at around 220 K due to the crystalline electric field (CEF) splitting [71] (fig. 4.2 a, upper frame). A later neutron scattering study [99] yielded evidence for ferromagnetic (FM) order below T_C=7.5 K and a second weaker phase transition at T=8.5 K. The saturation moment amounts to 1.98±0.03 μ_B at 1.5 K and the ordered moment is aligned along the tetragonal axis [99, 102]. The high temperature peak in the specific heat is a measure of the CEF splitting of the ground state: in the tetragonal symmetry one expects the J=5/2 level of the Ce $4f^1$ state to split into three doublets. The entropy of the lowest doublet is fully accounted for by the value of Rln2 reached at 20 K (see fig. 4.2 a, lower frame). The Schottky anomaly at high temperature is well accounted for by the remaining two doublets at 500 K (total entropy

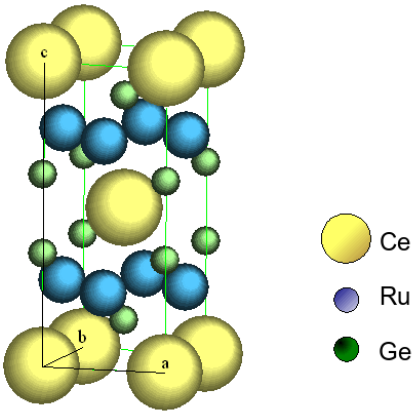

Figure 4.1: Tetragonal unit cell of $CeRu_2Ge_2$ ($ThCr_2Si_2$ structure [101]) with lattice parameters a=4.256 Å and c=10.000 Å [99].

Rln4) and 750 K (total entropy Rln6) [71] (see fig. 4.2 b).

Specific heat experiments [102] show that for a high-purity single-crystalline sample of $CeRu_2Ge_2$ the magnetic transition results in only one sharp anomaly at 7.91 K. This suggests that the secondary transition is present in low purity poly-crystalline samples only, although more recent studies still claim the presence of the second anomaly (the AFM order that will appear under pressure or doping [103]). The system is characterized by a small mass enhancement (γ=20 mJ/mol K^2), due to the low temperature magnetic order, and a Kondo temperature $T_K \sim 2$ K [99]. This means that the RKKY temperature T_{RKKY} is comparable with the Kondo temperature T_K and it places this compound in an interesting region of the Doniach diagram, as illustrated by fig. 3 in ref. [100]. The system is therefore in the heavy fermion regime close to nFL behaviour, which makes it a promising candidate to be tuned to a QCP by tuning a control parameter.

High pressure studies have been carried out on polycrystals [104, 105, 106] and single crystals [107, 108]. These studies reveal a complex phase diagram with FM and AFM phases and an AFM QCP at the critical pressure p_c=67.5 kbar [107]. For pressures $p > p_c$, the FL behaviour is slowly recovered. Resistivity measurements [107] show that the single-impurity Kondo temperature is never the dominant energy scale in the phase diagram. Here three different regimes can be discerned: (i) at low J the RKKY is dominant leading to local moment magnetism, (ii) for $J \sim J_c$ close to the QCP a Kondo-like moment

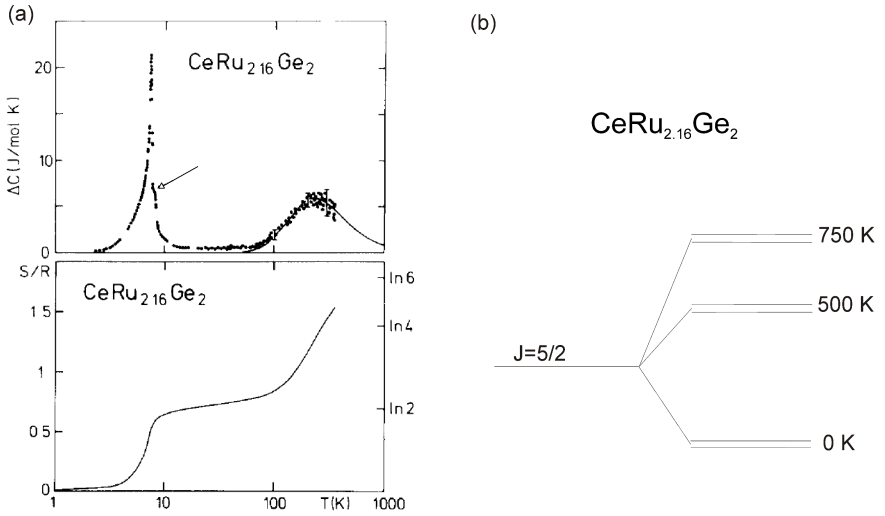

Figure 4.2: (a) Upper frame: electronic specific heat of $CeRu_{2.16}Ge_2$ [71]. The arrow indicates a weak secondary transition. The high temperature line represents the Schottky anomaly related to the CEF splitting (see text). Lower frame: entropy divided by gas constant S/R as a function of T. Figure adapted from ref. [71]. (b) J=5/2 level splitting in three doublets due to the crystal field [71].

compensation suppresses T_N, but for $J = J_c$ residual magnetic correlations are present resulting in enhancement of the effective mass, and (iii) at $J > J_c$ the system behaves as a Kondo lattice with a low effective mass [107]. Nevertheless T_K has been proved to increase while the magnetic order is suppressed [109].

The evolution of the magnetic state by doping has been widely studied as well, and can be compared with the phase diagram under pressure [94, 95, 107, 110]. For instance, in ref. [107], the phase diagram of $CeRu_2(Ge,Si)_2$ was found to be in good agreement with the pressure diagram of the pure compound. In ref. [94] the $p-T$ diagram of $CeRu_2Ge_2$ is compared with the effect of Fe-doping in $CeRu_2Ge_2$ (see fig. 4.3). The end compound $CeFe_2Ge_2$ is isostructural with $CeRu_2Ge_2$ and is a non-magnetic correlated metal with γ=270 mJ/mol K^2. In the Fe-doped compound, part of the Ru is replaced by Fe atoms, which are smaller, resulting in a positive chemical pressure on the Ce atoms [107].

Both tuning parameters result in an evolution from a FM to an AFM phase with an AFM QCP at the critical Fe concentration $x_c = 0.76 \pm 0.05$ in case of doping [94]. Inelastic neutron scattering (INS) studies on poly-crystalline samples in the AFM state (x=0.65), at the QCP (0.76), and in the FL regime

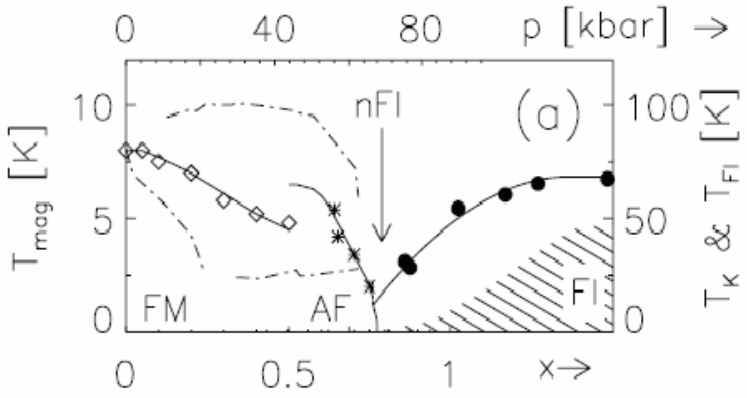

Figure 4.3: Magnetic phase diagram of $CeRu_2Ge_2$ versus pressure (upper axis, dashed lines) and of $Ce(Ru_{1-x}Fe_x)_2Ge_2$ (Fe-doping in the lower axis, empty diamonds: FM phase, stars: AFM phase). Filled circles give the pressure dependent T_K. The shaded part gives the pressure dependent FL region where the resistivity is $\propto T^2$. The solid lines are guides to the eye. See ref. [94] for Fe-doped data and ref. [107] for pressure data. Picture taken from ref. [94].

(0.87) [110] revealed a local moment magnetic response on the Ce-ions at high temperatures for all concentrations studied. Measurements of the samples at the QCP and in the FL regime showed that for both compositions the characteristic time scale on which the moments fluctuate increases inversely proportional to the distance to the critical point. The decay of the fluctuations is however quite different: exponential in time away from the QCP and non-single exponential at the QCP. It is not clear how to connect these to FL and nFL decay mechanisms.

Inelastic neutron scattering experiments on a single crystal prepared by Dr. Y. K. Huang (WZI) at the critical Fe concentration are reported in ref. [37]. The magnetic scattering at low temperature is shown in fig. 4.4 (left panel). This scattering was separated from the incoherent nuclear scattering and the weak background scattering by subtracting the signal at T=56 K from the signal at T=2 K. The results showed that, upon lowering the temperature at the QCP, the Ce moments become increasingly shielded by the conduction electrons. This results in a long-range incommensurate magnetic order at low temperatures, with a propagation vector (0,0,0.45) and an ordered moment of only $0.18\pm0.03\mu_B$/Ce. However, some moments survive down to the lowest temperature, while some others are fully shielded, due to the random fluctuation that changes the overlap between local moments and conduction electrons. In fig. 4.4 (right panel) we reproduce the new phase diagram pre-

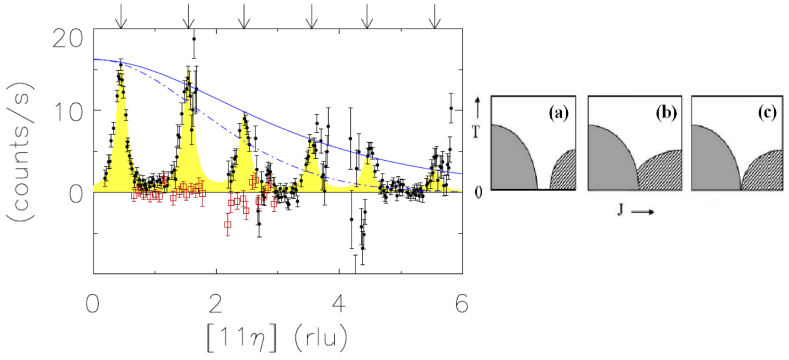

Figure 4.4: [left] Onset of incommensurate ordering at low temperature in a $Ce(Ru_{0.24}Fe_{0.76})_2Ge_2$ single crystal. The diffraction peaks are present only along [1 1 η] at the incommensurate positions [n n 2m±0.45] (indicated by the arrows at the top), with n and m natural numbers. No difference was observed along [0 0 η]. The solid line is the calculated magnetic intensity based on the cross section for neutrons and the Ce f-electron form factor [111], while the dotted line is calculated for the Fe d-electrons [112]. [right] (a) Suggested phase diagram for $CeRu_2Ge_2$ doped with Fe: the area between the regions where the moments order (gray) and where they are fully shielded (striped) is a region where some moments survive down to 0 K [37]. This phase diagram differs from the spin density wave [6] (b) and the local moment [22] (c) scenario. Both pictures are taken from ref. [37] and adapted.

sented in ref. [37] in order to explain this scenario: the area between the regions where the moments order and where they are fully shielded is a region where some moments survive down to 0 K [37]. This differs from the spin density wave [6] and the local moment [22] scenario diagrams.

4.2 Thermal properties of $Ce(Ru_{0.24}Fe_{0.76})_2Ge_2$

As part of a more detailed study of the QCP in $Ce(Ru_{0.24}Fe_{0.76})_2Ge_2$, measurements of the thermal properties and the Grüneisen ratio have been carried out. Thermal expansion and specific heat may shed light on the presence and amplitude of different electronic contributions. The Grüneisen ratio is predicted to diverge, under certain conditions, at every QCP [23] and it is therefore a powerful tool to detect quantum criticality and its features. Predictions are available for temperature variation of the Grüneisen parameter near an itinerant QCP [23], but not specifically for a local QCP [59]. From the response of the Grüneisen ratio at the QCP one could in principle tell whether quantum criticality in $Ce(Ru_{0.24}Fe_{0.76})_2Ge_2$ has an itinerant nature.

4.2.1 Specific heat

Unfortunately, the single crystalline sample used for the INS experiment (labelled #1) was not available and, therefore, a new single crystalline sample was grown with nominal concentration of Fe x_{Fe}=0.76 at the WZI by dr. Y.K. Huang. A part of this crystal was shaped into a cube for thermal properties measurements (sample labelled #2) with dimensions 5×5×5 mm^3. In fig. 4.5 we show the specific heat of sample #2 (mass 0.75 g) measured at the WZI and compare the data with the specific heat of sample #1 measured in Ann Arbor [112]. Clearly, the specific heat of sample #2 shows a maximum in c/T versus T at 1.2 K. No sign of such an anomaly is observed for sample #1. The two data sets start to deviate from each other at $T \sim 6$ K, but for $T < 1$ K the data sets level off to the same value of c/T indicating γ=0.8 J/mol K^2. The high mass enhancement, indicated by the high γ value present in both samples, indicates the proximity to a quantum critical point.

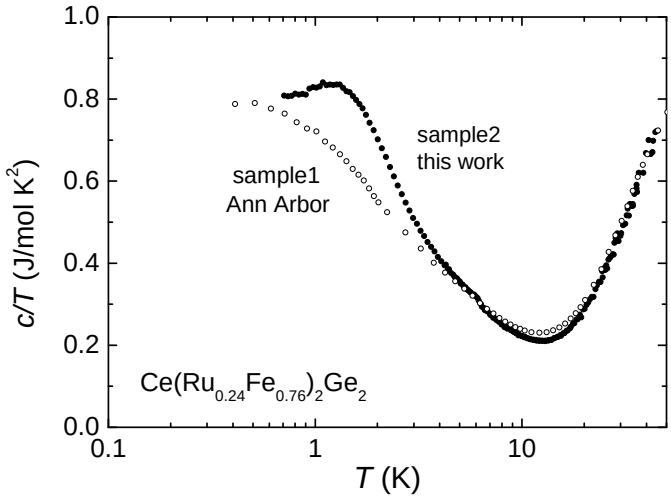

Figure 4.5: Specific heat divided by temperature as a function of the logarithm of temperature for $Ce(Ru_{0.24}Fe_{0.76})_2Ge_2$ sample #2 (filled symbols) and #1 [112] (open circles).

In fig. 4.6 we show the f-electron specific heat of $Ce(Ru_{0.24}Fe_{0.76})_2Ge_2$ sample #2 after subtracting the phononic contribution. The latter was estimated by measuring the specific heat of the non f-electron material $LaFe_2Ge_2$ [112, 113]. The specific heat of $LaFe_2Ge_2$ for $T < 150$ K can be described by

a Debye function with Θ_D=290 K. With this value we calculate a coefficient β of the low temperature T^3 phonon term $\beta = 3.97 \times 10^{-4}$ J/mol K^4 by using the relation (see sec. 2.1):

$$\beta = 5 \times \frac{12\pi^4 R}{5\Theta_D^3} \tag{4.1}$$

where $R = Nk_B$ is the gas constant. The coefficient γ_{La} of the linear electronic term is estimated as γ=0.043 J/mol K^2 (see dashed line in fig. 4.6). This value is of the same order of magnitude as the value reported in ref. [114]. The f-electron contribution of $Ce(Ru_{0.24}Fe_{0.76})_2Ge_2$ plotted in fig. 4.6 is derived as:

$$c_{el} = c - c_{lat}$$

where $c_{lat} = c_{La} - \gamma_{La}T$ is the estimate for the phonon contribution.

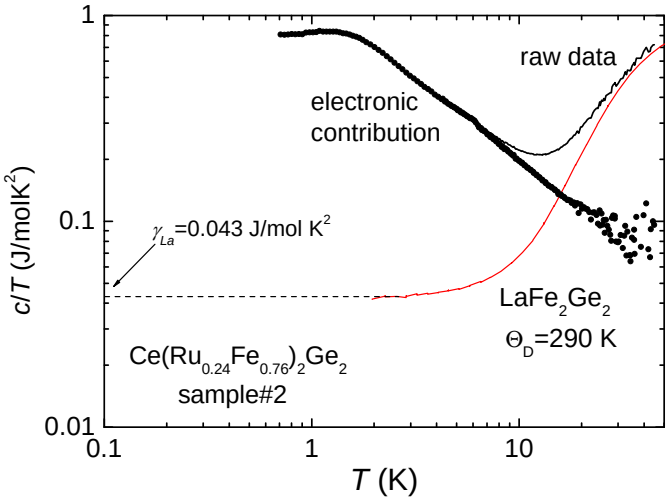

Figure 4.6: Electronic specific heat of $Ce(Ru_{0.24}Fe_{0.76})_2Ge_2$ sample #2 divided by the temperature (filled symbols) as a function of temperature in a log-log plot, obtained by subtracting the data of $LaFe_2Ge_2$ (thin solid line) from the raw data (solid line). The dashed line indicates the electronic contribution in $LaFe_2Ge_2$ with γ_{La}=0.043 J/mol K^2.

The data in figs. 4.5 and 4.6 show a large electronic contribution for $T < 10$ K. Considering, as discussed in sec. 6.1, that the second CEF doublet lies at an elevated temperature (Δ_{CEF}=500 K), the anomalous contribution is

a clear sign of the heavy fermion behaviour in samples with a Fe concentration near 76 at.%.

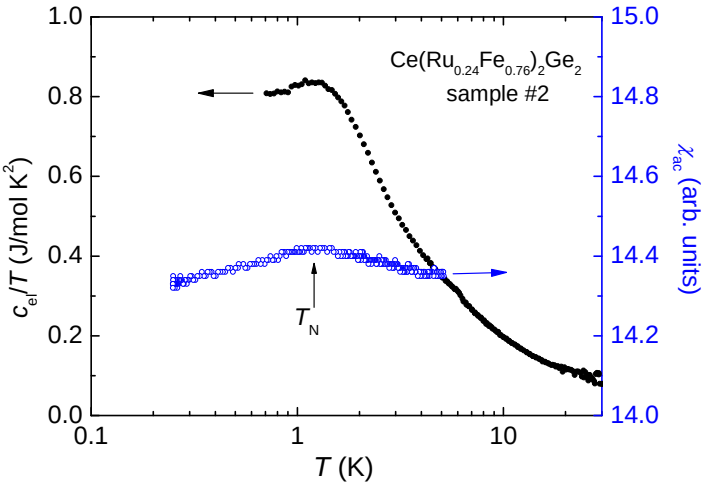

Figure 4.7: Electronic specific heat (filled symbols, left vertical scale) plotted together with $\chi_{ac}(T)$ (open circles, right vertical scale) to a logarithmic temperature scale. A weak maximum in both data sets is present for $T_N \sim 1.2$ K.

To investigate the nature of the low temperature anomaly in the specific heat of sample #2, the electronic contribution c_{el} is compared with ac-susceptibility data (fig. 4.7). The ac-susceptibility was measured on a bar shaped single crystalline sample of $Ce(Ru_{0.24}Fe_{0.76})_2Ge_2$, taken from the same large single crystalline piece as sample #2 was taken. The data are measured for a driving field H_{ac} along the c axis in the temperature range 0.24 K $< T <$ 5.5 K. Both c_{el}/T and χ_{ac} have a maximum at T=1.2 K, which tells us that the specific heat anomaly has a magnetic origin. Inspecting the phase diagram reported in ref. [94], we conclude that the AFM order is still present in the sample, and that the actual Fe-concentration of sample #2 is slightly lower than x_{nom}=0.76. From the phase diagram of $Ce(Ru,Fe)_2Ge_2$ and T_N=1.2 K we estimate $x \simeq 0.75$. Nevertheless, in the following we will refer to this sample by its nominal concentration: $Ce(Ru_{0.24}Fe_{0.76})_2Ge_2$ (sample #2).

4.2.2 Thermal expansion

The coefficient of linear thermal expansion was measured in the glass-dewar system along the three crystallographic axes and afterwards in the Heliox

system along the a and c axes. The data were taken on the same sample #2 as used in the specific heat experiments. The sample length amounted to ∼5 mm along all axes. Data have been taken in the range 0.25-150 K in two different experimental runs. The results for the coefficient of linear thermal expansion along the three crystallographic axes, α_a, α_b and α_c, are shown in fig. 4.8. In this figure we have also plotted the averaged value $\beta/3$.

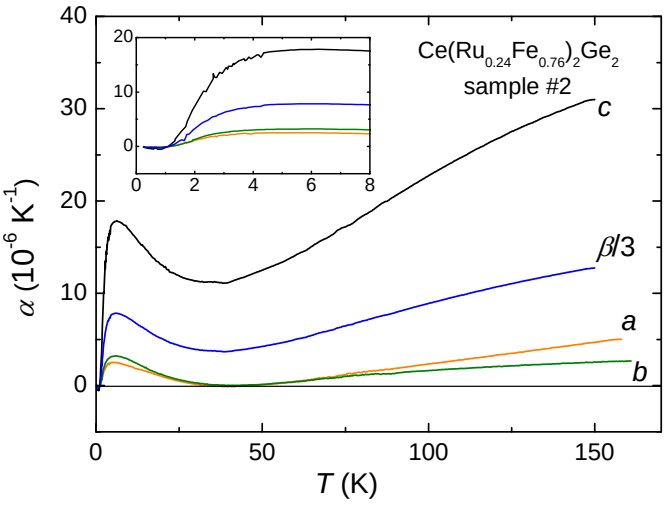

Figure 4.8: Coefficient of linear thermal expansion of $Ce(Ru,Fe)_2Ge_2$ with nominal concentration x_{cr}=0.76 (sample #2). The blue curve gives the volumetric thermal expansion coefficient divided by three, $\beta/3$. The horizontal line represents $\alpha = 0$. Inset: blow-up of the low temperature part of the data. The drop in α_i for $T < 2$ K is due to the magnetic order.

The thermal expansion shows a clear anisotropy $\alpha_c > \alpha_{a,b}$. The anisotropy can be attributed to the large splitting of the CEF ground state. A similar anisotropy was reported for $CeRu_2Si_2$ [115] (Δ_{CEF}= 220 K [116]). Below 2 K α drops for all three axes, which we attribute to the magnetic transition. For symmetry reasons α_a should be equal to α_b. Nevertheless small differences are found below 25 K and above 70 K. The origin of the differences is unclear, but is probably related to strain effects when the c axis parameter changes rapidly.

The volumetric thermal expansion coefficient $\beta = \alpha_a + \alpha_b + \alpha_c$ is plotted in fig. 4.9. At low temperatures ($T < 2$ K) α_b was not measured and we used the relation $\beta = 2\alpha_a + \alpha_c$. For 50 K $< T <$ 150 K the data resemble a Debye

function like in the case of the specific heat. For $T < 50$ K the contribution of the 4f electrons is dominant, i.e. a large heavy-fermion contribution with a maximum near $T = 6$ K. For $T < 2$ K, β drops faster because of the AFM transition and it becomes negative below T=1.1 K. For $T \to 0$ β approaches zero as expected.

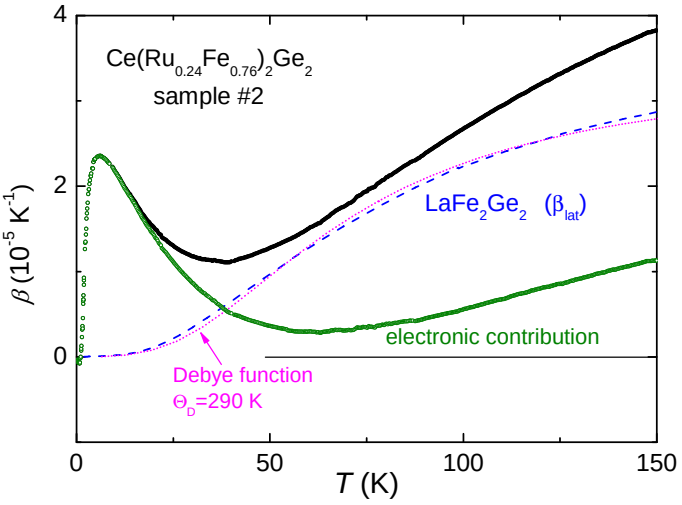

Figure 4.9: Calculated electronic contribution to the thermal expansion of $Ce(Ru,Fe)_2Ge_2$. The black dots give the measured data for $Ce(Ru_{0.24}Fe_{0.76})_2Ge_2$ sample #2. The dashed line is the $LaFe_2Ge_2$ data calculated from the specific heat data by means of the Grüneisen relation ($\Gamma_{\rm lat}$=2, see text), as an estimation for $\beta_{\rm lat}$. The dotted line is a Debye function adapted to the $LaFe_2Ge_2$ data, with $\Theta_{\rm D}$=290 K. The empty symbols give the electronic thermal expansion coefficient, obtained after subtracting the $LaFe_2Ge_2$ data from the raw data. The solid horizontal line represents β=0.

An estimate for the phonon contribution to the thermal expansion of $Ce(Ru,Fe)_2Ge_2$ is derived from the specific heat data of $LaFe_2Ge_2$ by taking into account a phononic Grüneisen parameter $\Gamma_{\rm lat}$=2 [49]:

$$\beta_{\rm lat} = \frac{\kappa_{\rm T}}{V_{\rm m}} \Gamma_{\rm lat} c_{\rm lat}. \tag{4.2}$$

Here the molar volume $V_{\rm m}$=5.53$\times$ 10^{-5} m^3/mol is calculated taking into account a linear variation of the lattice constants when going from $CeRu_2Ge_2$ to $CeFe_2Ge_2$. The assumption is corroborated by the low temperature data

in ref. [95]. The lattice constants of the pure compounds are taken from ref. [99] for $CeRu_2Ge_2$ and from ref. [117] for $CeFe_2Ge_2$. The compressibility κ_T=0.74 $\times$ 10^{-11} Pa^{-1} is calculated from the bulk modulus B_0=135 GPa [104]. In fig. 4.9 we show β_{lat} derived as discussed and compare it with the Debye function with Θ_D=290 K. We also show the 4f-electron contribution to the volume thermal expansion coefficient β_{el}. Notice that β of the $Ce(Ru_{0.24}Fe_{0.76})_2Ge_2$ sample #2 always exceeds the estimated phonon contribution. For $T < 50$ K the large heavy fermion contribution is dominant. For $T > 80$ K another electronic contribution is detected. A similar but smaller electronic contribution ($\sim$6%) is present in the specific heat data of sample #1, extrapolated up to T=150 K. This is most likely the low temperature shoulder of the CEF anomaly, present for $T > 80$ K in the pure compound [71] (fig. 4.2). We conclude we may neglect the contribution of phonons below 15 K, our temperature region of interest.

4.2.3 Grüneisen ratio

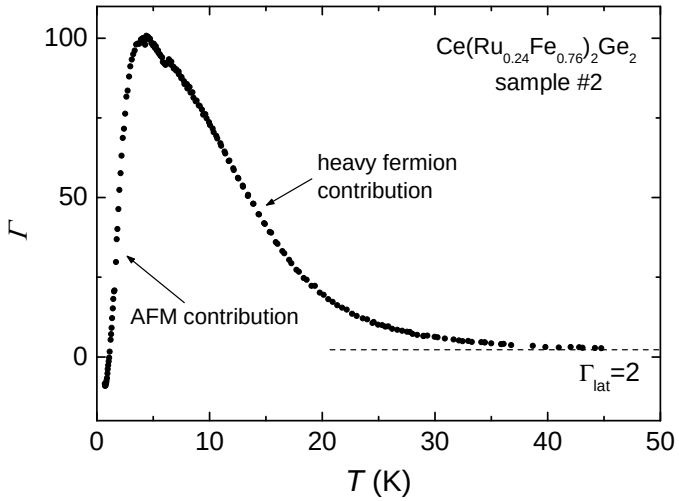

Figure 4.10: Grüneisen ratio of $Ce(Ru_{0.24}Fe_{0.76})_2Ge_2$ sample #2. The dashed line indicates the theoretical phononic Grüneisen ratio Γ_{lat}=2.

From the thermal expansion and specific heat data we calculate the Grüneisen ratio Γ (fig. 4.10), using the same values listed above for the mo-

lar volume and the compressibility. The Grüneisen ratio at high temperature ($T \sim 50$ K) has a constant value of $\Gamma \sim 2$ as expected for phonons [49]. This supports the procedure used above to derive the electron contribution in the thermal expansion data. Upon lowering the temperature, Γ increases due to the HF contribution until it reaches a high value of Γ_{max}=100 at 4 K. For $T < 4$ K it drops to below 0 because of the AFM transition. At low temperature the Grüneisen ratio seems to level off at $\Gamma \sim$-10 (fig. 4.11), where the negative value is expected when the AFM is the dominant energy scale.

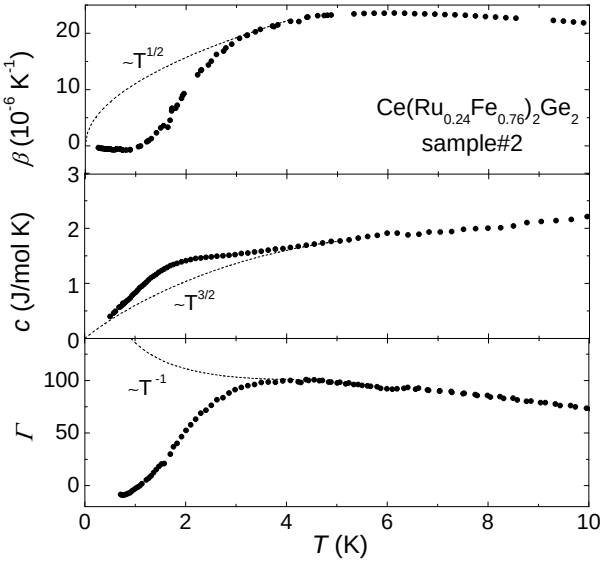

Figure 4.11: Thermal expansion, specific heat and Grüneisen ratio as a function of temperature for $Ce(Ru_{0.24}Fe_{0.76})_2Ge_2$ sample #2. The filled dots are the measured data, the dashed lines are the expected critical behaviour for an AFM QCP in a SDW scenario (see text).

The volume thermal expansion, the specific heat and the Grüneisen parameter are plotted in fig 4.11. In the same figure a qualitative representation of the predicted critical behaviour for an AFM QCP in a SDW scenario [23] is

shown:

$$\begin{aligned} \alpha_{cr} &\propto T^{1/2} \\ c_{cr} &\propto T^{3/2} \\ \Gamma_{cr} &\propto T^{-1}. \end{aligned} \tag{4.3}$$

The theoretical curves are 'normalized' to the measured data in the temperature range 4 K $< T <$ 6 K. Clearly the data do not follow eq. 4.3, as expected from the previous discussion: AFM order prevents the predicted critical low temperature behaviour. At the same time this hampers us to discern between the SDW or local quantum critical fluctuations scenarios, as discussed in chapter 2.

4.3 Tuning with magnetic field

The presence of an antiferromagnetic transition prevents the study of the Grüneisen ratio at the quantum critical point, but its high value at low temperature suggests that the compound is nevertheless close to a QCP. This provided the motivation to investigate whether we can suppress the AFM transition by applying a magnetic field B [4], thereby introducing a second control parameter.

Therefore we carried out magnetoresistance (MR) and magnetostriction (MS) experiments with the magnetic field applied along the direction of the magnetic moment, i.e. the c axis.

The magnetoresistance data are taken on a resistivity bar (dimensions $\sim$1×1×4 mm^3) of $Ce(Ru_{0.24}Fe_{0.76})_2Ge_2$ prepared along the c axis (same batch as sample #2). The residual resistance ratio RRR=2.1. The magnetic field was always applied along the c axis in the longitudinal configuration $B \parallel I \parallel c$. The results are shown in fig. 4.12 for T = 0.3 K and T = 6 K. At T=0.3 K, the data show a pronounced change for $B <$ 1 T. Taking the inflection point in the $R(B)$ curve we determine a characteristic field B_c=0.7±0.1 T. The MR data at T=6 K do not show such a change. We therefore identify B_c with the critical field for the suppression of AFM order: the sample is driven from an AFM ordered state at B=0 (corroborated by the data in 4.2) to a polarized phase for $B > B_c$. The values in the ordered AFM state are higher than the ones in the polarized state, as it will be reported also for the resistivity in zero field $\rho(T)$, showing that electron scattering is less effective in the latter. A similar effect is observed for the MR in the pure compound $CeRu_2Ge_2$ for field $B <$ 8 T and for temperature close to the transition temperature [118]. The

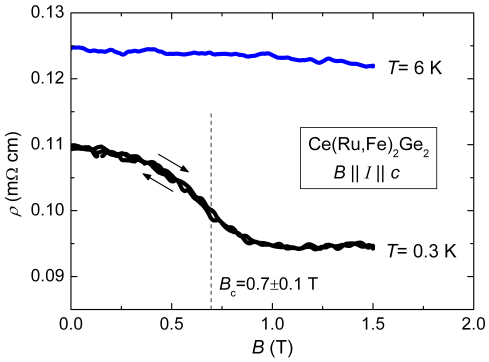

Figure 4.12: Magnetoresistance of $Ce(Ru,Fe)_2Ge_2$ with $x \sim 0.76$, for $B \| I \| c$ at T=0.3 K (black curve) and T=6 K (gray curve). The dashed line at B_c=0.63±0.01 T indicates the inflection point.

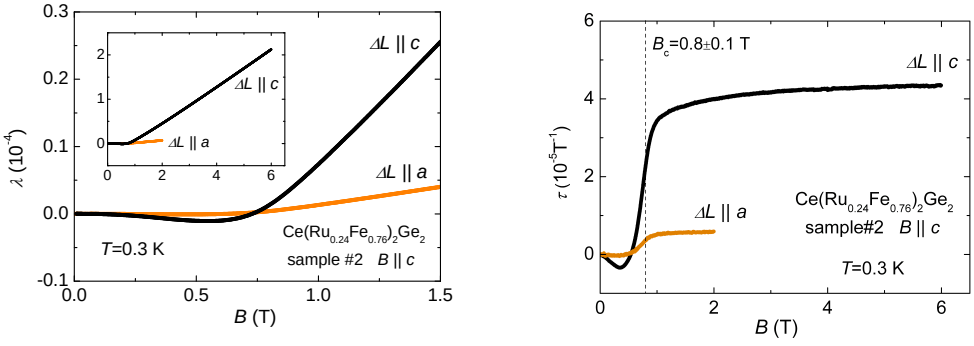

Figure 4.13: [left] Low temperature linear magnetostriction λ of $Ce(Ru_{0.24}Fe_{0.76})_2Ge_2$ sample #2 for $B \| c$ and $\Delta L \| a$ or $\Delta L \| c$. Inset: Linear magnetostriction λ of $Ce(Ru_{0.24}Fe_{0.76})_2Ge_2$ sample #2. [right] Coefficient of linear magnetostriction $\tau = d\lambda/dB$ of $Ce(Ru_{0.24}Fe_{0.76})_2Ge_2$ sample #2 as a function of the magnetic field for $B \| c$, with $\Delta L \| a$ (gray) and $\Delta L \| c$ (black). The characteristic field calculated as the inflection point B_c=0.75±0.01 T is marked by the vertical dashed line.

low temperature data are measured in up and down sweeps and no hysteresis is detected.

The magnetostriction data are taken on the same sample as used in the thermal expansion and specific heat experiments (section 4.2). The magnetic field was always applied along the c axis ($B \parallel c$) either in transverse configuration $B \perp \Delta L \parallel a$ or in longitudinal configuration $B \parallel \Delta L \parallel c$. In fig. 4.13 the magnetostriction coefficient λ (left panel) and its derivative $\tau = d\lambda/dB$ (right panel) from $Ce(Ru_{0.24}Fe_{0.76})_2Ge_2$ sample #2 at T=0.3 K are reported. The MS data show that the effect along the c axis is more pronounced than along the a axis. The characteristic field, determined as the inflection point, is B_c=0.8±0.1 T in agreement with the previous value. Since magnetostriction is a bulk property, in the following we take the critical field as $B_c \sim 0.8$ T. This value can slightly change with different samples and different determination methods, but the presence of the transition is the most relevant observation.

4.4 Transport properties of $Ce(Ru_{0.24}Fe_{0.76})_2Ge_2$ in field

The resistivity is subsequently measured at a constant applied magnetic field. The temperature variation of the resistivity was measured in the Heliox at several constant fields ($B \leq 1.5$ T), by sweeping the temperature from 6 K to base temperature. The sample used in this section was also used in the previous magnetoresistance experiments.

The results of sample #2 for $I \parallel c$ are shown in fig. 4.14. For $T \geq 3$ K the $\rho(T)$ curves are quite similar. In zero field an up-turn is present below 2 K: this is a clear sign of the AFM transition and it is smoothly suppressed by applying a magnetic field. In the AFM phase the resistivity is higher than in the PM phase, which is possibly due to the spin density wave coupled to a broad magnetic transition.

In fig. 4.15 the parameters of a fit of the resistivity data to $\rho = \rho_0 + AT^n$ are presented. The resistivity data are fitted in the temperature range outside the FM state. For $B \geq 0.75$ T temperatures in the range 0.24 K $< T <$ 3.5 K have been considered, while for $B < 0.75$ T the lowest temperature used is the temperature at which the up-turn in resistivity takes place. The fit parameters change as a function of the field, with a maximum or a minimum in the vicinity B_c. For the residual resistivity ρ_0 this change is only a few percent but for the temperature coefficient A and the temperature exponent n the relative change is much more pronounced. The temperature exponent n has a dip for $B \sim B_c$: from a value close to 2 (typical for a FL) at small magnetic field, it reaches $n \sim 1.3$ for B=0.75 T. The value of n is already smaller than the value n=3/2 for an AFM QCP within the SDW theory. For $B \geq 1$ T, the

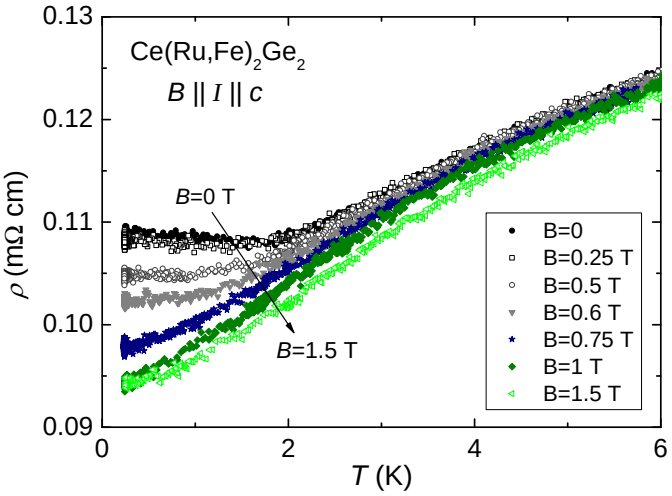

Figure 4.14: Resistivity versus temperature of $Ce(Ru,Fe)_2Ge_2$ with $x \sim 0.76$, for $I \| c$ and $B \| c$ in magnetic field up to 1.5 T.

temperature exponent slowly starts to increase in order to slowly recover the FL exponent value n=2. Such a slow recovery of the FL behaviour is observed in the thermal properties (sec. 4.5), in pressure experiments [94, 107] and in Si-doping experiments [95] and it is probably due to a broad transition.

4.5 Thermal properties of $Ce(Ru_{0.24}Fe_{0.76})_2Ge_2$ in field

In this section we report thermal expansion and specific heat measurements on $Ce(Ru_{0.24}Fe_{0.76})_2Ge_2$ sample #2 in a magnetic field $B \parallel c$. Subsequently we report the Grüneisen ratio. The sample used in this section is the same as used for measuring the thermal properties in zero field (sec. 4.2).

4.5.1 Thermal expansion

The thermal expansion was measured on $Ce(Ru_{0.24}Fe_{0.76})_2Ge_2$ sample #2 in a magnetic field. The thermal expansion for $\Delta L \parallel a$ was measured in magnetic fields $B \leq 1$ T with $B \parallel c$. For $\Delta L \parallel a$ data were taken for a field B=0.75 T with $B \parallel a$ as well, but no change from the ZF data is observed . The thermal expansion for $\Delta L \parallel c$ was measured in magnetic fields $B \leq 6$ T and $B \parallel c$. The results are reported in figs. 4.16 and 4.17.

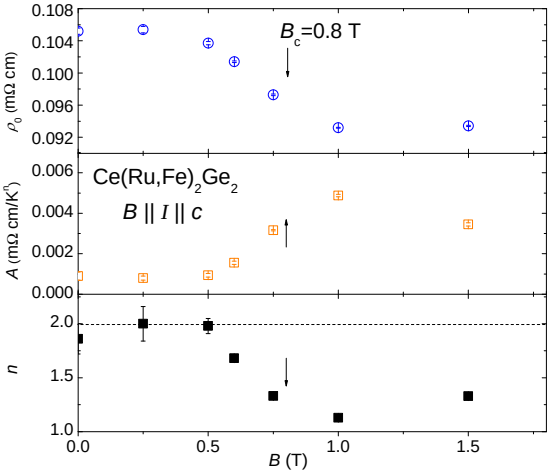

Figure 4.15: Resistivity fit parameters for $Ce(Ru,Fe)_2Ge_2$ with $x \sim 0.76$, $I \parallel B \parallel c$. The data have been fitted to $\rho = \rho_0 + AT^n$. The arrows indicate $B_c \sim 0.8$ T.

The results in zero field have already been discussed in sec. 4.2. Upon applying a magnetic field $B \parallel c$, the a and the c axes have a similar response: at high temperature there is no change for small magnetic fields, while at low temperatures the AFM transition is suppressed already for $B > 0.5$ T. By fitting the data as $\alpha = aT^n$, a linear behaviour is detected for $\alpha \to 0$ at $B \sim 0.8$ T (see dashed lines in figs. 4.16 and 4.17). For $B \geq 1$ T the coefficient a becomes smaller and α approaches 0 with $n \geq 1$. For $B \geq 1.5$ T, α_c starts to deviate from the zero field behaviour both at low and high temperature. Upon further increase of the magnetic field, the linear thermal expansion coefficient α_c differs much from the data at lower field and is even negative at $T < 4$ K for B=6 T.

The behaviour of the linear thermal expansion coefficient for $B > 0$ is better pictured in fig. 4.18 by the parameters of a power law data fit used to describe the approach to criticality. The thermal expansion data are fitted to α=aT^n, forcing the function to α=0 when T=0, as predicted by thermodynamics. The fits are made in the temperature range $T < T_{\rm infl}$, where $T_{\rm infl}$ is the temperature where α has an inflection point. In all the cases $T_{\rm infl}$=2-3 K apart for α_c at B=0.6 T where the maximum measured temperature was T=1.6 K. The fit parameters for both crystallographic axes have a similar trend. The temperature power law coefficient n sharply decreases upon increasing the magnetic field, until $n \sim$1 at $B \sim B_c$ for the a and c axes. Here we observe a small

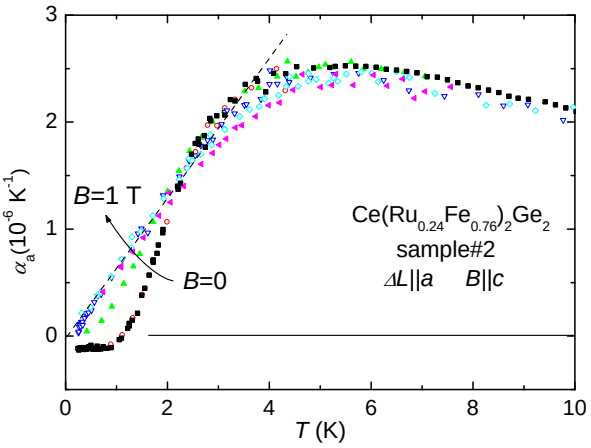

Figure 4.16: Coefficient of linear thermal expansion along the a axis, α_a, of $Ce(Ru_{0.24}Fe_{0.76})_2Ge_2$ sample #2 in zero field (■) and in fields applied along the c axis. Fields are 0.5 (▲), 0.75 (▽) , 0.85 (◇), and 1 (◀) T. For B=0.75 T, data on $\Delta L \| a$ and $B \| a$ (○) are reported for comparison. The dashed line is a guide to the eye for the linear behaviour at low temperature for $B \sim B_c$.

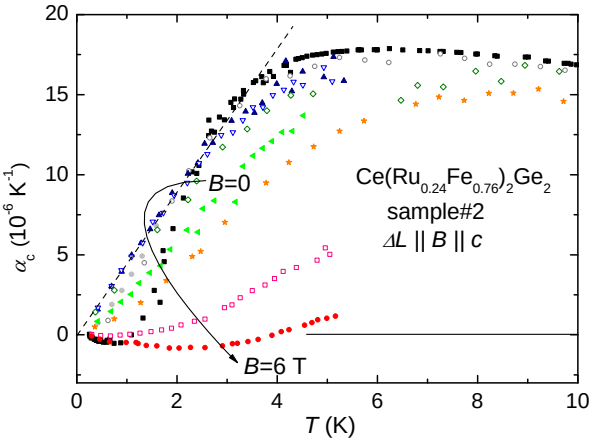

Figure 4.17: Coefficient of linear thermal expansion along the c axis, α_c, of $Ce(Ru_{0.24}Fe_{0.76})_2Ge_2$ sample #2 in zero field (■) and in applied fields. Fields are 0.5 (○), 0.6 (●), 0.75 (▲) , 0.85 (▽), 1 (◇), 1.5 (◀), 2 (★), 4 (□), and 6 (●) T. The dashed line a guide to the eye for the linear behaviour of the low temperature data for $B \sim B_c$.

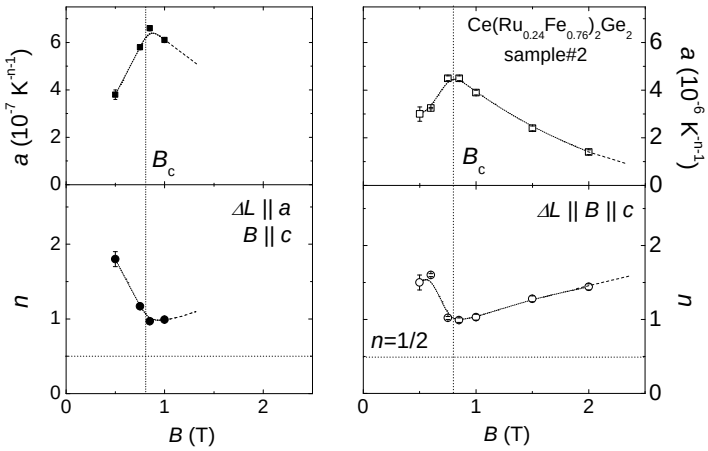

Figure 4.18: Fit parameters a and n for the linear thermal expansion coefficient α_a [left] and α_c [right] as a function of the applied magnetic field B of $Ce(Ru_{0.24}Fe_{0.76})_2Ge_2$ sample #2. The dashed line is a guide to the eye, while the dotted vertical line indicates the characteristic field $B_c \sim 0.8$ T. The horizontal dotted line gives the predicted temperature exponent of a AFM SDW QCP, n=1/2.

plateau ($\Delta B \sim 0.3$ T). For the a axis no further data are available. For the c axis instead we are able to fit the data until B=2 T and we record a slow recovery of the zero field coefficient. For $B > 2$ T the data no longer can be fitted with a power law function. The vertical dashed line that marks the characteristic field B_c in fig. 4.18 is located in the small plateau where n has the smallest value of ∼1. The lowest value of the temperature exponent is higher than the predicted exponent of a AFM SDW QCP n=1/2 (horizontal dashed line). Moreover the fast drop and slow recovery of n resemble the trend of the temperature exponent of the resistivity in fig. 4.15. As discussed in sec. 4.4, the slow recovery of the FL behaviour for $B > B_c$ was already observed. The temperature coefficient a has a behaviour which is similar, but mirrored with respect to n, with a maximum instead of a minimum at $B \sim B_c$.

The volume thermal expansion coefficient β is calculated for the data in field as $\beta = 2\alpha_a + \alpha_c$ as described in sec. 4.2. All the data measured in the same magnetic fields for the a and the c axis (B=0, 0.5, 0.8, 1 T) are reported and the results are shown in fig. 4.19. At high temperature (∼6 K) $\beta(T)$ decreases proportionally to the field and a 20% difference between the zero field and the B=1 T data is reported. The AFM transition is depressed already considerably in a small field B=0.5 T. The highest value of β at low

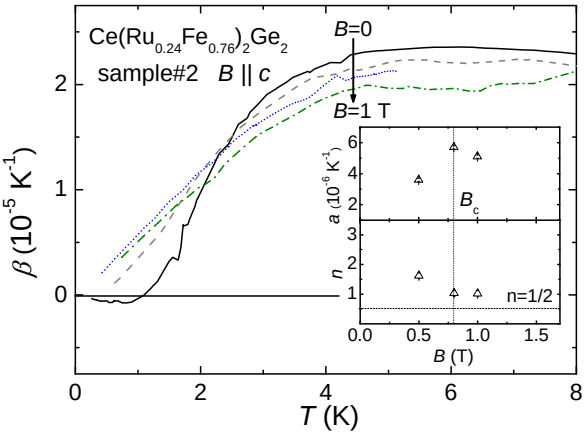

Figure 4.19: Coefficient of volume thermal expansion β of $Ce(Ru_{0.24}Fe_{0.76})_2Ge_2$ sample #2 in zero field (black) and in applied fields of 0.5 T (dashed line), 0.8 T (dotted line) and 1 T (dashed-dotted line). The field is applied along the c axis. Inset: fit parameters a and n for the volume thermal expansion coefficient β as a function of the applied magnetic field B. The dotted vertical line indicates the characteristic field B_c while the horizontal dashed line is the predicted temperature exponent of a AFM SDW QCP, n=1/2.

temperature is observed for B=0.8 T. A similar analysis as presented for α is reported in the inset of fig. 4.19. The data are fitted to $\beta = aT^n$ and the trend resembles the one reported in fig. 4.18, with a plateau for $B \sim B_c$.

4.5.2 Specific heat

The specific heat of $Ce(Ru_{0.24}Fe_{0.76})_2Ge_2$ sample #2 was measured in fields applied along the c axis ($B \| c$) up to 4 T on the same sample as used for the thermal expansion measurements. The results are reported in fig. 4.20. The data show a similar trend as observed in the thermal expansion data but a weaker field dependence. At high temperature the field dependence is weak. The AFM order, indicated by the maximum in c/T versus T near 1.2 K, is suppressed in a small magnetic field ($B \sim 0.8$ T). For $B \geq 1.5$ T the specific heat data proceeds to decrease as the sample is tuned away from the critical behaviour. The c/T value at 0.5 K as a function of the magnetic field is reported in the inset of fig. 4.20. For B=0, T=0.8 K is the lowest temperature and c/T at 0.5 K is calculated with a linear fit of the data in the temperature

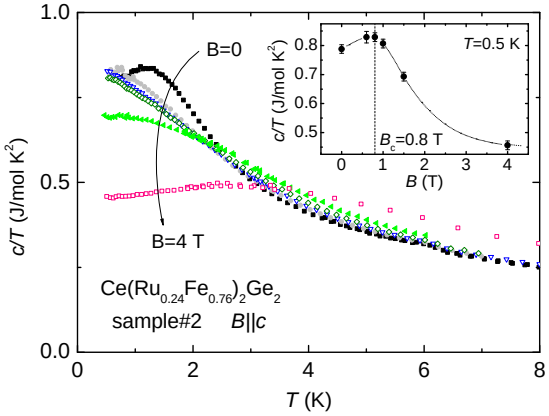

Figure 4.20: Specific heat divided by temperature as a function of temperature for $Ce(Ru_{0.24}Fe_{0.76})_2Ge_2$ sample #2, in zero field (■) and in field applied along the c axis $B\|c$. Fields are B 0.6 (●), 0.8 (▽), 1 (◇), 1.5 (◀), and 4 T (□). Inset: c/T at T=0.5 K as a function of the applied magnetic field. The dotted line is a guide to the eye. The dashed vertical line marks the characteristic field B_c. Data taken by Dr. J. C. P. Klaasse and M. Nale.

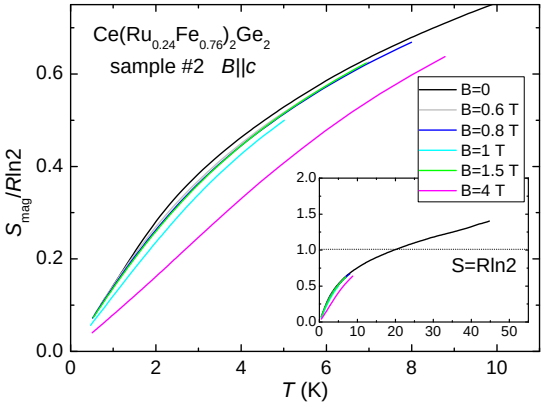

Figure 4.21: Magnetic entropy of $Ce(Ru_{0.24}Fe_{0.76})_2Ge_2$ sample #2 in units of $R\ln 2$ in the low temperature region for zero field (black line) and for fields applied along the c axis. The applied fields are B=0.6 (gray), 0.8 (blue), 1 (cyan), 1.5 (green), and 4 T (magenta). Inset: The magnetic entropy of $Ce(Ru_{0.24}Fe_{0.76})_2Ge_2$ sample #2, up to 45 K. The dotted line represents the entropy of the ground state doublet.

range T=0.8-1 K, giving a value 0.83 J/mol K^2.The value of c/T here obtained is compared with the γ values reported in literature. To avoid confusion we refer to the calculated c/T value at 0.5 K as the γ value.

The γ value at the magnetically tuned QCP is just $\sim$ 3% higher than the γ value at the doping tuned QCP reported in ref. [112, 113] for $Ce(Ru_{0.24}Fe_{0.76})_2Ge_2$ sample #1. The γ value for the pressure induced QCP is reported to be around 10 times lower than both the other values. In ref. [107] the Sommerfeld value of $CeRu_2Ge_2$ at p=67.5 kbar is indeed given as γ=0.080 J/mol K^2. This value is obtained from the Kadowaki-Woods ratio [119] A/γ^2=3.3 $\mu\Omega$ cm mol^2 K^2/J^2 of $CeRu_2Si_2$. The γ value for $CeRu_2Ge_2$ under pressure is therefore particulary small and probably underestimated. This we attribute to the non-validity of the Kadowaki-Woods ratio next to a QCP [17, 120]. From calorimetry experiments under pressure (arbitrary units) [121] we can roughly estimate $\gamma \sim$0.13 J/mol K^2, which is still much smaller that the other values at the QCP.

The magnetic entropy $S_{\rm mag}$ is calculated by integrating the electronic specific heat $c_{\rm el}$ divided by temperature versus the temperature. The lattice contribution in zero field is subtracted to calculate the electronic specific heat of the data in field. The data are then plotted together with $S = 0$ at T=0 for all data sets. The result is shown in fig. 4.21. For B=0, the magnetic entropy for the ground state doublet Rln2 is recovered already at T=20 K, as for the pure compound. This tells us that the HF contribution is still present in the system upon doping. When approaching the QCP, the specific heat divided by the temperature is predicted to be enhanced for $T \rightarrow 0$ with a corresponding shift of the entropy to low temperatures. This is not seen in our entropy data because for $B < 1$ T the field effect is very small. For higher applied magnetic fields, $S_{\rm mag}$ decreases with field. This is clearly visible at B=4 T. This is the signature that the entropy is shifted to higher temperatures and the system is tuned away from the QCP.

4.5.3 Grüneisen ratio

The Grüneisen ratio was determined for the field applied along the c axis at 0, 0.6, 0.8, 1 T. The results are reported in fig. 4.22. At high temperature ($\sim$5 K) the Γ value decreases with increasing field with a change of $\sim$20% in the maximum field of 1 T. At low temperature a large field effect is observed. The Grüneisen ratio increases from -10 in zero field data (AFM) to a maximum value of 50 in 0.8 T. As discussed in sec. 4.2, the large Γ value shows the presence of the heavy fermion contribution, which apparently becomes broader in field though maintaining roughly the same characteristic temperature. A divergence of the Grüneisen ratio is not observed even at $B = B_{\rm c}$ although

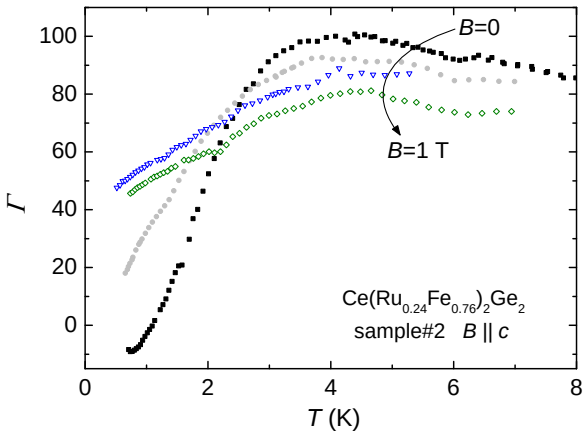

Figure 4.22: Grüneisen ratio of $Ce(Ru_{0.24}Fe_{0.76})_2Ge_2$ sample #2 in zero field (■) and in field applied along the c axis. Field values are 0.6 (●), 0.8 (▽), and 1 T (◇).

at this characteristic magnetic field Γ shows the maximum value Γ=50 at the lowest temperature measured ($T = 0.5$ K).

4.5.4 Discussion

In fig. 4.23 we summarize the results obtained on the thermal properties in field. We consider only the electronic contribution to the thermal expansion, the specific heat and the Grüneisen ratio, calculated after subtracting the estimated phononic contribution in zero field (sec. 4.2). The volume thermal expansion shows a quite strong field dependence at low temperature: β/T for $T < 2$ K at B=0.8 T is more than 3 times bigger than the absolute value in zero field. Already for small field (B=0.6 T) the volume thermal expansion becomes no longer negative and the AFM transition is not present anymore in the data. For $B = B_c$, β_{el}/T is quite constant. For $B > B_c$, the thermal expansion coefficient β is smaller than at $B = B_c$. The electronic specific heat data show a less pronounced field dependence. For B=0.6 T a transition is still measured (the lowest temperature is lower than the thermal expansion one) and the magnetic order is suppressed for $B \leq B_c$. The Grüneisen ratio follows the thermal expansion. The Grüneisen ratio has the highest low temperature value $\Gamma_{el} = 50$ at the critical field and for $B > B_c$ it decreases. Although the low temperature value is elevated, and at $B = B_c$ it is the highest in the data sets, no divergence is observed.

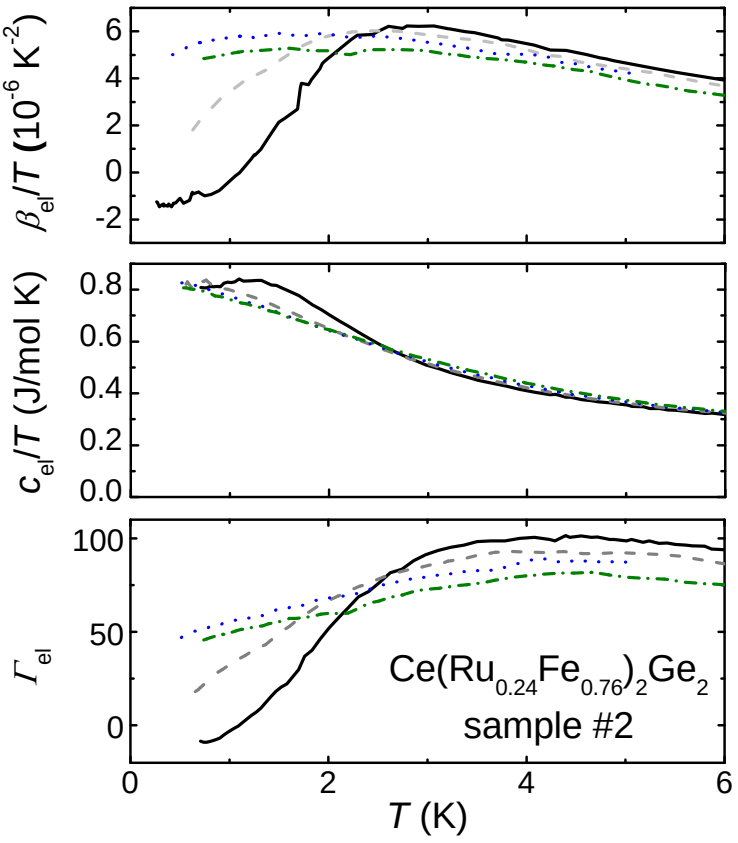

Figure 4.23: [top] Electronic volume thermal expansion divided by temperature, [middle] electronic specific heat divided by temperature, and [bottom] electronic Grüneisen ratio of $Ce(Ru_{0.24}Fe_{0.76})_2Ge_2$ sample #2, in zero field (black) and in applied fields of 0.5 T (dashed line), 0.8 T (dotted line) and 1 T (dashed-dotted line). For all the curves the field is applied along the c axis, $B \| c$.

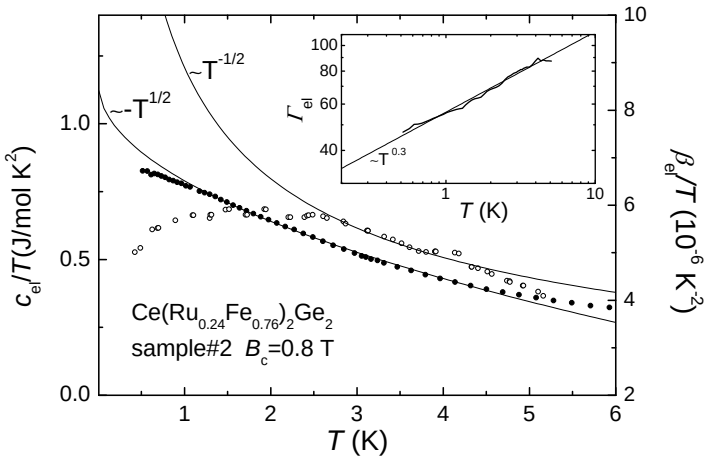

Figure 4.24: Electronic specific heat (filled symbols) and coefficient of electronic volume thermal expansion (empty dots), both divided by temperature, of $Ce(Ru_{0.24}Fe_{0.76})_2Ge_2$ sample #2 at B_c=0.8 T. The lines represent the fits made according to the SDW prediction for an AFM QCP as $c/T = \gamma - bT^{1/2}$ and $\beta/T = a + cT^{-1/2}$. Inset: Electronic Grüneisen ratio of $Ce(Ru_{0.24}Fe_{0.76})_2Ge_2$ sample #2 in a log-log plot. The line represents the fit to $\Gamma_{el} = AT^{-x}$ with $x = -0.3$.

A comparison of the data of the specific heat c_{el}/T and the thermal expansion β_{el}/T at B=0.8 T with the critical behaviour expected for an AFM QCP in SDW is made in fig. 4.24. The solid lines in the plot show the theoretical prediction for a *pressure* induced AFM SDW QCP in 3D. The comparison shows that a single component fit is not possible in the case of a field induced AFM QCP in $Ce(Ru,Fe)_2Ge_2$ with $x \sim 0.76$. Other additional terms could account for the contribution of the remaining local moment at low temperature, as discussed in the introduction, or for the influence of a magnetic field. The electronic Grüneisen ratio is shown in the inset in a log-log plot. A fit is made to identify the characteristic exponent x in $\Gamma \sim T^{-x}$. Here x is expected to be positive but we find $x = -0.3$, at odds with the prediction.

The discrepancy with the theory is not completely surprising. The system studied here does not comply with the theory proposed in ref. [23] (see chap. 2). The presence of non-critical contributions that cannot be discerned from the critical one or, even the presence of different competing critical contributions, could prevent the Grüneisen ratio from diverging. As discussed before in sec. 6.1, it is not clear which magnetic fluctuations drive the system

to criticality. Moreover this system lies above the upper critical dimension 4 for $d + z$, since d=3 and z=2. At the upper critical dimension, logarithmic corrections arise. Above the upper critical dimension, the scaling argument can be spoiled by the presence of so called 'dangerously irrelevant operators' [23]. This is taken into account in the calculation of the diverging Grüneisen ratio in the SDW scenario. If in $Ce(Ru_{0.24}Fe_{0.76})_2Ge_2$ a different mechanism for quantum criticality is at work, the Grüneisen ratio above the critical dimension could be logarithmically damped and will not diverge.

In addition we need to notice that in the discussion presented in sec. 4.5 we considered the thermal Grüneisen ratio $\Gamma_{\rm T}$, while in ref. [23] the magnetic Grüneisen ratio $\Gamma_{\rm mag} = -(dM/dT)_{\rm H}/c_{\rm cr}$ is predicted to diverge when the control parameter is the magnetic field. This has been shown for instance for the field induced AFM QCP in $YbRh_2Si_2$ [122]. Generally, when the electronic system is described by a single energy scale $\Gamma_{\rm mag}$ is approximately equal to $\Gamma_{\rm T}$ [123]. This is the case for instance in $CeRu_2Si_2$ [124] or next to an AFM QCP in $YbRh_2Si_2$ [125]. Nevertheless it is possible that in our case two energy scales are present [37] and that the thermal and magnetic Grüneisen ratios do not couple. This could be clarified by further measurements of the magnetocaloric effect $(dM/dT)_{\rm H}$.

4.6 Summary

The thermal expansion and specific heat of $Ce(Ru_{0.24}Fe_{0.76})_2Ge_2$ in zero applied magnetic field were measured and the Grüneisen ratio was subsequently derived. The asymptotic low temperature behaviour differed from that predicted for a SDW AFM QCP, and, as was clear from the susceptibility data, AFM order is present in the sample. From the Néel temperature $T_{\rm N}$ ∼1.2 K, we concluded that the sample has an Fe content x that is lower than the nominal critical concentration. From the phase diagram reported in ref. [94] we estimated $x \sim 0.75$ at.% of Fe. This offered the possibility of suppressing the AFM order by magnetic field tuning and to study a field induced AFM QCP in Ce(Ru,Fe)$_2$Ge$_2$.

Magnetostriction (MS) and magnetoresistance (MR) were used to determine the characteristic field at which the AFM transition is suppressed and the system turns into a spin-polarized phase. For both MS and MR the field is applied along the c axis (the direction of the magnetic moments). The MR data reveal an inflection point at $B_{\rm c}^{\rm MR} = 0.7 \pm 0.1$ T for $B \| I \| c$. From the MS data for $B \| \Delta L \| c$ or $B \| c$ and $\Delta L \| a$ we extract $B_{\rm c}^{\rm MS} = 0.8 \pm 0.1$ T. The MS response along the a axis is less pronounced than the one along the c axis. Since the MS is a bulk property, we take the critical field as $B_{\rm c} \sim 0.8$ T.

Next we investigated the $Ce(Ru_{0.24}Fe_{0.76})_2Ge_2$ sample by resistivity, thermal expansion and specific heat measurements in field ($B \| c$). The behaviour of the transport and thermal properties was analysed by means of the parameters of power law fits.

The resistivity data ($B < 1.5$ T) with $I \| c$ were fitted by $\rho(T) = \rho_0 + AT^n$. The fit parameters have their maximum or minimum at $B \sim B_c$. For $B > B_c$ we report a slow recovery of the FL behaviour, as observed in pressure and doping experiments around the QCP. The temperature exponent n at $B \sim B_c$ is $\sim$1.3, which is lower than the value of the exponent predicted for a SDW AFM QCP, n=3/2. This discrepancy is possibly due to crystallographic disorder.

Thermal expansion and specific heat in field ($B < 6$ T for the former and $B < 4$ T for the latter) have been measured and the Grüneisen ratio was detemined in fields $B = 0, 0.6, 0.8$, and 1 T. The main result is presented in fig. 4.23. In both thermal expansion and specific heat we observed a suppression of T_N in a small magnetic field, although the specific heat has a weaker field dependence. The volume thermal expansion coefficient was fitted by a power law function $\beta = aT^n$ with a minimum $n = 1$ for $B \sim B_c$. This value is higher than the exponent predicted for an AFM SDW QCP $n = 1/2$. The specific heat divided by the temperature c/T at $T = 0.5$ K was reported as representative for γ. At $B \sim B_c$ we reported its highest value $\gamma = 0.83$ J/mol K^2. The magnetic entropy S_{mag} calculated from the specific heat data had, as well, a weak field dependence. Nevertheless the data at $B = 4$ T showed that the entropy is shifted to higher temperatures and the system is tuned away from the QCP. The Grüneisen ratio has a strong field dependence. Although it reaches its highest low temperature ($T = 0.5$ K) value Γ_{mag}=50 at $B \sim B_c$, no divergence was observed, in disagreement with theory.

The behaviour at the critical field $B_c = 0.8$ T was analysed. The β_{el}/T and c_{el}/T data were compared with the prediction for an AFM SDW QCP, $\beta/T = a + cT^{-1/2}$ and $c/T = \gamma - bT^{1/2}$. Clear differences are observed. The Grüneisen ratio at B_c presented a temperature exponent x=-0.3, while a positive exponent is expected at the QCP. The discrepancy with the theory is not completely surprising. The system is reported to have a peculiar behaviour at the QCP tuned by doping. At the QCP both local and long-range fluctuations are present, although only the latter are believed to be critical. In the theory proposed in ref. [23] the presence of non-critical contributions that cannot be discerned from the critical one, or even the presence of different competing critical contributions, could prevent the Grüneisen ratio from diverging. Moreover this system is above the upper critical dimension $d + z = 4$. As a last fact, we mention that in the presence of a magnetic field as control

parameter, the magnetic Grüneisen ratio Γ_{mag} is predicted to diverge. If two energy scales are present, the thermal and magnetic Grüneisen ratios could not couple and only Γ_{mag} is predicted to diverge.

5 Itinerant ferromagnetic quantum critical point in U(Rh,Ru)Ge

il laboratorio rivisitato è sorgente di gioia
ed emana un fascino intenso

P. Levi

A few years after the discovery of URhGe, the first ambient pressure superconducting ferromagnet (SCFM) [26], it was demonstrated that URhGe could be tuned to a ferromagnetic quantum critical point (FM QCP) by doping with 38 at.% Ru [38, 126]. Several examples of antiferromagnetic (AFM) QCPs have already been discussed extensively in the literature (see refs. [4, 10, 11] for reviews). On the other hand the FM case has not been deeply studied, with Ce(Pd,Rh) [127, 128, 129] and $Zr_{1-x}Nb_xZn_2$ [130] as the only test-cases of a FM QCP. Here we investigate the properties of the FM QCP in U(Rh,Ru)Ge by means of the Grüneisen ratio. In this chapter we report the thermal expansion and the Grüneisen ratio of selected polycrystalline $URh_{1-x}Ru_xGe$ samples and of single crystalline samples with nominal concentrations x=0.38 and x=0.39.

5.1 Introduction

In 2001 the second SCFM URhGe was discovered [26]. The first SCFM, UGe_2, becomes superconducting under high pressures ($\sim$1 GPa) near the critical pressure for the suppression of ferromagnetism [24]. However, in URhGe FM and SC coexist at ambient pressure.

URhGe crystallizes in an orthorhombic structure, like UGe_2, with zig-zag chains of nearest-neighbour uranium atoms [131]. URhGe orders ferromagnetically below T_C=9.5 K with an ordered moment of μ_S=0.45 μ_B ($T \rightarrow 0$)

per formula unit, directed along the c axis. The analysis of the magnetization (Arrott plots) shows URhGe is an itinerant ferromagnet [132], while neutron scattering shows that the magnetization is almost entirely attributed to the uranium 5f electrons [26].

Superconductivity is found for $T_{sc} < 0.25$ K as demonstrated by resistivity and susceptibility data [26]. Evidence for bulk superconductivity is obtained by specific heat data. A strong sensitivity of the superconducting transition temperature to the quality of the samples provides evidence for unconventional superconductivity: no sign of SC down to 80 mK is present in samples with $\rho_0 \sim 30$ $\mu\Omega cm$ [26]. An unexpected and striking feature of URhGe is reentrant superconductivity, which can be induced by applying a large magnetic field ($B \sim 12$ T) along the b axis [133].

These observations raise the question whether URhGe can be brought to a FM QCP by applying mechanical or chemical pressure. In order to investigate the possible link between superconductivity and enhanced magnetic fluctuations, mechanical pressure is a clean way to drive a system to a QCP. Unfortunately this is not possible in URhGe. The Curie temperature increases by applying hydrostatic pressure at a rate of 0.065 K/kbar [27]. The increase of T_C is in agreement with the estimate made by the Ehrenfest relation, $dT_C/dp \sim 0.12$ K/kbar, which predicts a critical pressure p_{cr}=-80 kbar for the suppression of FM [134]. Consequently the applied pressure should be negative to tune the system to a FM QCP, which may be achieved by chemical substitution.

The first doping study of URhGe was reported in ref. [135]. Since among the isostructural UTX compounds, with T = transition metal and X = Ge or Si, only URuGe and UCoGe were reported to have a paramagnetic (PM) ground state [136, 137], Ru and Co are considered to be the best candidate dopants. Small amounts of Co increase the Curie temperature, however the FM order in URhGe can be depressed by replacing Rh by Ru and it completely vanishes at 38 at.% Ru [135]. URuGe has a smaller unit cell volume than URhGe, meaning that Ru-doping plays the role of providing negative pressure. Nevertheless for small Ru-content (< 10 at.% Ru) T_C increases. This is attributed to the fact that Ru and Rh are not isoelectronic: doping with Ru empties the electron d-band which leads to an increase of the Curie temperature.

Further studies on the $URh_{1-x}Ru_xGe$ system by means of resistivity, magnetization and specific heat measurements on polycrystalline samples are reported in ref. [38]. The main results are summarized in fig. 5.1. In the top frame the Curie temperature as a function of the Ru concentration is shown. The phase diagram shows T_C is suppressed for x_{Ru}=0.38. The middle frame reports the magnetization for $B = 0.01$ T and 1 T as a function of the Ru-

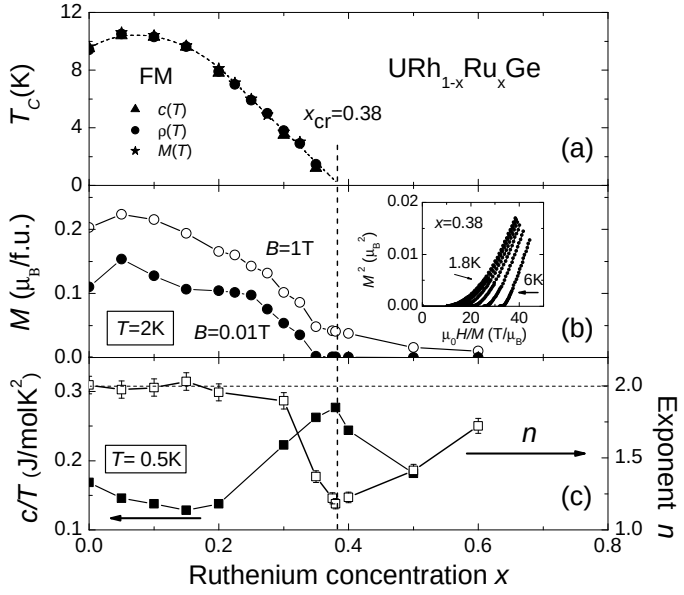

Figure 5.1: (a) Curie temperature determined from specific heat, resistivity and magnetization. The critical Ru content $x_{\rm cr}$=0.38 is indicated by the vertical dashed line. (b) Magnetization at T=2 K in B=0.01 T (filled dots) and in B=1 T (empty symbols). In the inset, the Arrott plot for $x_{\rm cr}$=0.38 at 1.8 K $\leq T \leq$ 6 K is shown. (c) Specific heat divided by temperature c/T at 0.5 K (filled squares) and the resistivity exponent n (empty squares). The horizontal dashed line indicates n=2. Figure taken from ref. [38].

concentration measured at 2 K. Notice, for B=0.01 T the magnetization is reduced due to demagnetization effects. Clearly the spontaneous magnetization vanishes for $x \rightarrow 0.38$ in a continuous way. This indicates that the FM to PM transition is a second order phase transition. The bottom frame shows the specific heat divided by the temperature c/T at 0.5 K (left vertical scale) and the resistivity exponent n of the non-Fermi liquid term in the resistivity, $\rho \sim T^n$ (right vertical scale). The former has a maximum at the critical concentration, while the latter attains a minimum value n=1.2 at $x_{\rm cr}$ followed by a slow recovery of the Fermi liquid (FL) value n=2 for $x > x_{\rm cr}$. These observations support the hypothesis of a critical behaviour at $x_{\rm cr}$, although the resistivity exponent is smaller than the value n=5/3 predicted in the case of a clean FM [7]. This is not unexpected since disorder reduces n, like for

instance reported in ref. [138]. Disorder might also explain why T_C deviates from the expected T_C suppression near a QCP for an itinerant clean FM. For d=3 and for a dynamical exponent z=3, $T_C \sim (x_{cr} - x)^{3/4}$ is expected, while for U(Rh,Ru)Ge $T_C \sim (x_{cr} - x)$ is found over the wide range $0.20 < x < 0.35$ [38].

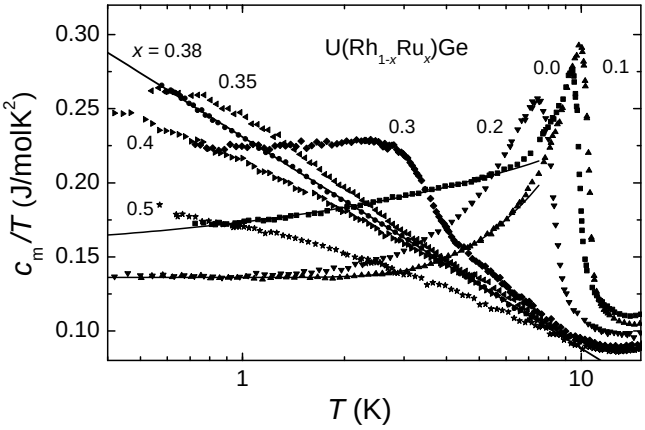

Figure 5.2: f-electron specific heat for polycrystalline samples of U(Rh,Ru)Ge plotted as c_m/T as a function of log$T$ for $0 \leq x \leq 0.50$. Figure taken from ref. [38].

The most compelling evidence for the presence of a QCP at x_{cr}=0.38 in U(Rh,Ru)Ge is provided by specific heat data taken on polycrystalline samples (see fig. 5.2 [38]). The data show that T_C, after a first increase, decreases gradually while at the same time the transition broadens and weakens. For x=0 and $T < 5$ K the f-electron specific heat can be described by an electronic (γ) and a spin wave (δ) term, $c_m(T)=\gamma T + \delta T^{3/2}$ [46]. Upon Ru doping an energy gap opens in the magnon spectrum. The specific heat of x=0.05 and x=0.10 is described by $c_m(T)=\gamma T + \delta T^{3/2} e^{-\Delta/k_B T}$ [46] where Δ is the energy gap in the magnon spectrum. At $x = x_{cr}$ the specific heat follows the predicted logarithmic behaviour for a FM QCP in 3D, $c_m(T) = -bTln(T/T_0)$, over one and a half decade in temperature. The temperature T_0 can be considered as an upperbound for the critical behaviour. In the case of $URh_{0.62}Ru_{0.38}Ge$, T_0 = 41 K. This indicates that experiments down to 0.4 K (hundred times smaller than T_0) indeed probe the quantum critical regime. The reduced f-electron entropy, about 50% of the local moment value Rln2 for $T < 15$ K,

confirms the itinerant nature of the FM state [38].

5.2 U(Rh,Ru)Ge polycrystalline series

In order to follow the evolution of the electron and phonon contributions in the U(Rh,Ru)Ge system, the Grüneisen ratio $\Gamma \propto \beta/c$ is studied. The specific heat of the U(Rh,Ru)Ge series was already reported in ref. [38, 92], and here we present thermal expansion data. Polycrystalline samples with different Ru concentrations ($0 \leq x \leq 0.60$) were prepared with the arc melting technique. All samples were annealed for 10 days at 900 °C. Their resistivity, magnetization and specific heat were measured and extensively reported in ref. [92]. The residual resistance ratio RRR of the polycrystalline samples amounts to ∼2. A more detailed characterization of the samples is given in ref. [92, 139]. Selected samples (x_{Ru}=0.10, 0.20, 0.38), used also for specific heat, were shaped into a cube with plane parallel surfaces in order to fit in the dilatometer.

5.2.1 Thermal expansion

Thermal expansion data were taken along the three orthogonal directions of the cube-shaped polycrystalline samples, in order to eliminate possible anisotropy effects due to crystallites with preferred orientations. The temperature range for the polycrystalline samples with x_{Ru}=0.10 and 0.20 is 2 K $< T <$ 150 K (glass dewar system) and for the polycrystalline sample with x_{cr}=0.38 1 K $< T <$ 20 K.

The coefficients of linear thermal expansion measured on the polycrystalline samples along the three orthogonal directions, α_i, where $i = x, y, z$, are reported in fig. 5.3. A strong anisotropy is present in all the polycrystalline samples. For $x = 0.20$ (middle frame) the three curves have the same shape but the step in α_y at the FM transition, $\Delta\alpha_y$, is almost 5 times bigger than $\Delta\alpha_x$ and $\Delta\alpha_z$. For the other samples (x=0.10 and x=0.38) the anisotropy is much more pronounced. In the sample with 38 at.% Ru, no FM transition is detected and upon lowering the temperature α_x and α_z become negative for $T < 4$ K, while α_y remains positive. For x=0.10 the anisotropy is more dramatic: the step in α_x at the FM transition is negative, while the steps in α_y and α_z are positive. This anisotropic behaviour in the polycrystals should not effect the true behaviour of the volume coefficient because $\beta = \sum_i \alpha_i$ with $i = x, y, z$. The origin of the anisotropy is not understood, but possibly crystallites with preferred directions form due to strong temperature gradients upon cooling after the arc melting process. The data along the three orthogo-

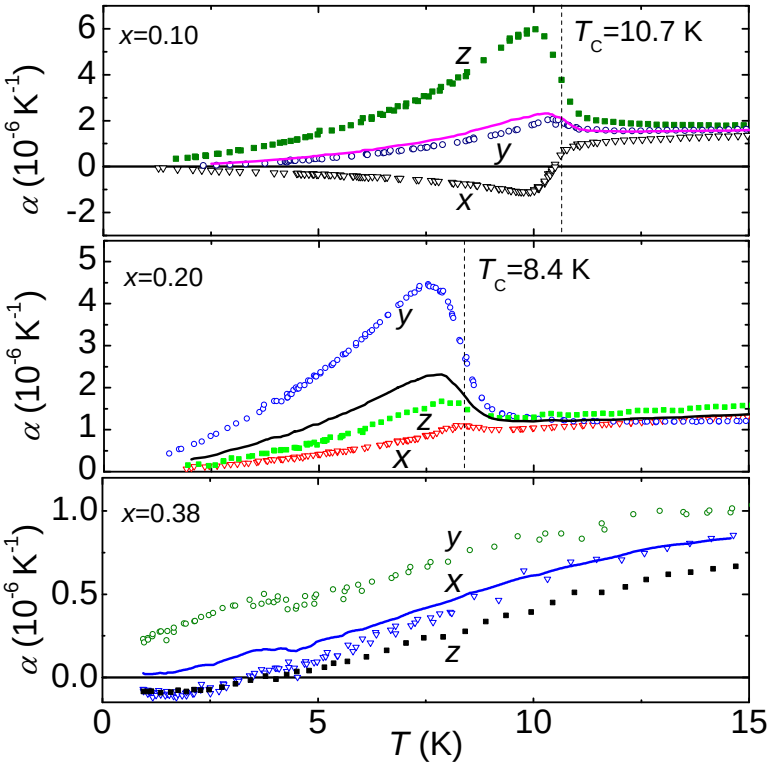

Figure 5.3: Coefficient of linear thermal expansion along the three orthogonal directions, x ($\triangledown$), y ($\circ$) and z ($\blacksquare$), of the polycrystalline samples of the U(Rh,Ru)Ge series with $x = 0.10$ (top frame), $x = 0.20$ (middle frame) and $x = 0.38$ (bottom frame). Notice the different vertical scales. The solid lines represent the averaged contribution $\beta/3$, while the dashed vertical lines mark the FM transition determined in each sample from β. The small structure at $T \sim 4$ K in the data for x=0.38 is due to a mismatch in the thermometer calibration.

nal directions are then averaged and the result $\beta/3$ is shown in the same figure for each sample (solid lines in fig. 5.3).

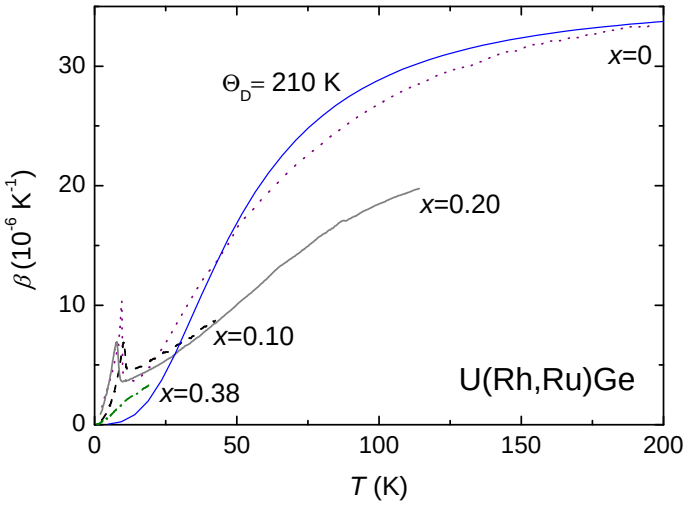

Figure 5.4: Coefficient of volume thermal expansion for polycrystalline $URh_{1-x}Ru_xGe$ with x=0.10 (dashed line), 0.20 (solid line) and 0.38 (dashed dotted line). For comparison the single crystal data for pure URhGe are shown [134] (dotted line). The thin line represents the Debye function with Θ_D=210 K.

In fig. 5.4 we plot β for the polycrystalline samples over a wide temperature range, together with the $\beta(T)$ data obtained for a single crystalline sample with $x = 0$ [134]. For temperatures $T > 50$ K these data on the pure compound roughly follow a phonon term (i.e. a Debye function) with Θ_D=210 K (thin line in the figure). This phonon contribution is calculated from the specific heat data (15 K $< T <$ 40 K) [92] assuming $\Gamma_{lat} = 2$ [49]. This analysis is in agreement with previous analysis of thermal expansion [139] and specific heat data [140, 141]. Notice that the volume thermal expansion for all polycrystalline samples for $T > 20$ K is smaller than for the undoped single crystal. This is unexpected because the lattice contribution should not change dramatically with chemical substitution.

The low temperature part of the $\beta(T)$ curves is presented as β/T versus T in fig. 5.5. Again the data on the undoped single crystalline URhGe sample are plotted for comparison. A sharp ferromagnetic transition at T_C=9.7 K characterizes the pure compound. The FM transitions present in the samples

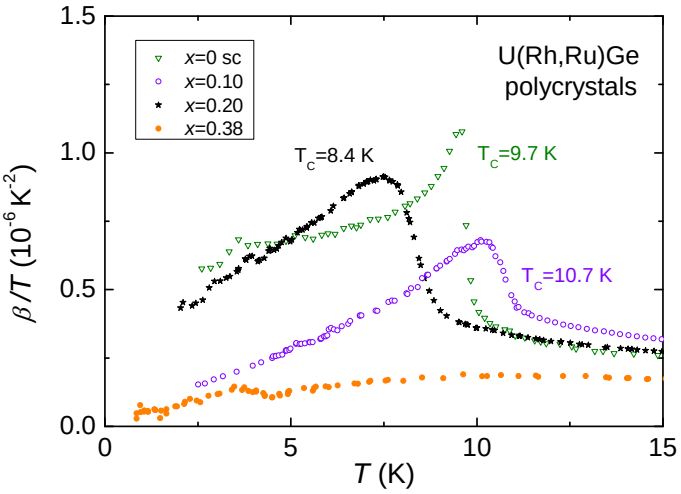

Figure 5.5: Coefficient of volume thermal expansion $\beta(T)$ divided by temperature versus temperature for polycrystalline samples with x=0.10, 0.20 and 0.38, as indicated. For comparison, the data on the undoped single crystalline URhGe sample taken from ref. [134] are plotted. The extracted Curie temperatures are indicated for each sample.

with x=0.10 and 0.20, at $T_{\rm C}$=10.7 K and 8.4 K respectively, are much broader due to the polycrystalline nature of the samples. These transition temperatures are determined from equal-area (length conserving) constructions for the broadened steps in α vs. T [142]. The data of the polycrystalline sample with $x_{\rm cr}$=0.38 do not show a FM transition down to 1 K, as expected from the phase diagram [92]. On the other hand the expected diverging behaviour $\beta/T \propto T^{-2/3}$ for a FM SDW QCP [23] is not observed.

It is interesting to consider the pressure dependence of the Curie temperature calculated using the Ehrenfest relation (eq. 2.21 in sec. 2.1.4) for the different doping levels. Since the specific heat has always a positive step Δc at $T_{\rm C}$ and, in this case, the step $\Delta\beta$ is positive as well, $dT_{\rm C}/dp > 0$ for x=0.10 and 0.20. Thus applying pressure drives the doped compound away from the critical point as for pure URhGe. The results are reported in table 5.1.

	$\Delta c/T_C$ (J/mol K^2)	$\Delta\alpha$ (10^{-6} K^{-1})	dT_C/dp (K/kbar)
x=0.10	0.21	3.09	0.05
x=0.20	0.18	4.60	0.09

Table 5.1: Hydrostatic pressure dependence dT_C/dp of the Curie temperature for polycrystalline samples $URh_{1-x}Ru_xGe$ with x=0.10 and x=0.20. dT_C/dp is calculated as $V_m\Delta\beta/(\Delta c/T_C)$,where V_m is reported in the following section 5.2.2.

5.2.2 Grüneisen ratio

The thermal expansion data are compared with the specific heat data to calculate the Grüneisen ratio:

$$\Gamma(T) = \frac{V_m}{\kappa_T}\frac{\beta(T)}{c(T)} \tag{5.1}$$

The molar volume V_m is calculated for each Ru-concentration from the lattice parameters reported in ref. [135]. We obtain V_m =3.364×10^{-5} m^3/mol, 3.357×10^{-5}m^3/mol, and 3.344×10^{-5} m^3/mol for x=0.10, 0.20, and 0.38 respectively. The compressibility is estimated at κ_T=0.8 Mbar^{-1} [134]. The calculated $\Gamma(T)$ curves are shown in fig. 5.6.

Apart from the curve for the sample at the critical concentration, all the curves are quite similar at high temperature ($T > 15$ K). For $T > 25$ K all the four curves level off around a value Γ_{lat}=2 [49]. The samples with x=0, x=0.10 and x=0.20 show a FM transition, sharp and clear for the first sample, broad for the other two samples. The sample with $x_{cr} = 0.38$ does not show a FM transition: $\Gamma(T)$ shows a broad maximum around 8 K. This is not expected: instead of diverging as predicted for a FM SDW QCP, $\Gamma(T)$ attains a value of 4 at T ∼9 K and smoothly decreases at lower temperatures.

5.2.3 Discussion

The Curie temperatures T_C determined by the thermal expansion measurements are in good agreement with previous results obtained by resistivity, magnetization, susceptibility and specific heat [92]. The resulting phase diagram $T_C(x)$ is shown in fig. 5.7.

At high temperatures $\beta(T)$ of the doped polycrystalline samples present a significantly smaller phonon contribution than reported for the undoped single crystal[1] (fig. 5.4). Such a difference is not observed in the specific heat

[1] As it will be shown in sec. 5.5, the same effect is observed for the doped single crystal with $x_{cr} = 0.38$. This observation allowed us to conclude that the smaller high temperature

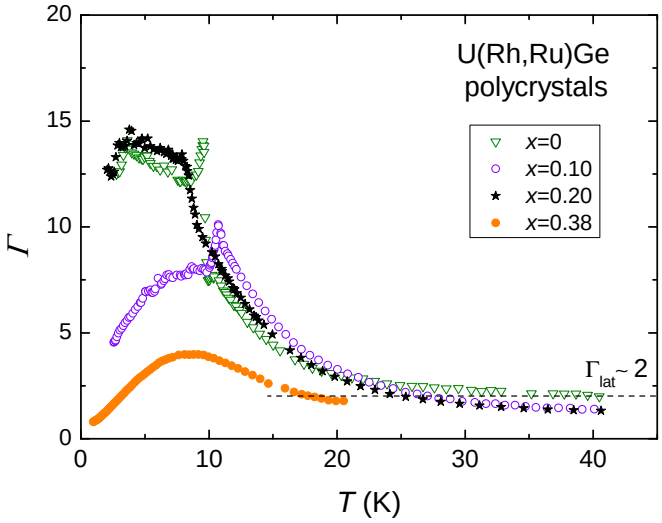

Figure 5.6: Temperature variation of the Grüneisen ratio $\Gamma(T)$ of the polycrystalline U(Rh,Ru)Ge series with x=0.10, 0.20, and 0.38. The data obtained for single crystalline URhGe are plotted for comparison [134]. The dashed line indicates the Grüneisen ratio $\Gamma_{\rm lat}$ ∼2.

data [92] which however extend up to 40 K only. The unexpected reduced phonon contribution is not yet understood. Possibly inelastic neutron scattering (INS) experiments could shed some light on this problem by determining the phonon dispersion curve. Thermal neutrons are a powerful probe to detect collective excitations such as phonons in crystals since they have both the right wavevector and energy to interact with phonons [143, 144].

The coefficient of volume thermal expansion $\beta(T)$ at low temperatures shows a pronounced f-electron contribution, as already was deduced from the specific heat [140] and the thermal expansion [139] data of URhGe. In refs. [92, 139, 140] the low temperature behaviour was attributed to an enhanced electronic contribution due to ferromagnetic spin fluctuations. In the ferromagnetic state the specific heat and the thermal expansion were characterized by a lattice contribution $\propto T^3$, a spin-wave contribution $\propto T^{3/2}$ and a ferromagnetic spin fluctuation contribution that leads to an enhanced electronic term, linear in T. Here a similar analysis is made for the doped polycrystalline samples.

contribution is not related to the the polycrystallinity of the samples but possibly to an effect of the doping.

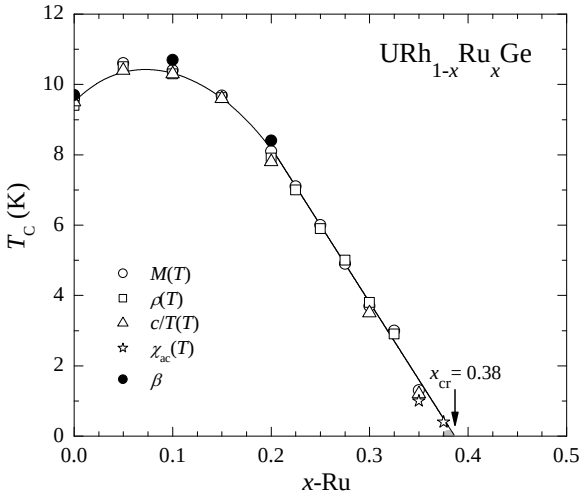

Figure 5.7: Curie temperature of $URh_{1-x}Ru_xGe$ alloys as a function of the Ru concentration, $T_C(x)$. The empty symbols are taken from ref. [92], while the filled symbols are determined by thermal expansion measurements on polycrystalline samples. The $T_C(0)$ data point is determined by thermal expansion measurements on the single crystalline sample, while the $T_C(0.38)$ (gray dot) is estimated to be zero since no transition is observed.

The lattice contribution is small at low temperature but it can be estimated from the specific heat data. From eq. 5.1 and considering only the lattice contribution $\beta_{\rm lat} = bT^3$ and $c_{\rm lat} = \tilde{\beta}T^3$ we calculate:

$$b = \frac{\kappa_{\rm T}}{V_{\rm m}} \Gamma_{\rm lat} \tilde{\beta} \tag{5.2}$$

where $\tilde{\beta}$ is the coefficient of the T^3 term in the specific heat. Considering $\Gamma_{\rm lat}$=2, β=0.60×10^{-3} J/mol K^4 (for all the samples) [38] and an average value $V_{\rm m}/\kappa_{\rm T}$=4.20×10^6 m^3/mol Pa, we estimate the coefficient of the phonon contribution to the thermal expansion $b = 3.0 \times 10^{-10}$ K^{-4}. This value is in good agreement with the low temperature slope of the Debye function presented in fig. 5.4. As it is clear from fig. 5.8, the phonon contribution its negligible at low temperature. Considering β/T as in fig. 5.5, the lattice and spin-wave contributions vanish at T=0. The linear electronic contribution, enhanced due to spin fluctuations, is estimated from the low temperature smooth ex-

trapolation of β/T when $T \rightarrow 0$. For x=0 at T=0, β/T=5.8×10^{-7} K^{-2} was obtained in ref. [139]. We obtain β/T=0.43×10^{-7} K^{-2} for x=0.10 and β/T=3.1×10^{-7} K^{-2} for x=0.20.

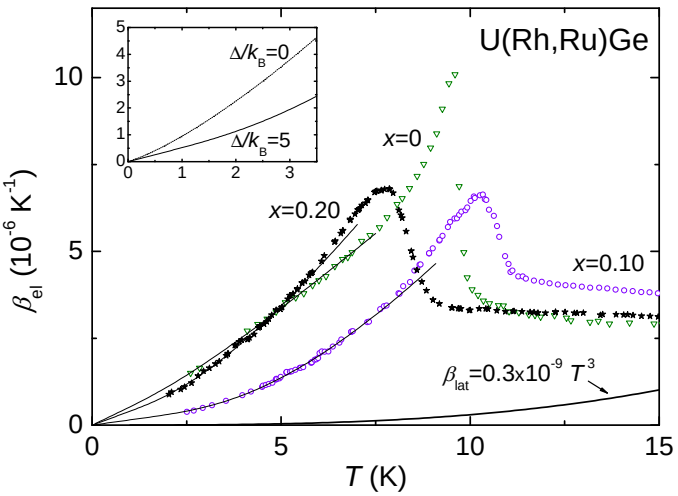

Figure 5.8: Coefficient of electronic volume thermal expansion β_{el} as a function of temperature of the polycrystalline series URh$_{1-x}$Ru$_x$Ge for x=0, 0.10, 0.20. The lines represent the fits $\beta_{el}(T) = cT + dT^{3/2}e^{-\Delta/k_BT}$ in the FM region. The lowest line represents the lattice contribution as indicated in the plot. Inset: low temperature fitting function of the URhGe data with non zero ($\Delta/k_B = 5$) or zero ($\Delta/k_B = 0$) energy gap, as indicated.

A more detailed analysis follows from the considerations made concerning the specific heat [38]. As mentioned previously, for x=0 $c_{el} = \gamma T + \delta T^{3/2}$ [38]. In the ordered state the c/T behaviour changes upon doping due to the opening of a gap in the magnon spectrum [46]. The electronic specific heat is described as $c_{el} = \gamma T + \delta T^{2/3}e^{-\Delta/k_BT}$ [38], where Δ is the energy gap and k_B is the Boltzmann constant. In the same spirit we analyse the electronic contribution to the volume thermal expansion in the FM region by:

$$\beta_{el}(T) = cT + dT^{3/2}e^{-\Delta/k_BT} \tag{5.3}$$

where c is coefficient of the enhanced electronic contribution linear in T, d is the coefficient of the spin-wave contribution and Δ accounts for the gap opening, as in the specific heat. The solid lines in fig. 5.8 represent the fits in

the FM region of the data sets of the samples with x=0, 0.10, and 0.20. The fit parameters are summarized in table 5.2.

	c [10^{-7} K^{-2}]	d [10^{-6} K$^{-5/2}$]	Δ/k_B [K]	T range
x=0	5.2 ± 0.6	0.43 ± 0.04	5 ± 2	$T < 6.5$ K
x=0.10	1.5 ± 0.1	1.4 ± 0.1	12 ± 1	$T < 7$ K
x=0.20	3.9 ± 0.2	1.1 ± 0.1	6.8 ± 0.8	$T < 5.5$ K

Table 5.2: Fit parameters for the data in the FM region for the samples with x=0, 0.10 and 0.20. The fitted function $cT + dT^{3/2}e^{-\Delta/k_BT}$ is used in the temperature range given by the last column. The maximum temperature considered is (2/3) T_C.

Notably a (very small) gap contribution is needed to fit the data of the pure compound. In the inset of fig. 5.8 the fit of the undoped compound data is compared with a similar fit with zero energy gap. The effect of a non-zero energy gap is to damp the spin-wave contribution, diminishing the number of magnons involved in the magnetic contribution to the thermal expansion. All the fits are approaching β_{el}=0 as $T \rightarrow$0. The value of the energy gap Δ for x=0.10 is in good agreement with the one reported in ref. [38]. The thermal expansion data on the sample with x=0.20 show that the gap becomes smaller for higher Ru concentration. However we cannot compare the value of Δ from the analysis of β with the one from the analysis of c/T for x=0.20 because, as printed out in ref. [38], the c/T curve seems to follow a different function from the ones of the lower doping levels. The values of c reported in the second column of table 5.2 are comparable with the extrapolated estimates of β/T reported in the beginning of this section. The β/T value for x=0.10, that did not appear to be in line with the magnitude of the surrounding doping levels, is comparable to the others when a non-zero energy gap Δ is taken into account in the fitting function.

A further analysis of β for x=0.38 is made in fig. 5.9, where we compare $\beta(T)$ and $c(T)$ measured on the same sample. The Grüneisen ratio is shown in the inset. The temperature dependence of $\beta(T)$ at low temperature is weaker than that of the specific heat $c(T)$. Concurrently the Grüneisen ratio slowly decreases at low temperatures in a quasi-linear way (1 K $\leq T \leq$ 5 K). This suggests an unusual behaviour $\beta_{cr} \propto T^2 \ln T$, since the specific heat follows the predicted behaviour for a FM SDW QCP in 3D, $c \propto$ -$T\ln(T/T_0)$ (critical behaviour), in the same temperature range. From the critical behaviour of the specific heat a value T_0=41 K was estimated (see sec. 5.1). Using the value of T_0 we can calculate the temperature below which $\Gamma(T)$ should start to increase: $T_{min} = T_0 e^{-3/2} \sim$9 K (see sec. 2.2.2). This is not observed in our data, as shown in fig. 5.9. We conclude this thermal expansion data on the

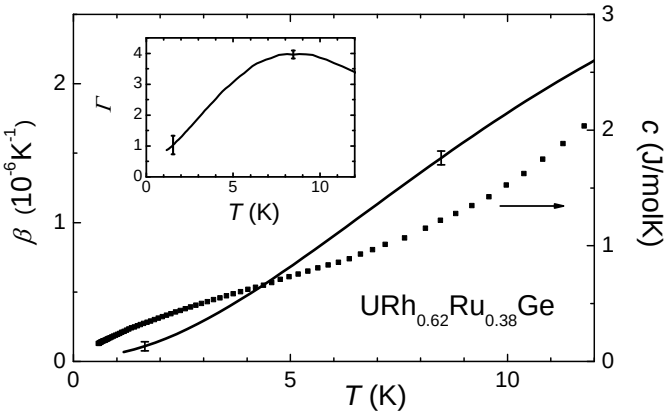

Figure 5.9: Thermal expansion β (left axis, line) and specific heat c (right axis, dots) as a function of temperature for polycrystalline $URh_{0.62}Ru_{0.38}Ge$. Inset: Grüneisen ratio as a function of temperature. In this figure the representative error bars for different temperature regimes are shown.

polycrystalline sample do not support the theory proposed in ref. [23].

5.3 Characterization of the single crystal ($x_N = 0.38$)

Ideally, the next step in our research programme is to investigate the Grüneisen ratio for a single crystal $URh_{1-x}Ru_xGe$, where $x = x_c$ refers to the critical concentration. However growing a single crystal with the right composition appeared to be very difficult. In the following we describe these attempts and characterize the prepared crystals. Three single crystalline samples were prepared with nominal concentration x_{Ru}=0.38 (two crystals labelled sc#1 and sc#2) and x_{Ru}=0.39 (one crystal labelled sc#3). The crystal sc#1 was characterized by means of resistivity ρ (sc#1-r) and susceptibility χ_{ac} (sc#1-ac), while crystals sc#2 and sc#3 were characterized by χ_{ac} only. In the vicinity of the QCP resistivity is not a good probe to detect the ferromagnetic phase transition as its signature becomes very weak. However a magnetic probe like ac-susceptibility is capable of detecting T_C close to the QCP. The value of T_C can be used as an indication of the real concentration of Ru in the sample (see fig. 5.7). Notice EPMA cannot resolve the concentration of Rh and Ru to better than 1% and that the Ru and Rh characteristic emission

lines are so close they overlap.

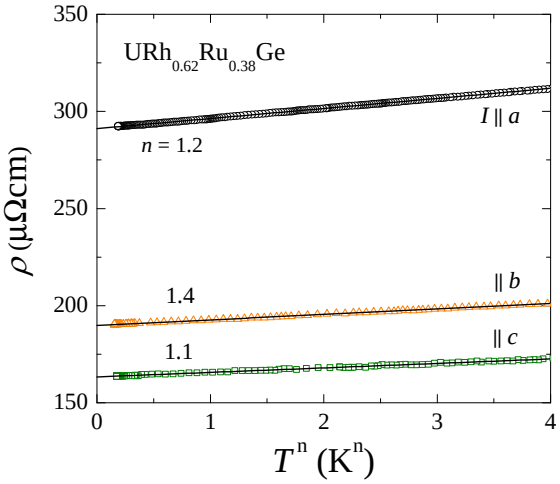

Figure 5.10: Resistivity of single crystalline U(Rh,Ru)Ge sc#1-r for a current I along the a, b and c axes (figure taken from ref. [92]). The resistivity is plotted versus T^n, where n represents a nFL exponent. The behaviour $\rho = \rho_0 + T^n$ is shown by the solid lines.

The ac-susceptibility, with a driving field $H_{ac} \sim 10^{-5}$ T, and resistivity were measured in the Heliox in the temperature range 0.24 K $< T <$ 6 K.

The resistivity of sc#1-r was measured by Dr. N. T. Huy [92] for a current I along the three crystallographic axes. The data are shown in fig. 5.10 in a plot of ρ vs T^n. No magnetic order is observed. The resistivity values for $I \| a$ are a factor 3/2 larger than for $I \| b$ and $I \| c$. For all the three axes, the residual resistance ratios are quite low, RRR ~2, as expected since the non-stoichiometry brings about disorder. The data are fitted as $\rho \sim T^n$ with exponents n of 1.2 ($I \| a$), 1.4 ($I \| b$) and 1.1 ($I \| c$). These values of n indicate non Fermi liquid (nFL) behaviour, but differ from n_{nFL}=5/3 as predicted for an itinerant FM QCP. This can be attributed to disorder. Notice, the data on a polycrystalline sample $URh_{0.62}Ru_{0.38}Ge$ (with a similar RRR) show n=1.2, as well as a recovery of the FL behaviour when a magnetic field of 10 T is applied [92]. We conclude that the exponent n extracted from the resistivity data is a clear sign of nFL behaviour, although its value is reduced by disorder.

AC-susceptibility measurements were performed on a part (labelled p#1-ac) of U(Rh,Ru)Ge sc#1 and the data are reported in fig. 5.11. Here the χ_{ac}

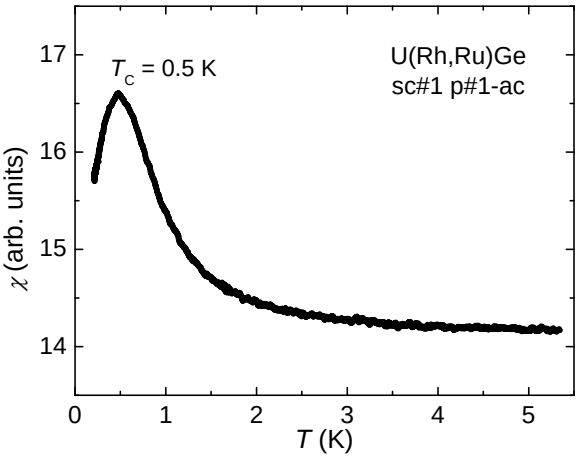

Figure 5.11: AC-susceptibility as a function of temperature for the single crystalline sample U(Rh,Ru)Ge sc#1 p#1-ac. The Ru-doping data indicates that magnetic order is present in the sample with T_C=0.5 K. The real concentration is estimated at 37.5 at.% Ru.

peak at T=0.5 K is a clear sign of FM order in the sample. Comparing the magnetic transition temperature to $T_C(x)$ for the polycrystalline samples (see fig. 5.7) we conclude that the sample orders ferromagnetically and that the real concentration of Ru is x=0.375, rather than the nominal concentration x_{cr}=0.38. The height of the peak in χ_{ac} is comparable to that of the polycrystalline sample with x=0.375 [92]. The same conclusion was drawn for a second piece of the same single crystal (from U(Rh,Ru)Ge sc#1 p#2-ac, data not shown).

For sc#2, a deeper characterization involving different parts of the sample was made, in order to investigate a possible composition gradient along the growth direction of the single crystal (fig. 5.12). Three pieces were taken from different parts of the single crystal sc#2 in the form of bars along the c axis. Ac-susceptibility data show that the different bars have different transition temperatures: T_C = 1 K for the top part, 0.7 K in the middle and T_C < 0.23 K at the bottom of the crystal. This shows that a composition gradient of ∼2 at.% Rh/Ru concentration is present in the as-grown crystal from top to bottom. For sc#2 we estimate the Ru concentration varies from $x \sim 0.36$ at the top to $x \gtrsim 0.38$ at the bottom. The gradient is related to the non-stoichiometry of the compound and to the growth technique (Czochralski

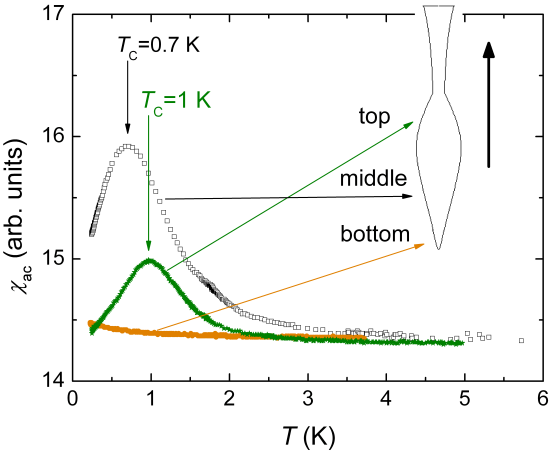

Figure 5.12: AC-susceptibility as a function of temperature for three samples taken from different parts of single crystalline U(Rh,Ru)Ge (sc#2). The Curie temperatures T_C, when present, are indicated by the arrows. In all cases $H_{ac} \sim 10^{-5}$ T was applied along the c axis. The arrow next to the sketch of the sample represents the pulling direction during the growth.

growth). Apparently in the beginning of the growth the crystal has the tendency to be Rh-richer than desired, towards the stoichiometric composition URhGe or due to a slightly different temperature at the liquid-solid interface. However, while the growth continues, the concentration of Rh in the melt decreases and the concentration of Ru in the solid increases. This results in a positive Ru gradient from top to bottom.

In order to slightly increase the Ru concentration in the crystal we decided to grow a crystal from a polycrystalline batch prepared with excess of Ru (x=0.39, sc#3). AC-susceptibility data taken on a piece of sc#3 were quite promising, showing no FM transition but a rather flat signal ($x > x_{cr}$) (data not shown). Following the results on the previous crystal sc#2, we expected to find a part of sc#3 with $x = x_{cr}$ (between the top and the middle part, according to the previous results). Nevertheless further measurements of the coefficient of thermal expansion showed that FM order was still present in the sample we selected from sc#3.

5.4 Thermal properties of the single crystal ($x_N = 0.38$)

The thermal expansion and the specific heat were measured on several single crystalline samples of U(Rh,Ru)Ge with $x \sim x_{cr}$. The specific heat was measured on two pieces of sc#1 and the thermal expansion on two pieces of sc#1, one piece of sc#2 and one piece of sc#3. The specific heat data were taken in the ^{3}He system in the temperature range 0.5 K $< T <$ 40 K and B=0, and in the range 0.5 K $< T <$ 15 K for $B \neq 0$. The thermal expansion data were taken in both the Heliox (0.24 K $< T <$ 15 K) and the glass dewar system ($T >$ 2 K). The data on the specific heat of $URh_{0.62}Ru_{0.38}Ge$ sc#1 p#1 were already reported in ref. [92] with a detailed analysis. These data are discussed in the following discussion section where a comparison with the thermal expansion data is made.

5.4.1 Thermal expansion

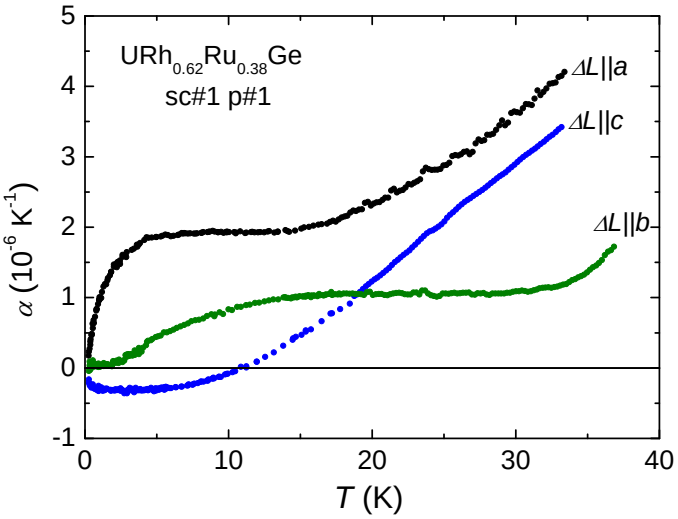

Figure 5.13: Coefficient of linear thermal expansion versus temperature of $URh_{0.62}Ru_{0.38}Ge$ sc#1 p#1. Data are taken along the three orthogonal axes as indicated.

The linear thermal expansion coefficient of $URh_{0.62}Ru_{0.38}Ge$ sc#1 p#1 is reported in fig. 5.13. The data reveal a strong anisotropy for the three crystallographic axes. Similarities with $\alpha(T)$ measured on the polycrystalline sam-

ple, reported in fig. 5.3, are present. This indicates that the anisotropy of the polycrystalline sample is related to the presence of preferred directions during sample preparation. For $T > 30$ K the data along the three crystallographic axes have an similar slope $d\alpha/dT$. For $T > 35$ K the Debye contribution is dominant. Upon lowering the temperature, α_a first steadily decreases, then reaches a plateau value for 15 K, and below 5 K rapidly goes to 0. The steepest temperature variation at low temperature is observed for α_a. Instead α_c is negative for $T < 10$ K and smoothly approaches T=0. The behaviour of α_b is similar to that of α_a, with a long plateau below 30 K, but α_b does not decrease as dramatically as α_a to zero when $T \to 0$.

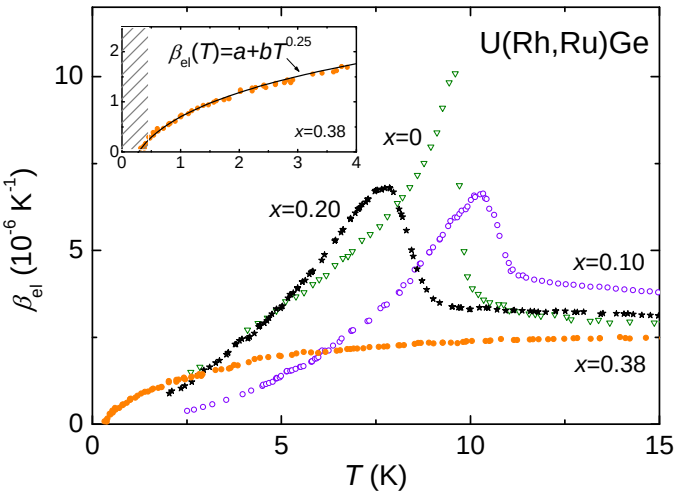

Figure 5.14: Electronic contribution to the coefficient of volume thermal expansion of the U(Rh,Ru)Ge series for x=0 (single crystal), x=0.10, x=0.20 (both polycrystalline samples) and x=0.38 (single crystal sc#1 p#1). Inset: Electronic contribution to the coefficient of volume thermal expansion of the single crystalline sample with x=0.38. The solid line represents a fit to $y = a + bT^n$ with n=0.25 for $T < 5$ K (see sec. 5.4.2). The dashed area indicates the ferromagnetic region as determined by the ac-susceptibility data.

The coefficient of volume thermal expansion of the sample with $x = 0.38$ (sc#1 p#1) is calculated by adding up the values of α along the three crystallographic axes, $\beta = \alpha_a + \alpha_b + \alpha_c$. The electronic contribution is obtained by subtracting the lattice contribution, $\beta_{el} = \beta - bT^3$, with $b = 0.30 \times 10^{-9}$ K^{-4}, as done for the polycrystalline samples (see sec. 5.2.3). In fig. 5.14 we compare

this result with $\beta_{\rm el}$ of the samples with lower Ru concentration (sec. 5.2). Upon lowering the temperature, no magnetic transition peak is detected for $x = 0.38$ down to the lowest measured temperature and $\beta_{\rm el}$ smoothly approaches T=0 as $\beta_{\rm el} \sim a + T^n$ where $n = 0.25 < 1/3$.

5.4.2 Discussion

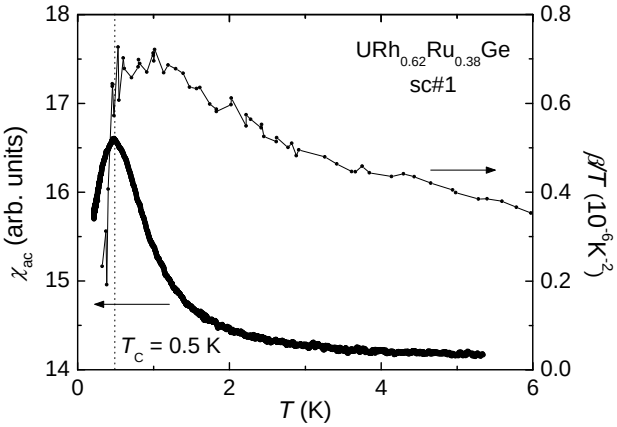

Figure 5.15: Comparison between the coefficient of volume thermal expansion divided by the temperature β/T (right vertical axis) and the ac-susceptibility $\chi_{\rm ac}$ (left vertical axis) of $URh_{0.62}Ru_{0.38}Ge$ sc#1 p#1. The FM transition temperature $T_{\rm C}$=0.5 K, corresponding to the peak of $\chi_{\rm ac}$ (vertical dotted line), accounts for the drop in β/T for $T < 1$ K.

In fig. 5.15 we compare $\beta(T)/T$ of U(Rh,Ru)Ge sc#1 p#1 with the ac-susceptibility $\chi_{\rm ac}$ measured on U(Rh,Ru)Ge sc#1 p#1-ac (sec. 5.3 and fig. 5.11). Upon lowering the temperature $\beta(T)/T$ slowly increases. For $T < 1$ K the increase stops. The comparison shows that $\beta(T)/T$ and $\chi_{\rm ac}$ drop at the same temperature T=0.5 K, which reveals that the drop in $\beta(T)/T$ is related to the magnetic order present in the sample. The presence of the FM phase is less evident in $\beta(T)$. A simple power law fit of these data for temperatures $T < 5$ K gives

$$\beta_{\rm el}(T) = (-1.9 \pm 0.1) \times 10^{-6} + (2.6 \pm 0.1) \times 10^{-6} T^{0.25 \pm 0.01}$$

with a temperature exponent close to the theoretically predicted value 1/3 and an unexpected negative term for $T = 0$ (fig. 5.14). This term is explained

considering that FM order is still present in the sample and a transition will occur at lower temperature. In this option $\beta(T)$ does not drop to zero with a power law but becomes negative due to a phase transition peak for $T < 0.3$ K. This hypothesis is corroborated by the fact that $\beta(T) = 0$ at $T \sim 0.28$ K. The possibly negative $\Delta\beta$ at the FM transition implies a negative response of T_C to pressure. In U(Rh,Ru)Ge, in the vicinity of the FM QCP, applying pressure would therefore depress the Curie temperature. The value $\Delta\beta$ at T_C changing sign when approaching the QCP was observed also for $CePd_{1-x}Rh_x$ [127, 145], the other example of a FM QCP reported in the literature, and for AFM compounds (for instance $CeIn_{1-x}Sn_x$ [146]). The sign change is still under discussion [147].

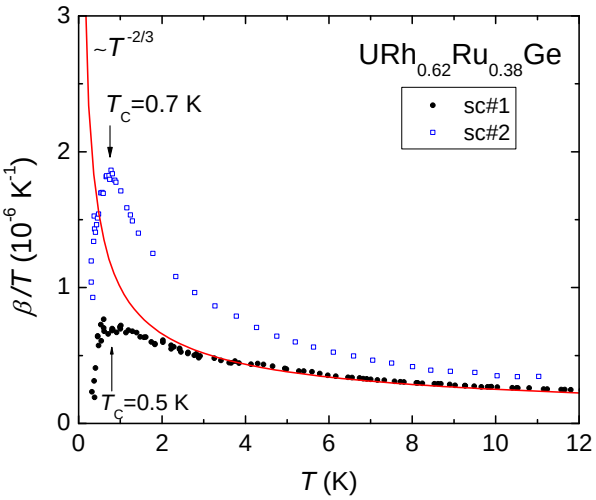

Figure 5.16: Coefficient of volume thermal expansion divided by temperature β/T as a function of the temperature for $URh_{0.62}Ru_{0.38}Ge$ sc#1 and sc#2. The arrows mark the FM transition temperatures T_C=0.5 K for sc#1 and T_C=0.7 K for sc#2. The line is a fit to the expected critical behaviour $\beta \propto T^{-2/3}$ of the data of sc#1 for $T > 3.5$ K.

In order to follow the FM contribution as a function of the concentration, we next present the thermal expansion data taken on a piece of the second crystal (U(Rh,Ru)Ge sc#2, for which the ac-susceptibility was mapped along the length of the crystal). The sample under study was cut between the bottom ($x > 0.38$) and the middle part ($x \sim 0.37$) of the crystal (see fig. 5.12). We therefore expect a sample with Ru-concentration $x \sim 0.38$. To check the

effective Ru-concentration of the sample, we plot β/T versus T, since the low temperature FM transition is more visible in this way. In fig. 5.16 β/T for sc#1 and sc#2 are compared. The FM transition is revealed by the drop of β/T at T_C, as previously discussed. The data show T_C=0.7 K for sc#2, meaning that $x = 0.37$. The results of α_a, α_b and α_c for sc#1 and sc#2 are compared in fig. 5.17. Since the a-axis qualitatively shows the same behaviour, while in α_b and α_c of sc#2 the FM transition is clearly visible (the Curie temperature is indicated by a maximum (minimum) in α_b (α_c)), we conclude that the b and c axes are more sensitive to FM order. Notice that these two samples were prepared at the same nominal concentration x=0.38, both have a lower and very similar ($\Delta x_{Ru} \sim 0.005$) effective concentration, but the thermal expansion coefficients change considerably. This result shows how small changes in Rh/Ru concentration strongly influence the behaviour of β close to the FM QCP in U(Rh,Ru)Ge.

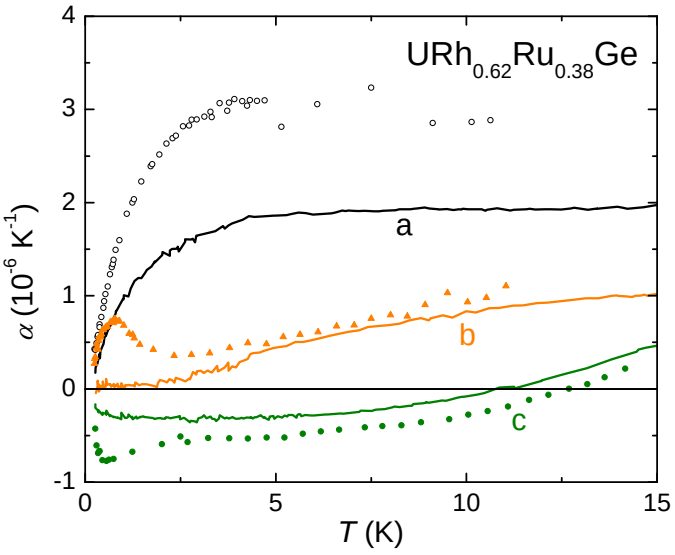

Figure 5.17: Coefficient of linear thermal expansion of samples $URh_{0.62}Ru_{0.38}Ge$ sc#1 and sc#2. The solid lines give $\alpha(T)$ for sc#1 while the symbols give $\alpha(T)$ for sc#2. An identical colour is used for the same crystallographic axes of the different crystals.

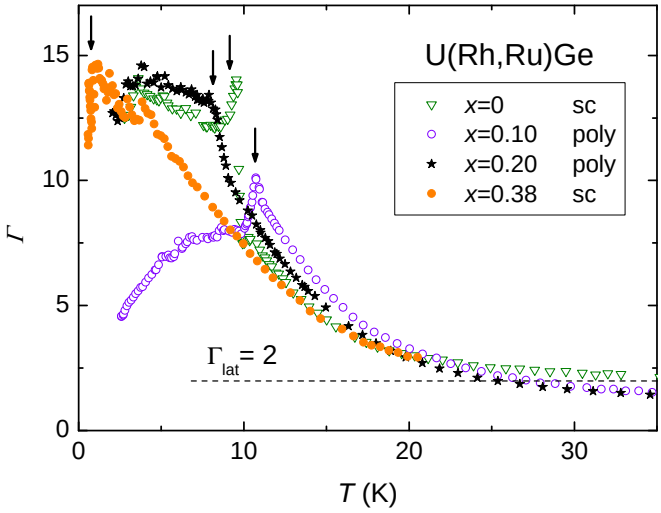

Figure 5.18: Grüneisen ratio of the U(Rh,Ru)Ge series. The dashed line indicates the theoretical value of lattice contribution to the Grünisen parameter, $\Gamma_{\rm lat} = 2$. The arrows indicate the FM transition temperatures for each concentration.

5.4.3 Grüneisen ratio

The Grüneisen ratio of $URh_{0.62}Ru_{0.38}Ge$ sc#1 is reported in fig. 5.18 together with the data of the samples with a lower Ru concentration. For calculating the Grüneisen ratio (eq. 5.1) the same molar volume $V_{\rm m}$ and compressibility $\kappa_{\rm T}$ as used for the polycrystalline sample at the critical concentration are taken. At high temperatures the single crystal data are similar to the data of the other samples. For $T > 20$ K all the data sets attain a similar value and reach $\Gamma_{\rm lat} = 2$ near $T \sim 30$ K. At low temperatures a clear depression of the Curie temperature is visible, as in the FM phase diagram [38]. The data level off at $\Gamma_{\rm FM}$=14 [139]. For $x = 0.38$ the FM transition is observed as a drop in the data at the Curie temperature $T_{\rm C} = 0.5$ K. Clearly, $T_{\rm C} \to 0$ but the ferromagnetism is not yet fully suppressed.

5.5 Critical contribution in single crystalline $URh_{0.62}Ru_{0.38}Ge$

In order to investigate the expected criticality in U(Rh,Ru)Ge we analyse next the thermal expansion, the specific heat and the Grüneisen parameter of sc#1 p#1. The thermal expansion and specific heat data have been taken on the same single crystalline sample. The Grüneisen ratio is calculated using eq. 5.1.

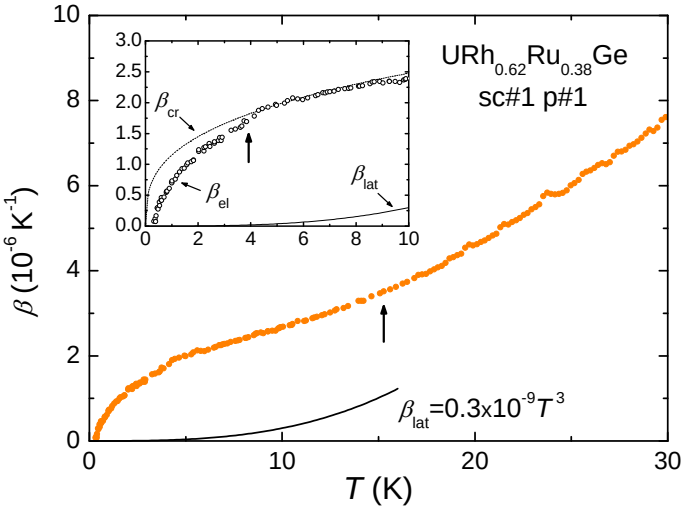

Figure 5.19: Coefficient of volume thermal expansion of $URh_{0.62}Ru_{0.38}Ge$ sc#1 p#1. The arrow in the plot marks the low temperature region where $\beta(T)$ deviates from a $T^3 + T$ behaviour (phononic and electronic contributions). The solid line represents the lattice contribution as indicated. Inset: electronic coefficient of volume thermal expansion $\beta_{\rm el}(T)$=$\beta(T) - bT^3$ as a function of temperature. The dashed line indicates a fit to $\beta_{\rm cr}(T) = T^{1/3}$ for the data in the temperature range 3.5 K $< T <$ 8 K. The arrow marks the deviation of $\beta_{\rm el}(T)$ from $\beta_{\rm cr}(T)$.

In the present case, at low temperature, four different contributions are present for both the thermal expansion and the specific heat: a phonon contribution ($\sim T^3$), an enhanced electronic contribution ($\sim T$), a FM contribution and a critical contribution (we expect $\beta_{\rm cr} \sim T^{1/3}$ and $c_{\rm cr} \sim -T\ln T/T_0$). The FM contribution is centered around $T_{\rm C} \sim 0.5$ K, as we concluded from the ac-susceptibility data. Since the critical contribution is supposed to be negligible at high temperature, we assume that for $T >$ 15 K a non-critical

contribution is given by the sum of the linear electronic term plus the phonon term ($T + T^3$). For the thermal expansion data the fit for $T > 15$ K results in:

$$\beta_{\text{no-cr}}(T) = (2.14 \pm 0.01) \times 10^{-7}\ T + (0.44 \pm 0.01) \times 10^{-10}\ T^3$$

where the extracted $\beta_{\text{no-cr}}/T$ at $T = 0$ (T-linear term) is in agreement with the previous values on the crystals with x=0 and x=0.20 while the value $b = 0.44 \times 10^{-10}$ K^{-4} is one order of magnitude smaller than the one estimated from the specific heat data. The origin of this inconsistency is still unclear, but is connected to the different high temperature β for pure and doped samples reported in fig. 5.4 (see sec. 5.2.3. At high temperature the doped compounds presented a much smaller phonon contribution (comparable with the value of b from the fit) than the one of the undoped compound (comparable with the estimation made using the specific heat data). Nevertheless, this does not influence our analysis since at low temperature the phonon contribution is negligible (as shown in fig 5.19 by the solid line) and the T-linear term is not affected by such a difference in the phonon contribution (within 3%). Therefore the value used previously, $b = 0.30 \times 10^{-9}$ K^{-4}, is used in the following. The electronic contribution $\beta_{\text{el}}(T) = \beta(T) - bT^3$ is plotted in the inset of fig. 5.19 together with the expected critical behaviour for a 3D FM QCP (dotted line) assuming α_{cr} for 3.5 K $< T <$ 8 K. The deviation from the expected $T^{1/3}$ behaviour of β_{el} for $T <$ 3.5 K is attributed to the FM order.

A slightly different approach to the analysis of β_{el} is presented in fig. 5.20. Here the data are plotted as a function of $T^{1/3}$. In the range 3.5 K $< T <$ 8 K the data are fitted by a linear function with zero intercept

$$\beta_{\text{el}}(T) = (1.135 \pm 0.002) \times 10^{-6} T^{1/3}. \tag{5.4}$$

The deviation from the linear fit below 3.5 K is again attributed to the FM transition. This analysis supports the previous one, although the temperature range of the fit is too small to draw any firm conclusion.

The specific heat appears to be less sensitive to magnetic order than the thermal expansion, as observed for the polycrystalline sample as well. Nevertheless, at low temperatures a deviation from the critical behaviour is observed (see fig. 5.21). The measured data are fitted in the temperature range 11 K $< T <$ 22 K with a polynomial function (electrons $\sim T$ and phonons $\sim T^3$)

$$\frac{c_{\text{no-cr}}}{T} = (0.086 \pm 0.001) + (6.03 \pm 0.05) \times\ 10^{-4} T^2$$

with γ=86 mJ/mol K^2 and β=0.603 mJ/mol K^4. The values of γ and β are comparable to the values obtained on the polycrystalline samples [38, 92]. The electronic contribution to the specific heat $c_{\text{el}}(T) = c(T) - \beta T^3$ is reported in

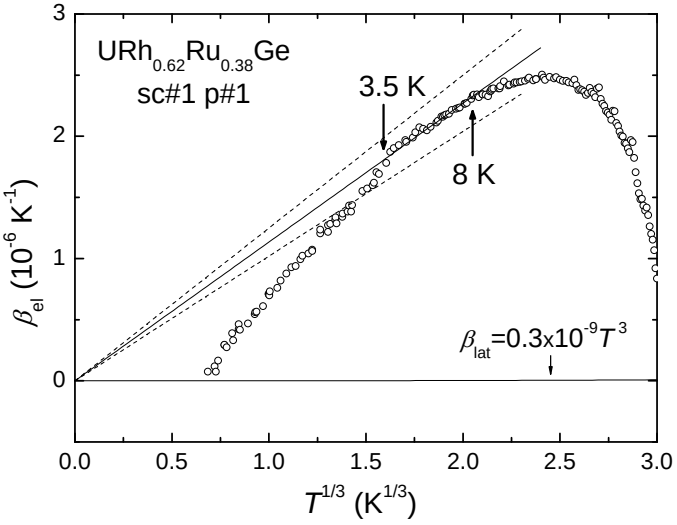

Figure 5.20: Electronic contribution to the volume thermal expansion of $URh_{0.62}Ru_{0.38}Ge$ sc#1 p#1 as a function of $T^{1/3}$. The solid line represents the linear fit to the data in the temperature range 3.5 K $< T <$ 8 K (indicated by the arrows), with zero intercept. The dashed lines are the confidence lines given by the linear fit. The lower solid line represents the lattice contribution as indicated.

the same plot (fig. 5.21, empty circles). The data for 1 K $< T <$ 8 K are fitted by a function linear in ln$T$:

$$c_{\rm el}(T)/T = (0.222 \pm 0.001) + (-0.056 \pm 0.001)\ln T. \qquad (5.5)$$

As in the thermal expansion, a deviation from the critical behaviour is observed at low temperature ($T <$ 1 K), where the FM transition takes place.

For the single crystalline sample we calculate $T_0 = 51$ K (where the linear fit intercepts the horizontal axis), comparable with the value obtained for the polycrystalline sample. For temperatures $T \ll T_0$ the critical behaviour becomes important. According to the previous consideration, we expect a divergence for Γ in the temperature range 3.5 K $< T <$ 8 K, much below T_0 and above the temperature for magnetic order. In fig. 5.22 the electronic contribution of $\Gamma_{\rm el} \propto \alpha_{\rm el}/c_{\rm el}$ for $URh_{0.62}Ru_{0.38}Ge$ sc#1 p#1 is reported. The value of T_0 is outside our temperature range. We compare our experimental data with the critical behaviour extracted from the previous analysis, $\Gamma_{\rm cr} \propto \alpha_{\rm cr}/c_{\rm cr}$ (dashed line). The dashed curve is the predicted critical behaviour

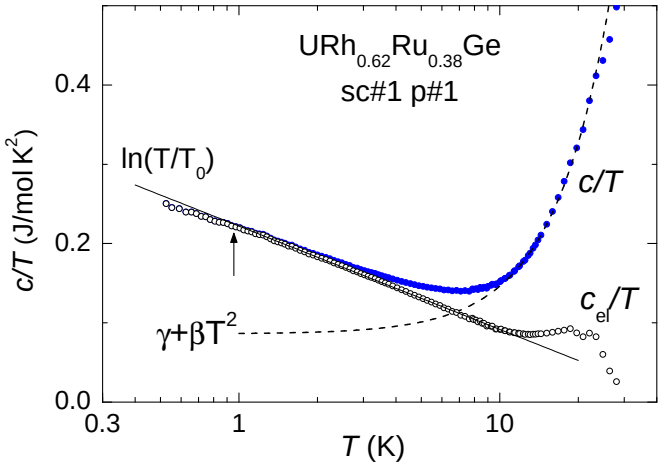

Figure 5.21: Specific heat divided by temperature of $URh_{0.62}Ru_{0.38}Ge$ sc#1 p#1 on logarithmic temperature scale. The filled dots represents the measured data. The high temperature fit to $c_{\text{no-cr}}(T)/T = \gamma + \beta T^2$ (dashed line) accounts for the electronic and phononic contribution. The empty circles represents the electronic contribution to the specific heat, $c_{\text{el}}(T) = c(T) - \beta T^3$. The solid line along these data is the linear fit (theoretical critical prediction) for 1 K $< T <$ 8 K. The arrow indicates the deviation from the critical behaviour for $T <$ 1 K.

obtained by dividing the fit to the thermal expansion (eq. 5.4) by the fit to the specific heat (eq. 5.5) and multiplying by $V_{\text{m}}/\kappa_{\text{T}}$. We observe a good agreement between the data and the fit in the considered temperature range. The divergence of Γ illustrated by the dashed line in fig. 5.22 differs from the AFM case [15, 148, 149] (see also sec. 2.2.2). Notably, the predicted diverging function is not monotonically decreasing with T but has a minimum at $T_{\text{min}} = T_0 e^{-3/2}$. The divergence possibly occurs at very low temperatures after a plateau that is possibly wide in temperature (depending on the parameters of the function, as illustrated in fig. 2.2). In our case T_{min}=11 K and the wide $\Gamma(T)$ plateau is evident in fig. 5.22. Moreover, the divergence takes place in the region of magnetic order, preventing its observation.

Although we do not observe a diverging Γ, the previous analysis brings us to a different conclusion than the one drawn for $CePd_{1-x}Rh_x$. In the latter system a non-diverging Γ provided evidence for the absence of a quantum critical point. Detailed magnetization and ac-susceptibility experiments showed

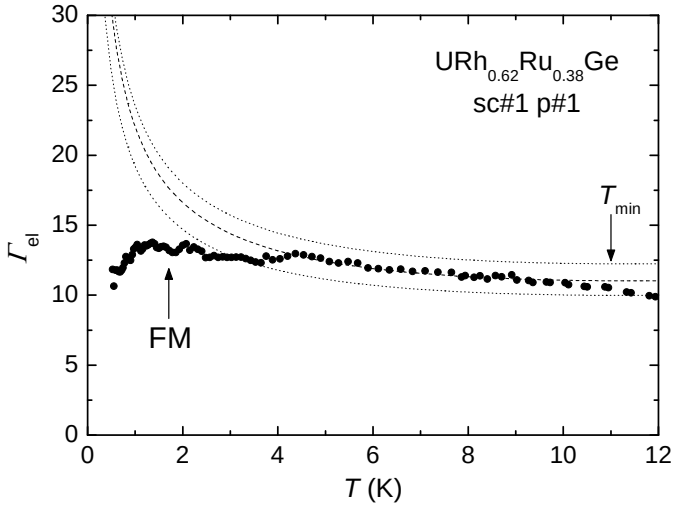

Figure 5.22: Electronic Grüneisen ratio as a function of the temperature. The dashed curve is the ratio between the fits of the thermal expansion and the specific heat data, multiplied by $V_{\rm m}/\kappa_{\rm T}$. The dotted lines are the same as the dashed line but using the confidence lines given by the linear fit of the thermal expansion data. The arrow with FM indicates $T_{\rm C}$ measured by $\chi_{\rm ac}$, while $T_{\rm min}$ marks the minimum of the dashed line function.

that the suppression of the FM order by Rh-doping in CePd leads to the formation of a peculiar Kondo-cluster-glass [128]. The presence of clusters and the power-law corrections to susceptibility and magnetization indicate that the expected QPT is replaced by disordered phases, possibly like the Griffiths one [129]. In the case of U(Rh,Ru)Ge, the single crystal data presented in this section are not inconsistent with the diverging function predicted by ref. [23].

5.6 Summary

In this chapter we have investigated the feasibility to tune URhGe by Ru doping to the FM QCP (at 38 at.% Ru) and probe the diverging Grüneisen ratio. The results reported in this chapter allow us to draw a number of conclusions, which in turn raise several new questions.

First, we address the results obtained on the polycrystalline samples. The thermal expansion of a series of polycrystalline $URh_{1-x}Ru_xGe$ samples

(x=0.10, 0.20 and 0.38) was measured and the coefficient of volumetric thermal expansion $\beta(T)$ was determined. The Grüneisen ratio was calculated using specific heat data taken on the same samples [92]. For the samples with x=0.10 and 0.20 a large contribution to $\beta(T)$ due to ferromagnetic order was observed, with Curie temperatures of 10.7 K and 8.4 K, respectively. The data below $T_{\rm C}$ were analysed using a spin wave contribution with a gap $\Delta/k_{\rm B}$ of the order of 10 K, in close analogy with the analysis of the specific heat [92]. From the step-sizes of $\beta(T)$ at $T_{\rm C}$ we derived - using the Ehrenfest relation - that upon applying pressure the Curie temperature increases at a rate of 0.05 and 0.09 K/kbar, respectively. The sample prepared at the critical concentration for FM order, x=0.38, did not show ferromagnetic order, as expected. From its Grüneisen ratio it was shows an unusual $\beta_{\rm cr} \sim T^2 {\rm ln}T$ behaviour, rather than the predicted diverging $\beta \sim T^{-1/3}$. Nevertheless, when we compare the results of the different samples, a steady rise of $\Gamma(T)$ is observed in the paramagnetic regime on approach of the ferromagnetic transition (see fig. 5.6): from $\Gamma(T) \sim 2$ at 40 K to $\Gamma(T) \sim 12-14$ just above $T_{\rm C}$. A possible reason why the enhancement of the Γ value towards the critical point does not persist for x=0.38 might lie in the strong effects the precise composition and sample homogeneity may have on the behaviour of $\beta(T)$ close to the critical point, as was found in the single crystal data.

Several single crystals of $URh_{1-x}Ru_xGe$ with $x \sim 0.38$ were prepared using the Czochralski technique. Characterization of the samples by means of resistivity and ac-susceptibility together with thermal expansion measurements showed it was not possible to obtain single crystals precisely at the critical concentration $x_{\rm cr}$: a typical variation of 2% in the Rh/Ru ratio was observed along the crystal pulling direction. Thermal expansion measurements were performed on several (pieces of the) crystals. All samples showed a finite Curie temperature, typically of the order of 0.5 K, which complicated the analysis of the data. The Grüneisen ratio of a single crystal with $T_{\rm C}$=0.5 K was investigated in detail. Thermal expansion measurements were carried out along the three orthorhombic axes down to 0.24 K, and the specific heat was investigated down to 0.5 K [92]. The coefficient of thermal expansion is strongly anisotropic. The largest contribution to $\beta(T)$ is due to the coefficient of linear thermal expansion along the orthorhombic a axis. The $\beta(T)$ and $c(T)$ data follow the theoretical functions for a 3D FM QCP, albeit in a small temperature window T=3.5-8 K, above the region of the FM transition. A deviation from this behaviour for $T < 1$ K suggested an anomaly at lower temperature associated to the magnetic transition, as confirmed by the ac-susceptibility data. The deviation in $c(T)$ occurs at lower temperatures than that in $\beta(T)$. This can be understood considering that the thermal expansion probes the

pressure dependence of the entropy while the specific heat the temperature dependence [54]. β is therefore more sensitive than c to (chemical-)pressure variation of the system. The higher sensitivity of β compared to c near a QCP was already observed in the case of $CeCu_{6-x}Ag_x$ [150, 151].

In fig. 5.23 we summarize the thermal expansion (upper frame) and specific heat (middle frame) data of $URh_{1-x}Ru_xGe$ discussed in this chapter. We included single-crystal data for x=0 and x=0.38 and polycrystal data for x=0.10 and 0.20. In the lower frame the temperature variation of the Grüneisen ratio is presented. For β and c the phonon contribution is considered as well in calculating the Grüneisen ratio. The close-to-critical behaviour stands out for the sample with x=0.38. In contrast to the polycrystal data, β(T) of the single crystal steadily increases with decreasing temperature and attains a value of ∼14 before magnetic order sets in. We conclude that although we do not observe a divergence of $\Gamma(T)$ for $T \rightarrow 0$, the data are not at odds with the FM QCP scenario presented in ref. [23]. This suggests that the U(Rh,Ru)Ge system remains an arresting laboratory tool to study FM quantum criticality. However, it is imperative to significantly improve the homogeneity of the crystals. Since the Czochralski growth is based on the stoichiometry of the sample, it is natural to ask whether such a technique is the most effective for this case. Possibly a higher homogeneity might be accomplished by using the floating zone technique in a mirror furnace.

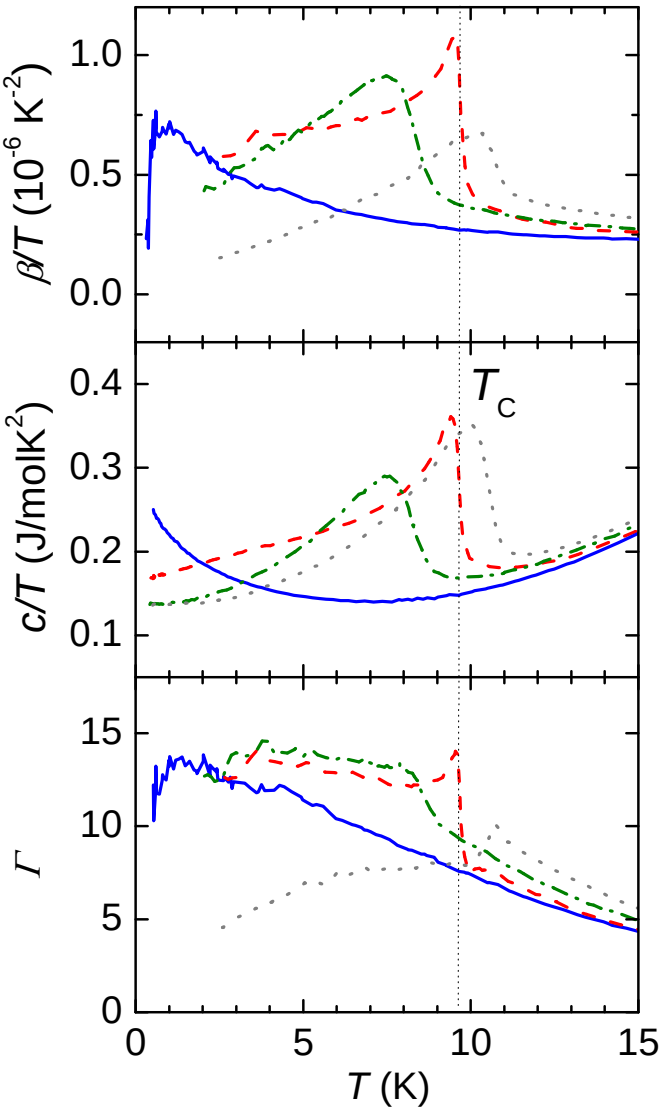

Figure 5.23: From top to bottom: coefficient of volume thermal expansion β divided by temperature, specific heat c divided by temperature and Grüneisen ratio Γ. The data are taken on the single crystalline URhGe (dashed line), on the polycrystalline samples at x=0.10 (dotted line) and at x=0.20 (dashed-dotted line) and on the single crystalline sample $URh_{0.62}Ru_{0.38}Ge$ sc#1 p#1 (solid line). The dotted line marks the Curie temperature of URhGe.

6 Coexistence of superconductivity and ferromagnetism in UCoGe

dunque ogni cosa giusta rivela il suo contrario

Caparezza

The superconducting ferromagnet (SCFM) UCoGe was discovered in Amsterdam in 2006 [29]. Just like in URhGe, superconductivity and ferromagnetism coexist at ambient pressure. The ordered moment of UCoGe, $m_0 = 0.07\ \mu_B$, is very small which demonstrates superconductivity occurs close to the border of FM order [29]. Recent work has shown that the FM QCP can be attained by applying moderate pressure (~ 0.1 GPa) and that superconductivity is enhanced at the critical point [42]. This makes UCoGe an excellent laboratory tool to study spin-fluctuation mediated superconductivity.

In this chapter we investigate the thermal properties of polycrystallline as well as single crystalline samples by means of thermal expansion and specific heat. The measurements provide solid evidence for bulk superconductivity. Thermal expansion measurements in an applied magnetic field on single crystals of UCoGe are used to investigate the response of the SC and FM phases to a magnetic field.

6.1 Introduction

In the search for a FM quantum critical point in URhGe, several alloy systems have been investigated [92, 135]. Among these is the series U(Rh,Co)Ge. The end compound UCoGe was reported to be paramagnetic down to 1.5 K according to magnetization, resistivity [137, 152] and specific heat measurements

[153]. This provided the motivation to alloy URhGe with Co. Magnetization data taken on polycrystalline $URh_{1-x}Co_xGe$ samples show that, upon doping, T_C first increases, displays a broad maximum near x=0.6 (T_C^{max}=20 K) and then rapidly drops to 8 K for x=0.9 [135, 154]. Measurements for x=1.0 showed that UCoGe is, unlike as was concluded previously [137, 152, 153], a weak itinerant ferromagnet. Moreover metallic ferromagnetism coexists with SC at ambient pressure [29].

The intermetallic compound UCoGe crystallizes in the orthorhombic TiNiSi structure [152, 155] with space group Pnma. It belongs to the family of the UTX compounds, where T is a transition metal and X is Si or Ge, like URhGe. The lattice constants of the conventional unit cell as determined by X-ray diffraction are a=6.852(1) Å, b=4.208(1) Å and c=7.226(1) Å [155].

Resistivity, ac-susceptibility and specific heat measurements provide evidence for a FM transition at T_C=3 K and for a SC transition at T_{sc} = 0.61 K (see fig. 6.1, polycrystalline sample labelled #2 [29]). The FM transition shows up as a broad maximum in the ac-susceptibility χ'_{ac} and as a hump in the resistivity $\rho(T)$. The SC transition appears below 1 K as a drop to zero of the resistivity $\rho(T)$ and a large diamagnetic signal in χ'_{ac}. In polycrystalline samples the SC transition is relatively broad (ΔT_{sc} ∼0.15 K). DC-magnetization $M(T)$ measurements confirm the FM transition and the data extrapolate to a polycrystalline averaged ordered moment m_0=0.03 μ_B. FM order is further corroborated by the hysteresis loop in $M(B)$ at 2 K with a small coercive field of 0.3 mT [29].

The magnetic transition is a robust property, as the $M(T)$, χ'_{ac} and $\rho(T)$ data taken on different UCoGe batches almost coincide [29, 92]. The small ratio of m_0 to the effective moment (p_{eff} = 1.7μ_B [137]) shows UCoGe is a weak itinerant ferromagnet [7, 156]. Unlike the magnetic properties, the SC properties depend sensitively on the quality of the samples measured by the residual resistance ratio RRR. The quality of the samples was improved by annealing, as will be discussed in sec. 6.3. The sensitivity to defects, together with the absence of Pauli limiting and the presence of FM, indicates that SC in UCoGe is unconventional [29]. The anisotropy of B_{c2} gives evidence of p-wave superconductivity and points to an axial SC gap function with nodes along the direction of m_0 [39].

6.2 Thermal properties of polycrystalline UCoGe

Thermal expansion and specific heat measurements on polycrystalline samples of UCoGe presenting large anomalies at the transition temperatures brought the first evidence that FM and SC are bulk properties [29].

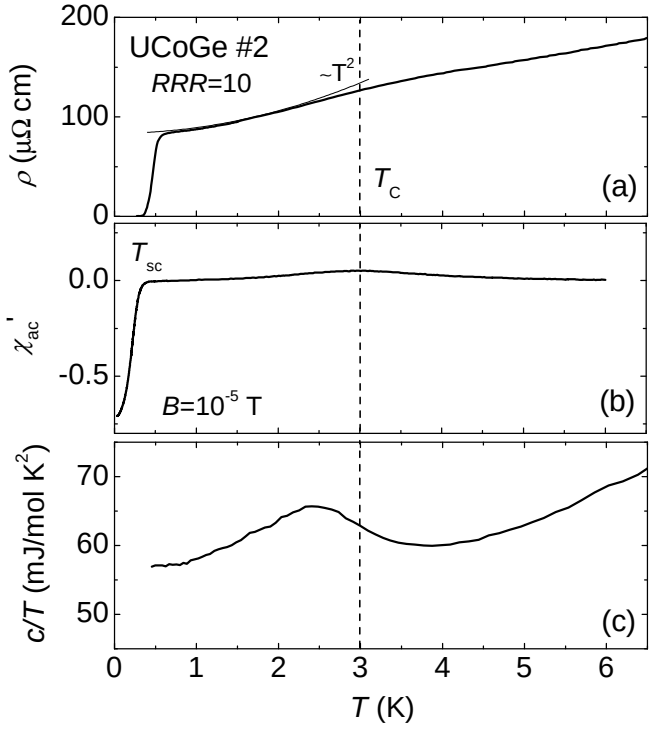

Figure 6.1: Resistivity (a), ac-susceptibility (b) and specific heat divided by temperature (c) of polycrystalline UCoGe (sample #2, RRR=10). The ac-susceptibility was measured with a small driving field of 10^{-5} T. A hump in $\rho(T)$, a maximum in $\chi'_{\rm ac}(T)$ and an anomaly in c/T locate $T_{\rm C}$ (dashed line). Superconductivity is found below $T_{\rm sc} = 0.61$ K in $\rho(T)$ and below 0.38 K in $\chi'_{\rm ac}(T)$. In the specific heat experiment the lowest temperature (0.5 K) was not low enough to detect SC. Data taken by Dr. N. T. Huy [92].

A polycrystalline sample of UCoGe was prepared with nominal composition $U_{1.02}Co_{1.02}Ge$ (sample #3). The as-cast sample was annealed for 10 days at 850 °C. Powder X-ray diffraction patterns at $T = 300$ K confirmed the TiNiSi structure reported in the literature [152, 155]. Part of the annealed sample was investigated using EPMA which revealed a matrix with a 1:1:1 composition and a small amount (2%) of impurity phases [92]. Annealing improved the quality of the sample as indicated by residual resistance ratio which increased from a couple up to $RRR \sim 30$. Afterwards, the sample was cut into a 'cube' with plane-parallel surfaces by means of spark erosion in order to be measured in the dilatometer.

The coefficient of linear thermal expansion, $\alpha(T)$, of the prepared polycrystal was measured in the temperature range 0.24 K $< T <$ 8 K in the Heliox in zero field and B=1 T, and in the temperature range 2 K $< T <$ 150 K in zero field in the bath cryostat. Specific heat data were collected using a semi-adiabatic method with a mechanical heat switch on sample #2 with a mass $m = 3$ g for T=0.5-10 K (data taken by Dr. J. C. P. Klaasse [92]). In addition specific heat measurements using a weak thermal link were carried out on sample #3 with mass $m = 0.1$ g for T=0.1-1.0 K (data taken at the University of Karlsruhe).

The data of $\alpha(T)$ versus T were taken along two directions of the square prism-shaped polycrystalline sample (dimensions $\sim 5 \times 5 \times 3$ mm^3). The data sets agreed well with each other and here we concentrate on the data in one direction only. The data are reported in fig. 6.2 in the temperature range 0.3-150 K, together with resistivity data (single crystal measurements). For comparison we plot in fig. 6.2 (upper frame) also a Debye function with Θ_D=200 K. This shows that for $T \gtrsim 80$ K $\alpha(T)$ is dominated by phonons. Below ~ 80 K an additional contribution is present. A comparison with the resistance data (fig. 6.2, lower frame) reveals that this contribution is due to the formation of a Kondo-lattice state, resulting in a coherent correlated metal state at liquid Helium temperatures.

Below 4 K the FM and SC transitions appear. The $\alpha(T)$ data in the low temperature region are shown in more detail in fig. 6.3 (FM) and in fig. 6.4 (SC) together with a comparison with the specific heat, resistivity and ac-susceptibility data. The ideal SC and FM transitions are sketched for both ordered states using an equal length change method [142] (dashed-dotted lines in the plots).

The FM transition width is large ($\Delta T_C \sim 2$ K). In the specific heat, the idealized transition has a step size $\Delta(c/T)$=0.014 J/mol K^2 at T_C=3 K. The relative change $\Delta(c/T_C)/(c/T_C)$ is only 25% and the associated magnetic entropy is small (0.3% of Rln2), as expected for a weak itinerant ferromagnet with a small

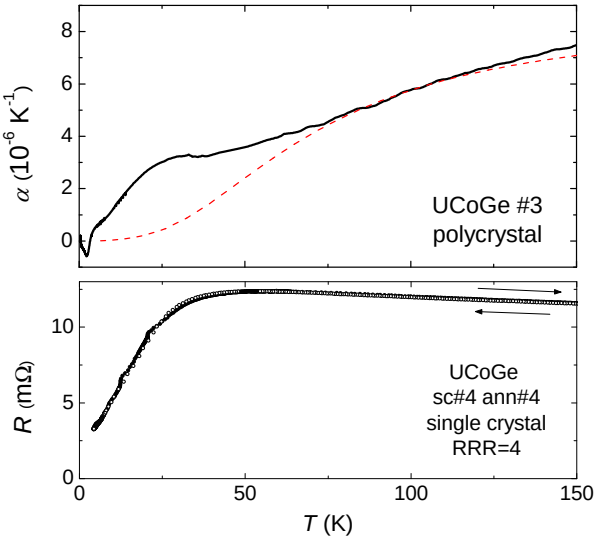

Figure 6.2: [upper frame] Coefficient of linear thermal expansion of polycrystalline UCoGe (sample#3). The dotted line represents a Debye contribution with Θ_D = 200 K. [lower frame] Resistance of single crystalline UCoGe (sc#4 ann#4) (data taken by R. Huisman).

ordered moment [156]. The Sommerfeld coefficient (γ=0.057 J/mol K^2) indicates that UCoGe is a correlated metal but the electron interaction is relatively weak. In the thermal expansion, FM order is observed as a large negative step, $\Delta\alpha$ =-1.1×10^{-6} K^{-1} at T_C=3 K with a relative change $\Delta\alpha/\alpha \approx 3.3$. This shows the magnetic transition is a bulk phenomenon. Upon application of a magnetic field B=1 T along the dilatation direction, the FM transition in α is smeared out (fig. 6.3(b)).

As reported above, the $\rho(T)$ and $\chi_{ac}(T)$ data show UCoGe becomes superconducting below 1 K. Proof of bulk SC is obtained by the specific heat and thermal expansion data (fig. 6.4). The specific heat shows a broad transition with onset temperature $T_{sc}^{onset} \sim 0.66$ K. At this temperature the resistivity has dropped to zero. A rough estimate for the step size of the idealized transition in the specific heat gives $\Delta(c/T_{sc})/\gamma \approx 1.0$ at T_{sc}. This value is smaller than the one for a conventional SC (according to the BCS theory $\Delta(c/T_{sc})/\gamma = 1.43$) but is comparable to the value found for URhGe [26]. In the thermal expansion an equivalent, broad transition is observed. Assuming an ideal transition, the step size $\Delta\alpha \approx 3.8\times10^{-7}$ K^{-1} at T_{sc}=0.45 K, i.e.

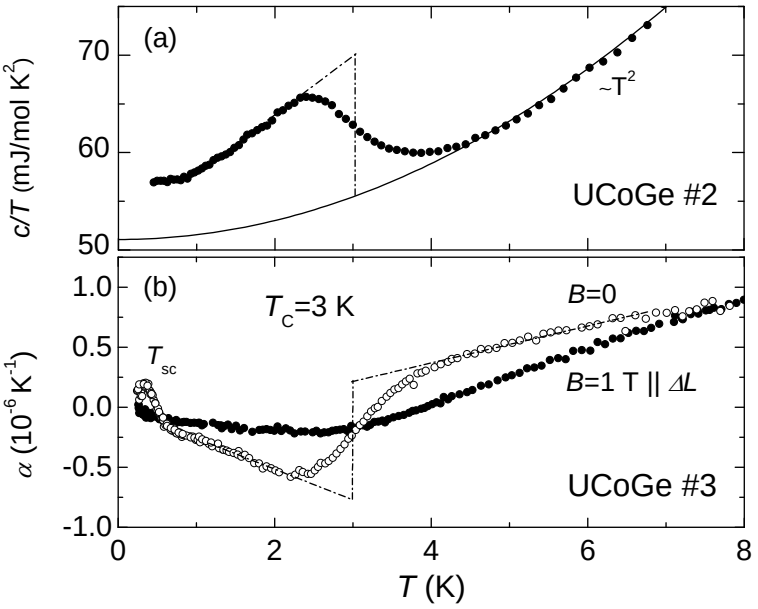

Figure 6.3: (a) Specific heat divided by temperature c/T versus temperature in zero magnetic field (ZF) for sample #2. The T^2 phonon contribution is represented by the solid line for temperature $T >5$ K. The idealized transition (dashed-dotted line) is at T_C=3 K. Bulk SC for sample #2 sets in at 0.38 K (measured by χ_{ac}, see sec. 6.1) but the $c(T)$ data extend down to 0.5 K only. Data taken by Dr. J. C. P. Klaasse [92]. (b) Coefficient of linear thermal expansion of polycrystalline UCoGe sample #3 in ZF (empty symbols). The dashed-dotted line represents the ideal transition at T_C=3 K. The peak below 0.6 K is the thermodynamic signature of the SC transition. In a field of 1 T (black dots) ($B\|\Delta L$) the FM transition broadens while superconductivity is not resolved.

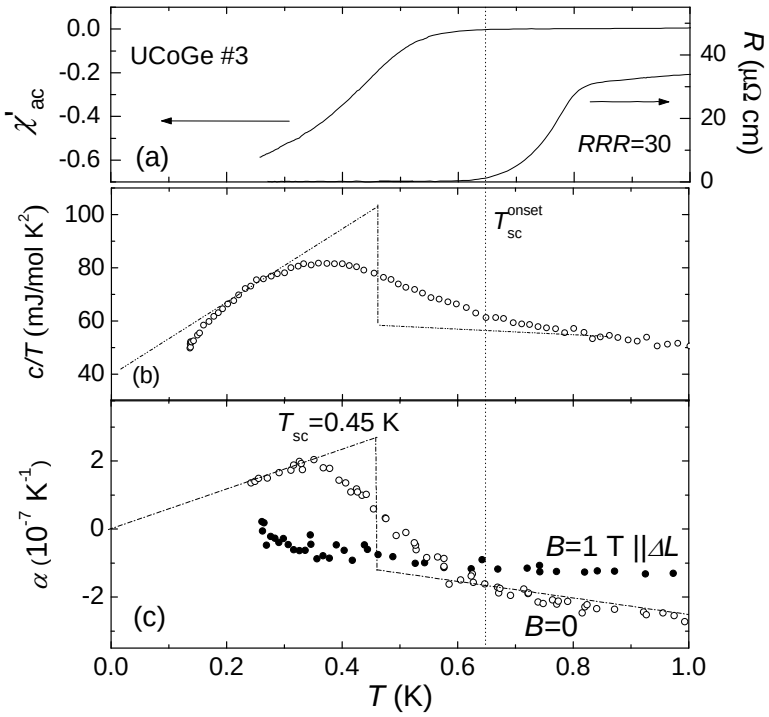

Figure 6.4: Superconducting properties of polycrystalline UCoGe sample #3. (a) ac-susceptibility $\chi_{\rm ac}(T)$ (left axis) in $B = 10^{-5}$ T and resistivity $\rho(T)$ (right axis). Data taken by Dr. N. T. Huy. (b) Specific heat divided by temperature c/T as a function of T. Bulk SC occurs below $T_{\rm sc}^{\rm onset} \sim 0.66$ K, i.e. the temperature at which the resistivity is zero (dotted vertical line). (c) Thermal expansion coefficient in zero field and in B=1 T. In zero field bulk SC is observed below $T_{\rm sc}^{\rm onset} \approx 0.66$ K. The dashed-dotted lines show the ideal transitions, located at $T_{\rm sc}$=0.45 K. In a field B=1 T applied along the dilatation direction ΔL, superconductivity is suppressed down to the lowest temperature.

a value comparable with those obtained on the heavy fermion superconductors URu_2Si_2 [157] and UPt_3 [158, 159]. In a magnetic field B=1 T the SC transition is no longer resolved.

6.2.1 Discussion

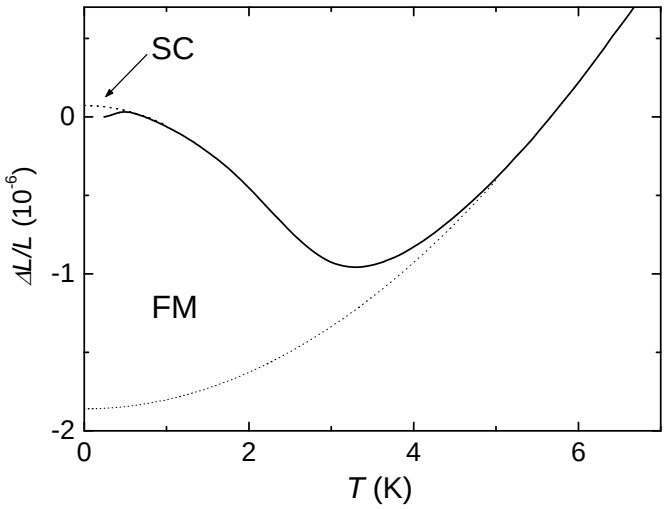

Figure 6.5: Relative length change $\Delta L/L$ as a function of temperature. The dotted lines are extrapolations based on fits of $\Delta L/L \propto T^2$ in the paramagnetic (PM) and FM states.

The relative length change $\Delta L/L = (L(T) - L(0.23\ \mathrm{K}))/L$ is calculated by integrating $\alpha(T)$ starting at the lowest measured temperature $T = 0.23$ K (fig. 6.5). The lowest dotted line in the figure, obtained by a $\propto T^2$ extrapolation from the data above T_C, indicates the $\Delta L/L$ in the absence of a FM state, while the upper dotted line, obtained by quadratic extrapolation of α_{FM} to $T = 0$, indicates $\Delta L/L$ in the absence of a SC state. The total length change associated with SC after correcting for the normal state linear contribution ($\Delta L/L \sim -0.1 \times 10^{-6}$) is small compared to the length change $\Delta L/L \sim 1.9 \times 10^{-6}$ due to magnetic ordering. This allows us to draw the important conclusion that magnetism is not expelled below T_{sc} and that FM coexists with SC.

The pressure variation of T_C and T_{sc} of UCoGe can be estimated using the

Ehrenfest relation for second-order phase transitions:

$$\frac{dT_{\mathrm{C,sc}}}{dp} = V_{\mathrm{m}} T_{\mathrm{C,sc}} \frac{\Delta\beta_{\mathrm{C,sc}}}{\Delta c_{\mathrm{C,sc}}} \tag{6.1}$$

where $V_{\mathrm{m}} = 3.13 \times 10^{-5}$ m^3/mol, and $\Delta\beta_{\mathrm{C,sc}} = 3\Delta\alpha_{\mathrm{C,sc}}$ and $\Delta c_{\mathrm{C,sc}}$ are the step sizes of $\alpha(T)$ and $c(T)$ at the FM and SC transition, respectively. From the estimated step sizes of $\alpha(T)$ and $c(T)$ we calculate

$$dT_{\mathrm{C}}/dp = -0.79 \text{ K/kbar}$$

$$dT_{\mathrm{sc}}/dp \sim 0.062 \text{ K/kbar}.$$

The calculated value of dT_{C}/dp shows that the critical pressure at which magnetism is predicted to vanish is very low, p_{c} ∼4 kbar, considering a linear depression of T_{C} with pressure. Interestingly T_{sc} increases with pressure. This places UCoGe in the generic phase diagram of fig. 2.4 (left panel) on the far side of the left SC lobe with respect to the critical point. Upon applying pressure, the SC transition temperature of UCoGe is predicted to pass through a maximum before vanishing at the magnetic QCP. Later studies on polycrystals [41] and single crystals [42] under pressure showed a phase diagram different from ref. [30], with, however, a $T_{\mathrm{C,sc}}$ pressure dependence with the same sign as predicted using the Ehrenfest relations.

The final and decisive proof that FM and SC in UCoGe are bulk properties and coexist at the microscopic scale is obtained by μSR [92, 160] and NQR [161] experiments. Notably, zero field (ZF) muon spin rotation data provide unambiguous proof that FM is present in the whole sample volume. Furthermore, the persistence of the spontaneous muon precession signal with the same amplitude below T_{sc} provides solid evidence for the coexistence of FM and SC [92, 160].

6.3 Characterization of UCoGe single crystals

The SC transition temperature of UCoGe is strongly defect sensitive [29]. This sensitivity is due to pair-breaking occurring not only for magnetic impurities, as in conventional SC, but also for non-magnetic impurities and defects. Together with the proximity to a ferromagnetic instability and the absence of Pauli limiting, the non-magnetic defect sensitivity yields evidence of unconventional superconductivity. Examples of the sensitivity of T_{sc} to the residual resistivity are already reported in the literature, for instance in the case of the ferromagnetic superconductor URhGe [26, 162] and the p-wave superconductor Sr_2RuO_4 [163, 164]. It is therefore crucial to utilize high-quality samples

to investigate the special properties of UCoGe. The first high-quality single crystal of UCoGe was prepared by Dr. Y. K. Huang at the WZI [165]. This allowed to determine the anisotropy in the magnetization: UCoGe is a uniaxial FM with the ordered moment m_0 pointing along the orthorhombic c-axis. The crystal was subsequently used for a study of the anisotropy of the upper critical field B_{c2} providing evidence that the SC gap function is unconventional and has point nodes along the direction of m_0 [39]. In the course of this thesis work, several other single crystalline samples of UCoGe have been prepared with the main aim to obtain a large single crystal (typically $5 \times 5 \times 5$ mm^3) for thermal expansion measurements. Especially, much work was devoted to investigate the effect of different annealing procedures on the SC and FM properties.

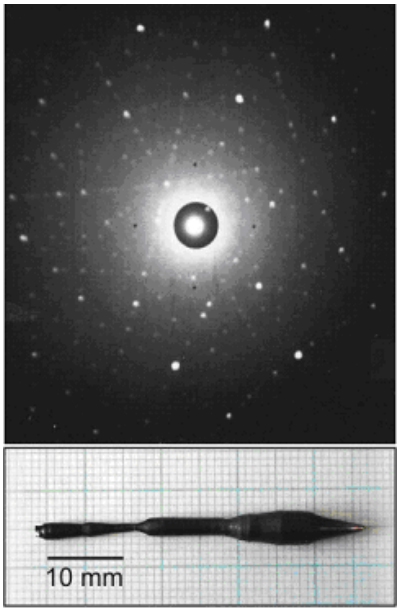

Figure 6.6: X-ray Laue picture (top) of as-grown single crystalline UCoGe (bottom). Picture taken from ref. [92].

Polycrystalline samples were prepared as starting material by arc melting following the procedure outlined in chap. 3. These sample were prepared from high purity constituents (natural or depleted U 3N, Co 3N and Ge 5N) with nominal composition $U_{1.01}Co_{1.02}Ge$. The small excess of U is to compensate for the loss due to oxidation during the sample preparation process, while excess Co was used to prevent the formation of the secondary phases revealed by EPMA. Subsequently, single crystalline samples were grown by Dr. Y. K.

Name	Annealing procedure	*RRR*	FM	SC	Remarks
sc#1	as-cast	1.2-5	not clear or broad FM transition	T_{sc}=0.25 K ΔT_{sc}=0.15 K	modified Czochralski technique
sc#1 - ann#1[a]	1 day @1250 °C + 3 weeks @880 °C	**30** (*a*) **40** (*b*)	very sharp FM transition	T_{sc}=0.55 K ΔT_{sc}=0.1 K	annealing of 3 bars
sc#1 - ann#2	60 hours @900 °C	7.6	broad FM transition	T_{sc}=0.35 K ΔT_{sc}=0.15 K	annealing of 3 polished bars
sc#2	as-cast	5	very broad FM transition	T_{sc}=0.25 K ΔT_{sc}=0.20 K	modified Czochralski technique
sc#2 - ann#1	1 day @1250 °C + 3 weeks @880 °C	1.2-4.6	not clear FM	T_{sc}=0.30 K - not complete transition	annealing of 2 bulk pieces
sc#2 - ann#2	1 day @1250 °C + 3 weeks @880 °C	NA	NA	NA	annealing of polished bars and a slice, samples destroyed
sc#4	as-cast	1.6	T_{C1} = 3 K T_{C2} = 1.5 K (double transition)	not complete $\Delta T_{sc} < 0.4$ K	modified Czochralski technique
sc#4 - ann#1	1 day @1250 °C + 3 weeks @880 °C	8 (bar *c* axis) 8 (bulk *c* axis) 3.5 (bulk *b* axis)	T_C = 2.5 K (*c*) 1.7 K (*b*)	T_{sc} = 0.64 K (*c*) 0.58 K (*b*) ΔT_{sc}=0.28 K (*c*) 0.17 K (*b*)	annealing of polished bars and bulk pieces
sc#4 - ann#2	1 week @950 °C	12 (*c* axis) 5.5 (*b* axis)	T_C = 1.5 K (*c*,*b*)	T_{sc}=0.45 K (*c*) 0.53 K (*b*) ΔT_{sc}=0.20 K	annealing of polished bars
sc#4 - ann#3	3 weeks @950 °C	9 (*c* axis) 3.3 (*b* axis)	T_C = 2.3 − 1.5 (*c*, double transition) T_C = 1.3 K (*b*)	T_{sc}=0.52 K (*c*) 0.40 K (*b*) ΔT_{sc}=0.22 K (*c*) 0.40 K (*b*)	annealing of polished bars

Table 6.1: Summary of the main features of the annealed single crystalline sample of UCoGe before and after different annealing procedures.

[a]Annealing procedures carried out by Dr. N. T. Huy

Huang using the Czochralski technique. The single crystallinity was checked by Laue back-scattering (see for an example fig. 6.6). The same technique was used to orient the crystals. The single crystalline samples were cut by spark erosion and the surfaces of several pieces were polished before being annealed.

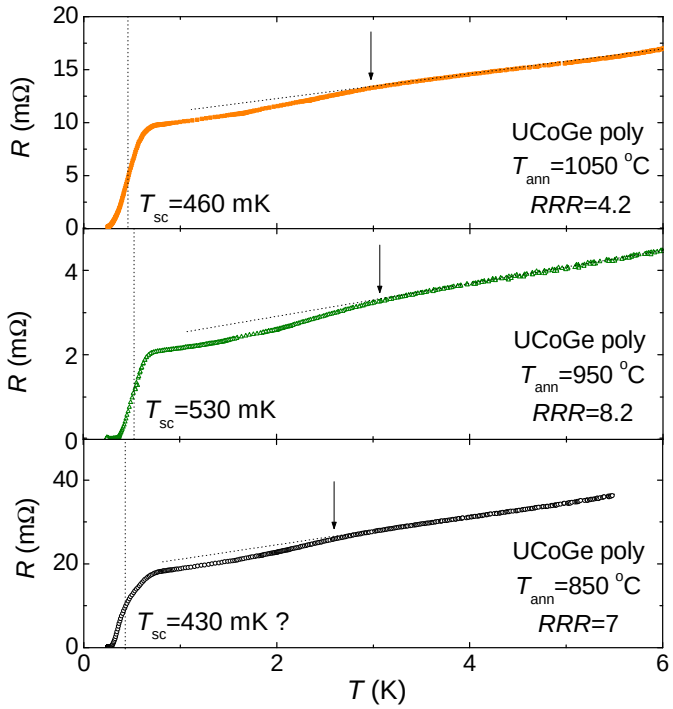

Figure 6.7: Resistivity of polycrystalline UCoGe samples taken from the same batch. The samples were heat-treated for 10 days at 1050 °C (upper frame), 950 °C (middle frame) and 850 °C (lower frame). Note the different vertical scales. The arrows mark the ferromagnetic transition at T_C while the vertical dotted lines mark the superconducting transition at T_{sc}. The dotted lines represent a linear extrapolation of the resistance in the PM region to below T_C. The data were taken by E. Slooten.

Different annealing procedures were used for different pieces of the single crystals, labelled sc#1, sc#2 and sc#4, as reported in tab. 6.1. The first heat treatment procedures carried out [165] were copied from the one applied to URhGe [162, 166, 167]. Here, a one day anneal at 1250 °C was aimed at releasing eventual excess Ge, as Ge has a much larger vapour pressure at this temperature than the other two elements. The subsequent three-week anneal

is meant to homogenize the material. In addition we performed several annealing procedures without the one day anneal at 1250 °C. The last two annealing procedures were carried out for three weeks at 950 °C. This temperature was chosen because it gave the best results on a test on polycrystalline samples. These polycrystalline pieces taken from the same batch were annealed for 10 days at 850 °C, 950 °C and 1050 °C respectively. Their resistance was measured (fig. 6.7). The highest value of the residual resistance ratio, RRR=8.5, is reported for the piece annealed at 950 °C. Moreover this sample presents the highest superconducting transition temperature T_{sc} = 530 mK with a broad (ΔT_{sc} = 350 mK) but complete transition. The transition temperature is in agreement with previous measurements on polycrystalline samples with similar RRR [92] although the width of the transition is double the size. The ferromagnetic transition is observed at T_C = 3 K with a clear hump.

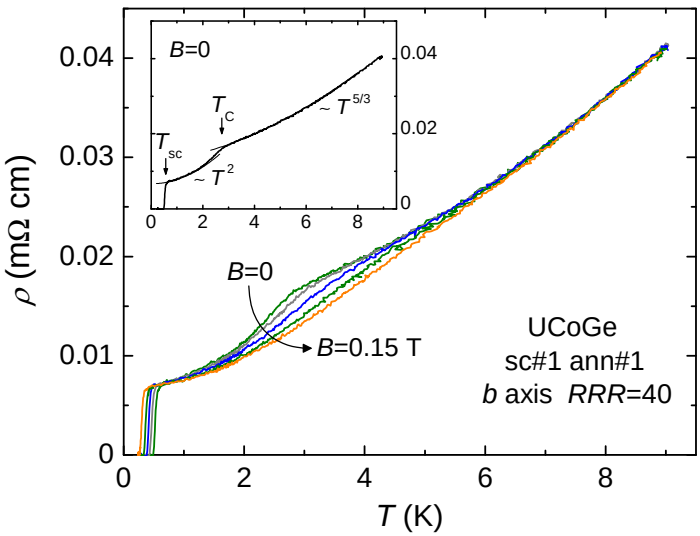

Figure 6.8: Resistivity of UCoGe sc#1b ann#1, with $I \| b$ and $B \| c$. The applied magnetic fields are B=0, 0.02, 0.05, 0.1, and 0.15 T. Inset: Resistivity of UCoGe sc#1b ann#1 in zero applied field. The FM and SC transition temperatures are marked as T_C and T_{sc} respectively. The solid lines are fits to the data in the PM ($\sim T^{5/3}$) and in the FM ($\sim T^2$) region. The residual resistivity is $\rho_0 \sim 7$ $\mu\Omega$ cm and $RRR = 40$.

As representatives of the results reported in tab. 6.1, we show two extreme cases. An example of a successful annealing [165] is reported in fig. 6.8 for a sample with RRR=40. In sc#1 ann#1 ($I \| b$, later on called sc#1b ann#1),

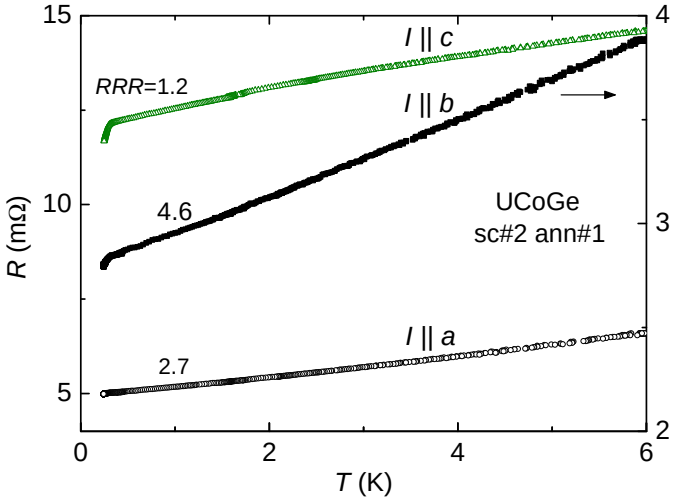

Figure 6.9: Resistance of UCoGe sc#2 ann#1 for a current along the three crystallographic axes, as indicated. Note the different vertical scale for the data with $I \| b$.

both the FM and the SC transitions are clearly present at $T_C = 2.8$ K and $T_{sc} \sim 0.5$ K. The transitions are subsequently depressed in a small magnetic field $B \| c$ (in agreement with the data reported in ref. [39] on sc#1 ann#1 with $I \| a$, subsequently referred as sc#1a ann#1). An example of a non satisfactory annealing is reported in fig. 6.9, where we show the resistance of UCoGe sc#2 ann#1 cut along the three crystallographic axes. The residual resistance ratio is different for every sample and almost no improvement of the RRR compared to the as-cast crystal is found. Signatures of the FM and SC transitions are present, but none of them is sharp or complete.

For the two examples reported here, the annealing procedures were the same, but for sc#2 a new furnace was used. The unsatisfactory result suggested that an oven calibration was necessary to reproduce the result obtained on UCoGe sc#1 ann#1. We therefore proceeded with a temperature calibration of the furnaces. The annealing procedures on UCoGe sc#4 (see tab. 6.1) and sc#5 (data not reported) subsequently showed some improvement of the RRR with a best $RRR = 12$, but we still are not able to reproduce the results for sc#1 ann#1.

The results of the different annealing procedures are summarized in fig. 6.10

by plotting the residual resistance ratio RRR (as an estimate of the purity of the sample) as a function of the annealing temperature. From the plot it is evident that the annealing procedure improves the quality of the sample. Unfortunately the best RRR=12 for sc#4 ann#2 is considerably smaller than the values obtained for UCoGe sc#1 ann#1. For this crystal the residual resistance ratio RRR=30-40 (see inset in fig. 6.10).

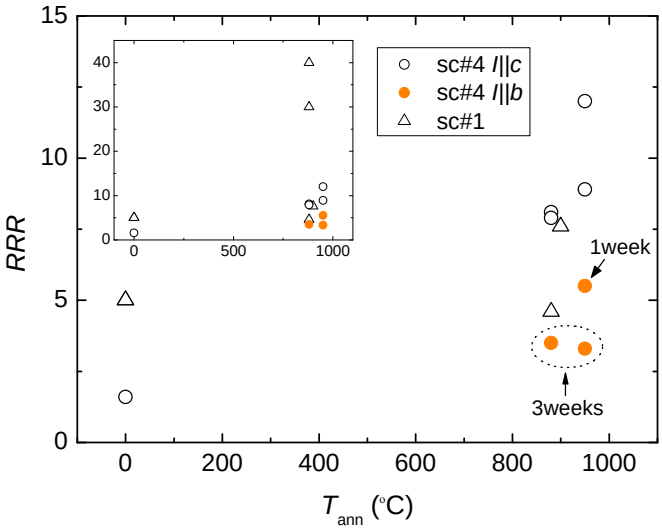

Figure 6.10: Residual resistance ratio RRR of several single crystalline samples of UCoGe as a function of the annealing temperature T_{ann}. Inset: same plot in a wider vertical scale.

In fig. 6.11 we trace the superconducting transition temperature for different crystals as a function of the residual resistance ratio. The plot represents the influence of non-magnetic impurities (represented by the RRR) on superconductivity. The effect of non-magnetic impurities is theoretically described in ref. [168], following the theory proposed by Abrikosov and Gor'kov for magnetic impurities on conventional superconductors [169, 170]. It was shown that T_{sc} is inversely proportional to ρ_0 [171], as sketched in the plot (since $RRR \sim 1/\rho_0$). Furthermore, it is clear from the plot that improving the quality of the sample will not increase T_{sc} further than ∼0.6 K. Nevertheless the width of the transition (given by the error bar) does become smaller for higher RRR.

Finally, we notice that EPMA data taken on sc#1c ann#1 (RRR=30),

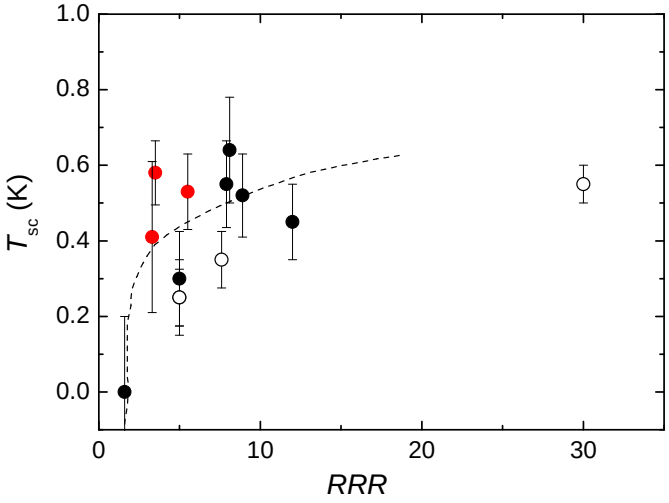

Figure 6.11: Superconduction transition temperature of several single crystalline UCoGe samples as a function of the residual resistance ratio. The line is a guide to the eye for the relation between T_{sc} and RRR.

sc#2 as-cast (RRR=5) and sc#2 ann#1 (RRR=4.6) detected no differences in composition within the instrumental resolution (1%). For all the three samples the EPMA results revealed a homogeneous matrix with composition 1:1:1 and no secondary phases.

6.3.1 Resistivity at high magnetic field

The superconducting ferromagnet URhGe shows an unusual re-entrant superconducting phase for a magnetic field applied along the b axis [133]. Since the magnetic and superconducting properties of URhGe and UCoGe presents similarities, it is of interest to search for a similar field re-entrant SC state in UCoGe. To this purpose, high magnetic field experiments were carried out in a dilution refrigerator at the HFML in Nijmegen. The resistance of UCoGe sc#1a ann#1 (bar cut along the a axis, $RRR = 30$) was measured at several fixed low temperatures and in large magnetic fields up to 30 T.

The results are reported in figs. 6.12 and 6.13. For $B \| I \| a$, field sweeps up to 30 T and back to zero field were made at T=60, 180 and 300 mK. For $I \| a$ and $B \| b$, sweeps were made at T=110, 200 and 300 mK. No sign of re-entrant superconductivity is observed up to 30 T. Very recently, however, Aoki and

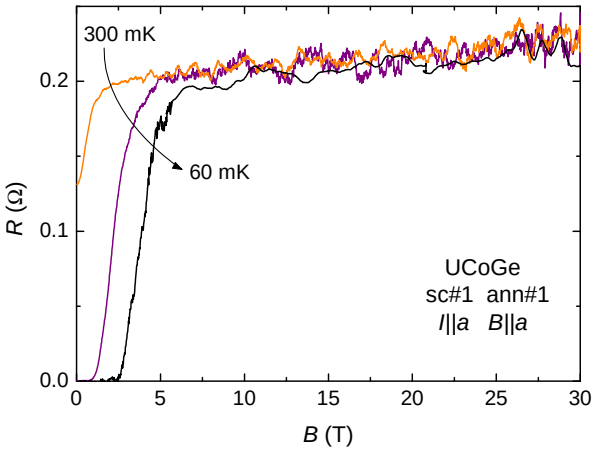

Figure 6.12: Resistance of UCoGe sc#1a ann#1 as a function of the magnetic field B, with $B \| I \| a$. The field sweeps are made at 60 mK, 180 mK, and 300 mK.

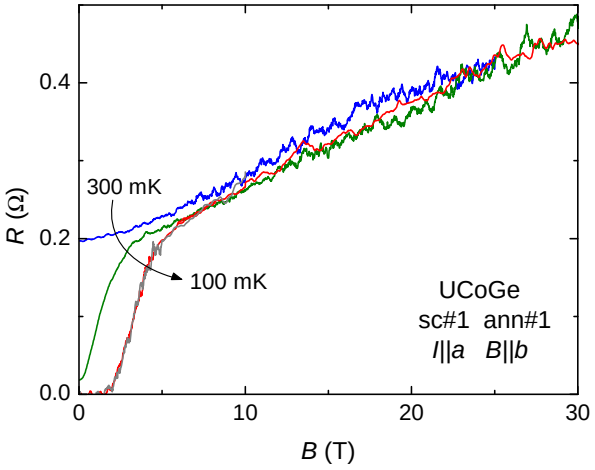

Figure 6.13: Resistance of UCoGe sc#1a ann#1 as a function of the magnetic field B, with $I \| a$ and $B \| b$. The field sweeps are made at 110 mK, 200 mK, and 300 mK.

collaborators performed a careful study of the angular dependence of B_{c2} on a high quality sample ($RRR = 30$) of UCoGe [172]. They obtained a remarkable result. For $B \| b$, B_{c2} shows an unusual S-shape, implying field-reinforced SC in the field range 12-14 T. A small mis-orientation of a few degrees largely washes out this phenomenon. Although the sample we used for the experiment in Nijmegen was carefully oriented within 1-2 degrees, possibly an additional orientation error in mounting the sample in the dilution refrigerator hampered the observation of the field-reinforced superconductivity.

6.4 Thermal properties of single crystalline UCoGe in zero field

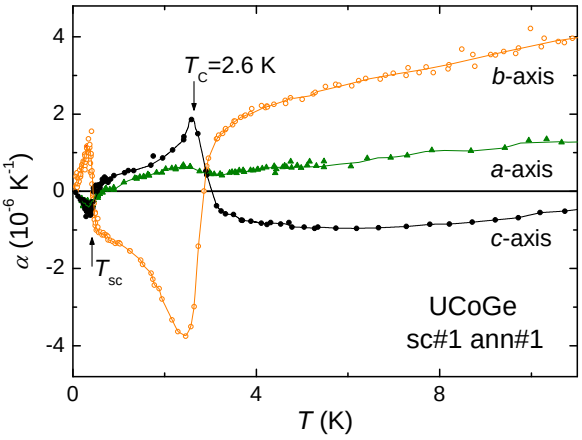

Figure 6.14: Coefficient of linear thermal expansion of UCoGe sc#1 ann#1 along the a, b and c crystallographic axes, as indicated. The arrows indicate T_C and T_{sc}, as extracted from $\beta(T)$ (see text).

In this section we present thermal expansion measurements on UCoGe single crystals in zero field. Ideally, for the dilatometer, samples with a typical size of $\sim 5 \times 5 \times 5$ mm^3 are required. However, even after preparing several single crystals and applying different heat treatments (see previous section 6.3), large crystal with acceptable RRR values were not yet available. We therefore decided to measure the coefficient of linear thermal expansion on two bar shaped samples with dimensions $\sim 1 \times 1 \times 4$ mm^3 that we previously used for transport measurements. These samples are labelled UCoGe sc#1a ann#1

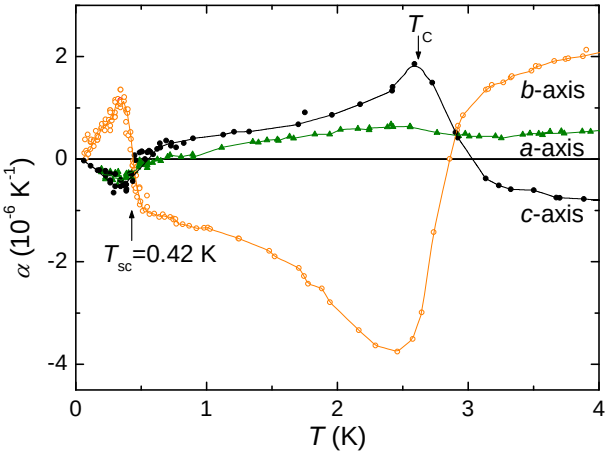

Figure 6.15: Coefficient of linear thermal expansion of UCoGe sc#1 ann#1 at low temperatures along the a, b and c crystallographic axes, as indicated. The arrows indicate T_C and T_{sc}, as extracted from $\beta(T)$ (see text).

and sc#1b ann#1, where the character stands for crystallographic axis along the long direction of the bar. These samples are of high quality as evidenced by the RRR values of 30 and 40 respectively. On the b axis sample α_a was measured, while on the a axis sample α_b and α_c were measured. In this way the data were taken on small samples with a typical thickness of ~ 1 mm. No further heat treatment, spark erosion or polishing process was made on the samples after the transport measurements were carried out.

The thermal expansion data were taken in the Heliox system (0.23 K $< T <$ 14 K) and in the Kelvinox system (0.06 K $< T <$ 1 K). The measurements taken in different cryostats are in good agreement with each other. The data in zero field are plotted in figs. 6.14 (up to 11 K) and 6.15 (up to 4 K). They reveal a strong anisotropy. In the paramagnetic phase α_a and α_b are positive, while α_c is negative. The most pronounced variation is observed along the b axis. For this direction, FM yields a negative and SC a positive contribution to α. For the a and c axis the contributions are smaller and the polarity is reversed. At the FM and SC phase transitions, large step-like changes, $\Delta\alpha$, are found. The large values of $\Delta\alpha$ at T_C and T_{sc} provide solid evidence that FM and SC are bulk properties. Notice, the step-sizes at T_{sc} are comparable to the ones obtained for the heavy-fermion SCs URu_2Si_2 [157] and UPt_3 [159]. For $T < T_{sc}$, α_i drops to zero for all the axes. The scatter of the

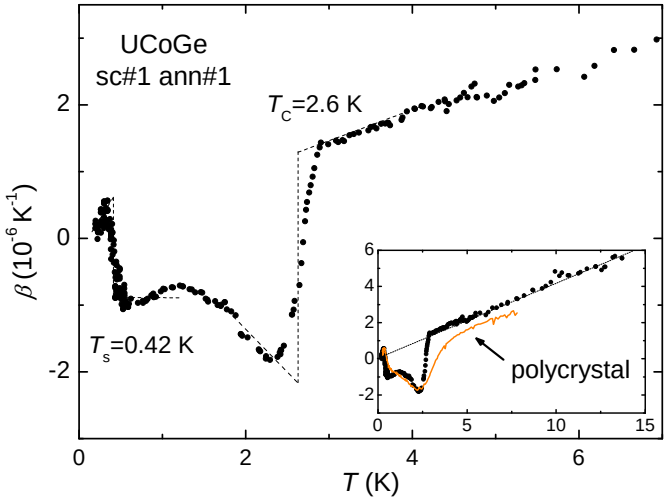

Figure 6.16: Coefficient of volume thermal expansion of single crystalline UCoGe sc#1 ann#1 as a function of temperature. The dashed lines represent idealized sharp FM and SC transitions, at $T_C = 2.6$ K and $T_{sc} = 0.42$ K, respectively. The star marks an additional contribution before the SC transition. Inset: Comparison of $\beta(T)$ of single-crystalline (closed circles) and polycrystalline (solid line) UCoGe. The dashed line gives $\beta_{para}(T) = aT$ (see text).

data prevents a proper determination of the power law function of $\alpha(T) \propto T^n$ for $T \to 0$. Such a power law behaviour is expected for an unconventional superconductor ($\sim T^2$ is expected for line nodes in the gap function and $\sim T^3$ for point nodes [173]). Nevertheless, we can observe that the temperature dependence is stronger than exponential (expected for an isotropically gapped BSC superconductor [174]).

The overall behaviour of UCoGe is determined by the coefficient of volume thermal expansion $\beta(T) = \sum_i \alpha_i$ where $i = a, b, c$. Ideally the $\alpha_i(T)$ curves should be measured on one single sample, however, in our case we used two samples with slightly different RRR-values. The resulting $\beta(T)$ is presented in fig. 6.16. The data show a large negative step at T_C and a positive step at T_{sc}. Since the phase transitions are relatively broad in temperature, we use an equal volume construction [142] to obtain idealized sharp transitions. In this way we extract $T_C^{bulk} = 2.6$ K and $T_{sc}^{bulk} = 0.42$ K. In the inset to fig. 6.16 we compare $\beta(T)$ of the single crystal with previous results on a polycrystal [29],

where we assume $\beta = 3\alpha$. The data show a nice overall agreement, but, obviously, the phase transitions are much sharper for the single crystal.

A closer inspection of the volume thermal expansion reveals an additional contribution is present below ~ 1.5 K in the FM phase, just before superconductivity sets in (star symbol in fig. 6.16). This shoulder-like feature indicates the presence of a second energy scale. A similar feature was reported for other SCFMs. It was observed in the specific heat of a polycrystalline sample of URhGe [38], in specific heat [140] and thermal expansion [134] of single crystalline samples of URhGe. At ambient pressure it was observed in specific heat [25] and thermal expansion [175] of UGe_2 and in thermal expansion of UIr [135]. This feature could possibly be related to an enhancement of the spin fluctuations. It will be highly interesting to investigate whether these enhanced spin fluctuations actually provide the pairing interaction for superconductivity.

Specific heat, $c(T)$, data around the SC transition are reported in fig. 6.17(b). The phase transition for sc#1*b* ann#1 is broad, with $\Delta T_{\rm sc} \sim 0.2$ K. An estimate for the step-size $\Delta(c/T_{\rm sc})$ can be deduced using an equal entropy method (dashed line in fig. 6.17(b)), which yields an idealized transition at $T_{\rm sc} = 0.35$ K and $\Delta(c/T_{\rm sc})/\gamma_{\rm N} \approx 0.7$, where $\gamma_{\rm N} = 0.062$ J/mol K^2 is the Sommerfeld coefficient. This value is considerably smaller than the BCS value 1.43 for a conventional SC. On the other hand, a smooth extrapolation of c/T versus T to 0 K indicates the presence of a residual term $\gamma_0 = 0.04$ J/mol K^2. Since orthorhombic SCFMs are in principle two-band SCs [78], with equal spin-pairing triplet states $|\uparrow\uparrow\rangle$ and $|\downarrow\downarrow\rangle$ in the spin-up and spin-down bands, respectively, a finite γ_0-value could be taken as evidence that only one band superconducts [176], in which case $\gamma_0 = \gamma_{\rm N}/2$. However, in our case the broad transition and finite γ_0-value strongly suggest sample quality is an issue. The low value $\Delta(c/T_{\rm sc})/\gamma_{\rm N}$ and finite γ_0 term remind one of the early specific-heat data on single crystals of the heavy-fermion SC UPt_3 [177]. Upon improving the sample quality the transition became more and more sharp, and eventually a split transition appeared, as well as a much reduced γ_0 value [178].

In fig. 6.17 we compare $c/T(T)$ (b) with resistivity, $\rho(T)$ (c), data taken on the same sample sc#1*b* ann#1, and $\alpha_b(T)$ (a) measured on sc#1*a* ann#1. The zero resistance state is reached at 0.5 K, which corresponds to the onset temperature $T_{\rm sc}^{\rm onset}$ for bulk SC. Using idealized constructions for the SC phase transition in c/T (fig. 6.17(b)) and α_b (fig. 6.17(a)) we obtain $T_{\rm sc}^{\rm bulk}$ is 0.35 K and 0.42 K, for sc#1*b* ann#1 and sc#1*a* ann#1 respectively.

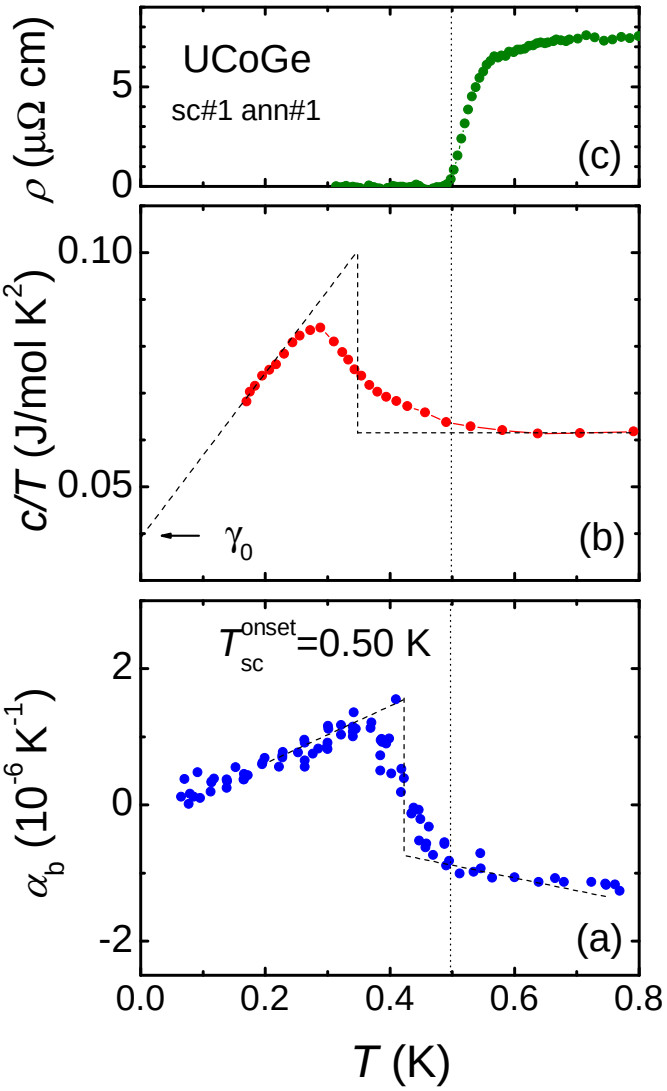

Figure 6.17: (a) $\alpha_b(T)$ of UCoGe (sc#1a ann#1). (b) Specific heat of UCoGe (sc#1b ann#1) in a plot of c/T versus T. (c) Resistivity versus T of UCoGe (sc#1a ann#1). The vertical dotted line indicates the onset temperature of bulk SC. The dashed lines in (a) and (b) represent idealized sharp FM and SC transitions. The specific heat data are taken by J. Hartbaum (University of Karlsruhe).

6.4.1 Discussion

In the inset of fig. 6.16, $\beta(T)$ up to 15 K is shown. Surprisingly $\beta(T)$ shows a linear behaviour for 5 K $< T <$ 15 K with $\beta_{\mathrm{PM}}(T) = (4.4 \pm 1.0) \times 10^{-7}\, T$. This shows that the phonon contribution to the thermal expansion is small compared to the linear electronic contribution for $T <$ 15 K. Using the coefficient $\tilde{\beta} = 0.54 \times 10^{-3}$ J/mol K^4 [29, 92] of the T^3 phonon contribution in the specific heat of the polycrystalline sample (see fig. 6.3) we can estimate the corresponding b value in the thermal expansion under the assumption $\Gamma_{\mathrm{ph}} = 2$. We obtain

$$b = \frac{\kappa_{\mathrm{T}}}{V_{\mathrm{m}}} \Gamma \tilde{\beta} = 0.3 \times 10^{-9} K^{-4}$$

where $V_{\mathrm{m}} = 3.13 \times 10^{-5}$ m^3/mol and $\kappa_{\mathrm{T}} \sim 1$ Mbar^{-1} is an estimate of the compressibility. This value of b indicates that for $T <$ 15 K the phonon contribution is indeed small compared to the electronic contribution.

As was done previously with the polycrystalline sample of UCoGe, we calculate here the relative volume change $\Delta V/V = (V(T) - V(0.05\ \mathrm{K}))/V$ of the sample as a function of the temperature. This is calculated by integrating $\beta(T)$ from the lowest temperature. The result (in fig. 6.18) is in good agreement with that from the polycrystalline sample, where however the effect was much broader because of the polycrystalline nature of the sample. The relative volume change due to the spontaneous magnetostriction amounts to $\Delta V/V = 4.2 \times 10^{-6}$ for $T \to 0$ and is much larger (and has an opposite sign) than the estimated $\Delta V/V = -2.5 \times 10^{-7}$ due to SC (see inset fig. 6.18). The latter value is due to the condensation energy of the SC state and agrees well with similar values obtained for heavy-fermion superconductors [157, 159]. Thus FM order is not expelled below T_{sc} and coexists with superconductivity.

With the thermal expansion and specific heat data on single crystals, one may extract the uniaxial pressure variation of T_{sc} and T_{C} with help of the Ehrenfest relation for second-order phase transitions

$$\frac{dT}{dp_i} = \frac{V_{\mathrm{m}} \Delta\alpha_i}{\Delta(c/T)}$$

where the index i refers to the orthorhombic a, b or c axis, $\Delta\alpha_i$ is the thermal expansion step along a certain axis i and V_{m} is the molar volume. The values of $\Delta\alpha_i$ are reported in table 6.2, for both the FM and the SC transition. The values of $\Delta\beta$ for the FM and SC transition are derived from $\beta(T)$ and listed in the same table. Since the specific heat for a single crystalline sample for $T >$ 1 K has not been measured yet, $\Delta(c/T_{\mathrm{C}}) = 14$ mJ/mol K^{-2} from the polycrystalline sample was used [29]. $\Delta(c/T_{\mathrm{sc}}) = 38$ mJ/mol K^{-2} of UCoGe sc#1b ann#1 as reported in fig. 6.17 is used. Since not all steps

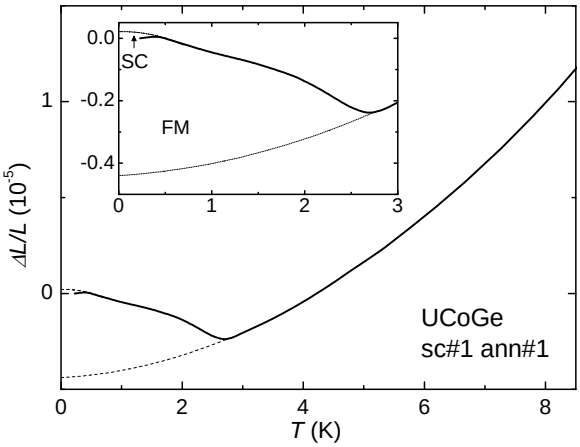

Figure 6.18: The relative volume change $\Delta V/V = (V(T) - V(0.05\text{K}))/V$ as a function of T (solid line). The black dashed line gives $\Delta V/V$ in the absence of FM order. The gray dashed line gives a smooth extrapolation of $\Delta V/V$ in the absence of SC. Inset: Blow-up of the low-T part.

$\Delta\alpha_i$ and $\Delta(c/T_{s,C})$ have been measured on the same sample, we here restrict ourselves to a qualitative analysis. The largest effect is calculated for p_b, uniaxial pressure along the b axis: T_{sc} increases and T_{C} decreases. For p_a and p_c the effect is smaller with reversed polarity. An estimate of the variation of T_{sc} as a function of hydrostatic pressure can be calculated using the relation: $dT_{\text{sc}}/dp = V_{\text{m}}\Delta\beta/\Delta(c/T_{\text{sc}})$. By combining the results obtained on the two crystals, using the values $\Delta\beta = 1.19 \times 10^{-6}$ K^{-1} (see fig. 6.14) and $\Delta c/T_{\text{sc}} = 0.038$ J/molK^2 (fig. 6.15), we calculate $dT_{\text{sc}}/dp = 0.098$ K/kbar. This value is larger than the value deduced for a polycrystal 0.062 K/kbar [29, 179] reported in sec. 6.2. In the same way we calculate $dT_{\text{C}}/dp = -0.79$ K/kbar, where we used $\Delta\beta = -3.53 \times 10^{-6}$ K^{-1} (fig. 6.14) and the polycrystal value $\Delta c/T_{\text{C}}$ reported above. Notice the pressure variations deduced for the single crystal by the Ehrenfest relation are considerably larger than the experimental values $dT_{\text{sc}}/dp = 0.03$ K/kbar and $dT_{\text{C}}/dp \sim -0.21$ K/kbar [41, 42], which tells us the quantitative analysis should be interpreted with care.

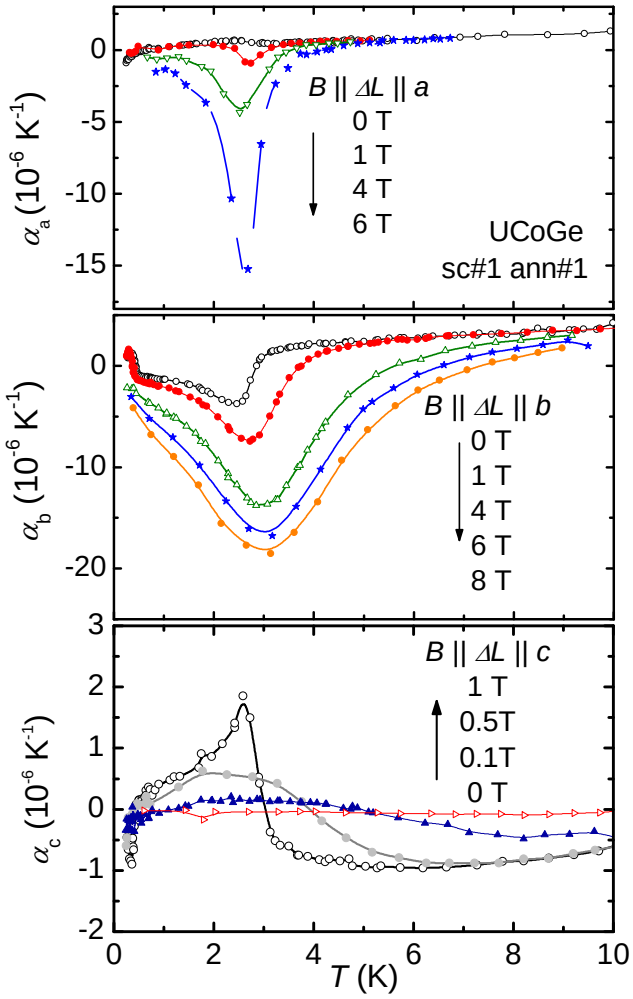

Figure 6.19: Coefficient of linear thermal expansion of UCoGe sc#1 ann#1 in applied magnetic field, for $B\|a$ (upper panel), $B\|b$ (middle panel) and $B\|c$ (lower panel). The magnetic field is applied along the elongation direction $B\|\Delta L$.

FM	$\Delta\alpha$ (10^{-6}K^{-1})	dT/dp (K/kbar)
a	0.4	0.1
b	-6.7	-1.5
c	2.8	0.6
volume	-3.5	-0.8

SC	$\Delta\alpha$ (10^{-6}K^{-1})	dT/dp (K/kbar)
a	-0.4	-0.03
b	2.4	0.17
c	-0.8	-0.06
volume	1.2	0.08

Table 6.2: Pressure dependencies of $T_{\rm C}$ and $T_{\rm sc}$ in UCoGe. The values are determined using the Ehrenfest relation with $\Delta\alpha_i$ from UCoGe sc#1 ann#1. $\Delta(c/T)_{\rm FM} = 14$ mJ/mol K^{-2} is determined from the polycrystalline sample #3 while $\Delta(c/T)_{\rm SC} = 38$ mJ/mol K^{-2} from the single crystalline sample sc#1b ann#1.

6.5 Thermal expansion of single crystalline UCoGe in field

The thermal expansion of single crystalline UCoGe was measured in magnetic field, in order to study the field dependence of FM and SC. We report measurements of $\alpha_i(T)$ along each orthorhombic axis in field applied parallel to the elongation direction $B\|\Delta L\|i$, with $i = a, b, c$. Notice that, in the following and if not otherwise stated, $\Delta\alpha_i$ refers to the step height of the FM transition. The data are shown in fig. 6.19 in the temperature range 0.23 K $< T <$ 10 K. The coefficient of linear thermal expansion of UCoGe behaves in a peculiar and irregular way in field. Again we observe a large anisotropy, as in the zero field data. In α_c ($B\|m_0$) the FM transition is peaked in zero field (fig. 6.19, lower panel). The effect of the magnetic field, as expected, is to smear out the transition rapidly: in a field of 1 T $\alpha_c(T)$ is virtually temperature independent up to 10 K and close to zero. The same behaviour is observed for the SC transition, where $T_{\rm sc}$ is depressed and the SC transition in the thermal expansion is smeared out. For $B\|a$ (fig. 6.19, upper panel), the positive and small FM contribution to α_a in zero field becomes negative for $B > 1$ T increasing of ~ 100 times at $B = 6$ T with respect to the absolute value of $\Delta\alpha_a$ in zero field. The SC transition temperature is depressed in field. For $B > 0.3$ T the SC transition is difficult to track because of the scatter in the data. Also the case of α_b (fig. 6.19, middle panel) is interesting. In zero field $\Delta\alpha_b < 0$. By applying a magnetic field $B\|b$, the magnetic transition temper-

ature slightly increases and $\Delta\alpha_b$ remains negative attaining the large values of $\sim -2 \times 10^{-5}$ K^{-1} at T_C in a field of 8 T.

6.5.1 Discussion

The magnetic field has a strong, anisotropic effect on the thermal expansion of UCoGe which is in keeping with its uniaxial ferromagnet nature. For $B\|c$, i.e. along the direction of the magnetic moment m_0, the magnetic transition as measured by $\alpha_c(T)$ smears out rapidly and in field T_C cannot be defined anymore, but rather becomes a cross-over temperature T^*. For $B \perp m_0$, the magnetic transition as measured by $\alpha_a(T)$ for $B\|a$ and $\alpha_b(T)$ for $B\|b$ becomes more pronounced. The magnetic transition broadens considerably, notably in $\alpha_b(T)$, but the step sizes $|\Delta\alpha_a(B)|$ and $|\Delta\alpha_b(B)|$ increase rapidly with field as shown in the inset of fig. 6.20. This indicates the nature of the ferromagnetic transition becomes first-order-like in a magnetic field, in agreement with the phase diagram for an itinerant quantum critical point with the magnetic field playing the role of pressure [176]. The analysis of the Landau free energy of a uniaxial ferromagnet in a magnetic field predicts T_C is reduced in a transverse field $B \perp m_0$ [79]. For instance, the Curie point of the quantum Ising ferromagnet $LiHoF_4$ ($T_C = 1.53$ K) is depressed in a field applied perpendicular to the Ising axis and $T_C \to 0$ at a critical field $B_c \sim 0.5$ T [180]. The field variation of T_C of UCoGe for $B\|a$ and $B\|b$ is plotted using filled symbols in fig. 6.20. Here the Curie temperature is identified by the minimum in $\alpha_{a,b}(T)$ in field. For $B\|a$ T_C shows an small initial increase and then remains constant up to the highest field $B = 6$ T, whereas for $B\|a$ T_C shows an overall small increase. Clearly, fields exceeding 8 T are needed to depress T_C. The weak increase of T_C can be attributed to a small misorientation ($\sim 2-3$ degrees) of the field with respect to the crystallographic axes. If B is not exactly oriented perpendicular to m_0, the ferromagnetic transition becomes a cross-over due to the presence of a component of the magnetic field parallel to m_0 [77]. Recently, Aoki and collaborators [172] demonstrated the importance of a precise alignment of the magnetic field with respect to the crystal axes by carrying out an angular magnetotransport study on UCoGe. For $B\|b$ these authors report T_C remains constant in fields up to ~ 8 T and the is gradually depressed to vanish at a critical field $B_c \sim 15$ T.

In fig. 6.20 we have also traced the variation of the superconducting transition temperature as a function of the magnetic field $B\|b$ as deduced from the thermal expansion. $T_{sc}(B)$ determined in this way is systematically lower than the values determined by resistivity measurements in field on the same sample (solid line in fig. 6.20) [39]. This is expected as thermal expansion is a bulk probe and bulk superconductivity sets in when the resistive transition is

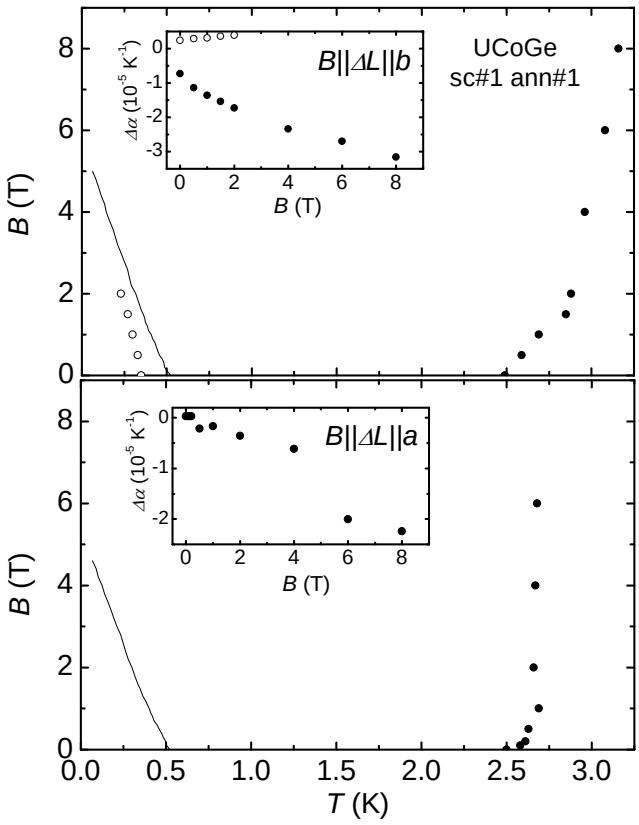

Figure 6.20: Upper critical field as a function of temperature for sc#1 ann#1 with $B\|b$ (upper frame) and $B\|a$. The filled symbols are the fields at $T_{\rm C}$, while the empty dots those for $T_{\rm sc}$ (not reported for $B\|a$). The solid line represents the values obtained from the resistivity data [39], plotted for comparison. Insets: transition height $\Delta\alpha$ as a function of the applied field.

complete (see fig. 6.4 or ref. [29]). Huy *et al.* [29] reported an overall unusual upward curvature and a change of slope ($B\|b$) or kink ($B\|a$) in the upper critical field B_{c2} near 1.5 T (solid lines in fig. 6.20). The feature near 1.5 T was tentatively attributed to a change of population of the equal spin pairing states $|\uparrow\uparrow\rangle$ and $|\downarrow\downarrow\rangle$ [39]. Interestingly, $T_C(B)$ shows a change of slope near 1.5 T (notably in $B\|b$) as well. At the moment it is not clear whether both phenomena are connected. As mentioned above, recent work by Aoki and co-workers [172] pointed out that the normal and superconducting state properties depend sensitively on the orientation of the magnetic field. Clearly, this should be considered when interpreting the data reported in fig. 6.20.

6.6 Summary

In this chapter we reported thermal expansion measurements on polycrystalline UCoGe samples which, together with specific heat, provided the first evidence for the coexistence of FM and SC in the bulk of the samples. High-temperature thermal expansion revealed the formation of a Kondo lattice state for temperatures below $T \sim 80$ K. FM and SC transitions appear in both the thermal expansion and the specific heat (figs. 6.3 and 6.4) at $T_C = 3$ K and at $T_{sc}^{bulk} = 0.45$ K. The total length change associated with SC allowed to draw the conclusion that magnetism is not expelled below T_{sc} and that FM coexists with SC. The pressure variation of T_C and T_{sc}, calculated by the Ehrenfest relation, placed UCoGe on the far side of the left SC lobe with respect to the critical point (fig. 2.4, left panel). A different phase diagram is obtained by later studies on polycrystals [41] and single crystals [42] under pressure. However, the measured $T_{C,sc}$ pressure dependence was of the same sign as given by the Ehrenfest relation.

Several single crystalline UCoGe batches have been characterized in order to obtain a high quality single crystal for thermal studies (see table 6.1). The influence of impurities and defects (represented by the RRR) on superconductivity [168] was presented in fig. 6.11. Improving the quality of the sample will not further increase T_{sc} beyond ∼0.6 K, but the width of the transition can be further reduced. The single crystalline samples with the highest RRR obtained were two bars, labelled sc#1*a* ann#1 ($RRR = 30$) and sc#1*b* ann#1 ($RRR = 40$). Despite the high quality, these sample showed no sign of reentrant superconductivity for magnetic fields up to 30 T. According to the results obtained in ref. [172], possibly a small error in the orientation hampered the observation of the field-reinforced superconductivity.

The single crystalline UCoGe samples sc#1 ann#1 were used for thermal expansion and specific heat measurements. The coefficient of linear thermal

expansion measured (fig. 6.14 and 6.15) is strongly anisotropic and FM and SC appear in the form of large steps. The large values of $\Delta\alpha$ at the transitions provide evidence for bulk FM and SC in single crystalline UCoGe. The coefficient of volume thermal expansion is presented in fig. 6.16. The data show a large negative step at $T_C = 2.6$ K and a positive step at $T_{sc}^{bulk} = 0.42$ K. An additional contribution is present below ~ 1.5 K, just before superconductivity sets in, as observed in other SCFMs [25, 92, 134, 135, 140]. This shoulder-like feature indicates the presence of a second energy scale, most likely related to an enhancement of spin fluctuations. The relative volume change due to the spontaneous magnetostriction (fig. 6.18) is much larger and has an opposite sign than the estimated $\Delta V/V$ due to SC. Specific heat, thermal expansion and resistivity are reported in fig. 6.17 around T_{sc}. A residual term γ_0 is observed when c/T is extrapolated to 0 K. The broad superconducting transition and finite γ_0-value strongly suggest sample quality is an issue here. A qualitative analysis using the Ehrenfest relation shows that for pressures applied along the b axis T_{sc} increases while T_C decreases, and vice-versa for pressures along the a and c axes.

Thermal expansion in field ($B\|\Delta L$) was measured on UCoGe sc#1 ann#1 and reported in figs. 6.19. The response of α to field is very anisotropic. While $B\|c$ suppresses the FM (and SC) transition, $B\|a, b$ enhances it. The large length changes show the nature of the FM transition becomes first-order-like in an applied magnetic field. Notably for $B\|a, b$ a change of slope in $T_C(B)$ is observed at $B = 1.5$ T. A similar result was reported for $T_{sc}(B)$ [39].

Bibliography

[1] L. D. Landau, Sov. Phys. JETP **3**, 920 (1957).

[2] L. D. Landau, Sov. Phys. JETP **5**, 101 (1957).

[3] L. D. Landau, Sov. Phys. JETP **8**, 70 (1959).

[4] H. von Löhneysen, A. Rosch, M. Vojta, and P. Wölfe, Rev. Mod. Phys. **79**, 1015 (2007).

[5] J. A. Hertz, Phys. Rev. B **14**, 1165 (1376).

[6] A. J. Millis, Phys. Rev. B **48**, 7183 (1993).

[7] T. Moriya, *Spin Fluctuations in Itinerant Electron Magnetism* (Springer, Berlin, 1985).

[8] N. Grewe and F. Steglich, in *Handbook on the Physics and Chemistry of the Rare Earths*, edited by Eds. K. A. Gschneidner Jr. and L. Eyring (Elsevier Science Pub. B.V., North Holland, 1991).

[9] S. Doniach, Physica B+C **91**, 213 (1977).

[10] G. R. Stewart, Rev. Mod. Phys. **73**, 797 (2001).

[11] G. R. Stewart, Rev. Mod. Phys. **78**, 743 (2006).

[12] P. Gegenwart, F. Kromer, M. Lang, G. Sparn, C. Geibel, and F. Steglich, Phys. Rev. Lett. **82**, 1293 (1999).

[13] R. Küchler, N. Oeschler, P. Gegenwart, T. Cichorek, K. Neumaier, O. Tegus, C. Geibel, J. A. Mydosh, F. Steglich, L. Zhu, and Q. Si, Phys. Rev. Lett. **91**, 066405 (2003).

[14] P. Gegenwart, Q. Si, and F. Steglich, Nature Physics **4**, 186 (2008).

[15] O. Trovarelli, C. Geibel, S. Mederle, C. Langhammer, F. M. Grosche, P. Gegenwart, M. Lang, G. Sparn, and F. Steglich, Phys. Rev. Lett. **85**, 626 (2000).

[16] P. Gegenwart, J. Custers, C. Geibel, K. Neumaier, T. Tayama, K. Tenya, O. Trovarelli, and F. Steglich, Phys. Rev. Lett. **89**, 056402 (2002).

[17] J. Custers, P. Gegenwart, H. Wilhelm, K. Neumaier, Y. Tokiwa, O. Trovatelli, C. Geibel, F. Steglich, C. Pèpin, and P. Coleman, Nature **424**, 524 (2003).

[18] P. Gegenwart, J. Custers, Y. Tokiwa, C. Geibel, and F. Steglich, Phys. Rev. Lett. **94**, 076402 (2005).

[19] N. Oeschler, S. Hartmann, A.P. Pikul, C. Krellner, C. Geibel, and F. Steglich, Physica B **403**, 1254 (2008).

[20] P. Gegenwart, T. Westerkamp, C. Krellner, Y. Tokiwa, S. Paschen, C. Geibel, F. Steglich, E. Abrahams, and Q. Si, Science **315**, 969 (2007).

[21] O. Stockert, H. v. Löhneysen, A. Rosch, N. Pyka, and M. Loewenhaupt, Phys. Rev. Lett. **80**, 5627 (1998).

[22] Q. Si, S. Rabello, K. Ingersent, and J. Lleweilun Smith, Nature **413**, 804 (2001).

[23] L. Zhu, M. Garst, A. Rosch, and Q. Si, Phys. Rev. Lett. **91**, 066404 (2003).

[24] S. S. Saxena, P. Agarwal, K. Ahilan, F. M. Grosche, R. K. W. Haselwimmer, M. J. Steiner, E. Pugh, I. R. Walker, S. R. Jullan, P. Monthoux, G. G. Lonzarich, A. Huxley, I. Sheikin, D. Braithwaite, and J. Flouquet, Nature **406**, 587 (2000).

[25] A. Huxley, I. Sheikin, E. Ressouche, N. Kernavanois, D. Braithwaite, R. Calemczuk, and J. Flouquet, Phys. Rev. B **63**, 144519 (2001).

[26] D. Aoki, A. Huxley, E. Ressouche, D. Braithwaite, J. Flouquet, J. P. Brison, E. Lhotel, and C. Paulsen, Nature **413**, 613 (2001).

[27] F. Hardy, A. Huxley, J. Flouquet, B. Salce, G. Knebel, D. Braithwaite, D. Aoki, M. Uhlarz, and C. Pfleiderer, Physica B **359**, 1111 (2005).

[28] T. Akazawa, H. Hidaka, T. Fujiwara, T. C. Kobayashi, E. Yamamoto, Y. Haga, R. Settai, and Y. Ōnuki, J. Phys.: Condens. Matter **16**, L29 (2004).

[29] N. T. Huy, A. Gasparini, D. E. de Nijs, Y. Huang, J. C. P. Klaasse, T. Gortenmulder, A. de Visser, A. Hamann, T. Görlach, and H. v. Löhneysen, Phys. Rev. Lett. **99**, 067006 (2007).

[30] D. Fay and J. Appel, Phys. Rev. B **22**, 3173 (1980).

[31] F. Steglich, J. Aarts, C.D. Bredl, W. Lieke, D. Meschede, W. Franz, and H. Schäfer, Phys. Rev. Lett. **43**, 1892 (1979).

[32] D. Jaccard, K. Behnia, and J. Sierro, Phys. Lett. A **163**, 475 (1992).

[33] H. Q. Yuan, F. M. Grosche, M. Deppe, C. Geibel, G. Sparn, and F. Steglich, Science **302**, 2104 (2003).

[34] H. Kamimura, H. Ushio, S. Matsuno, and T. Hamada, *Theory of Copper Oxide Superconductors* (Springer-Verlag, Berlin, 2005).

[35] H. Hosono, J. Phys. Soc. Jpn. **77**, Supplement C pp. 1 (2008).

[36] J. A. Wilson, J. Phys.: Condens. Matter **22**, 203201 (2010).

[37] W. Montfrooij, J. Lamsal, M. Aronson, M. Bennett, A. de Visser, Y.K. Huang, N.T. Huy, M. Yethiraj, M. Lumsden, and Y. Qiu, Phys. Rev. B **76**, 052404 (2007).

[38] N. T. Huy, A. Gasparini, J. C. P. Klaasse, A. de Visser, S. Sakarya, and N. H. van Dijk, Phys. Rev. B **75**, 212405 (2007).

[39] N. T. Huy, D. E. de Nijs, Y. K. Huang, and A. de Visser, Phys. Rev. Lett. **100**, 077002 (2008).

[40] D. E. de Nijs, N. T. Huy, and A. de Visser, Phys. Rev. B **77**, 140506 (2008).

[41] E. Hassinger, D. Aoki, G. Knebel, and J. Flouquet, J. Phys. Soc. Jpn. **77**, 073703 (2008).

[42] E. Slooten, T. Naka, A. Gasparini, Y. Huang, and A. de Visser, Phys. Rev. Lett. **103**, 097003 (2009).

[43] S. Sachdev, *Quantum Phase Transitions* (Cambridge University Press, Cambridge, 1999).

[44] T. Vojta, Ann. Phys (Leipzig) **9**, 403 (2000).

[45] P. Coleman and A. J. Schofield, Nature **433**, 226 (2005).

[46] A. Tari, *The Specific Heat of Matter at Low Temperatures* (Imperial College Press, London, 2003).

[47] N. W. Ashcroft and N. D. Mermin, *Solid State Physics* (Saunders College Publishing, New York, 1976).

[48] H. Ibach and H. Luth, *Solid-State Physics* (Springer-Verlag, Berlin, 1993).

[49] T. H. K. Barron, J. G. Collins, and G. K. White, Advances in Physics **29**, 609 (1980).

[50] N. H. van Dijk, Ph.D. thesis, University of Amsterdam, 1994, unpublished.

[51] K. Huang, *Statistical Mechanics* (Wiley, New York, 1987).

[52] B. Widom, J. Chem. Phys. **43**, 3892 (1965).

[53] K. G. Widom, Phys. Rev. B **4**, 3174 (1971).

[54] D. V. Schroeder, *An Introduction to Thermal Physics* (Addison Wesley Longman, US, 1999).

[55] K. G. Wilson, Phys. Rev. B **4**, 3174 (1971).

[56] S. Chakravarty, B. I. Halperin, and D. R. Nelson, Phys. Rev. Lett. **60**, 1057 (1988).

[57] S. Chakravarty, B. I. Halperin, and D. R. Nelson, Phys. Rev. B **39**, 2344 (1989).

[58] P. Coleman, Physica B **353**, 259 (1999).

[59] L. Zhu, Ph.D. thesis, Rice University, 2004, unpublished.

[60] D. Belitz, T. R. Kirkpatrick, M. T. Mercaldo, and S. L. Sessions, Phys. Rev. B **63**, 174427 (2001).

[61] A. Dommann, F. Hulliger, and T. Siegrist, J. Magn. Magn. Mat. **67**, 323 (1987).

[62] S. Sakarya, W. Knafo, N. H. van Dijk, Y. Huang, K. Prokes, C. Meingast, and H. v. Löhneysen, J. Phys. Soc. Jpn. **79**, 014702 (2010).

[63] A. de Visser, in *Encyclopedia of Materials: Science and Technology (pp 1-6)*, edited by Eds. K H. J. Buschow *et al* (Elsevier, Oxford, 2010).

[64] J. Bardeen, L. N. Cooper, and J. R. Schrieffer, Phys. Rev. **108**, 1175 (1957).

[65] D. D. Osheroff, R. C. Richardson, and D. M. Lee, Phys. Rev. Lett. **28**, 885 (1972).

[66] A. J. Leggett, Rev. Mod. Phys. **47**, 331 (1975).

[67] H. R. Ott, H. Rudigier, Z. Fisk, and J. L. Smith, Phys. Rev. Lett. **50**, 1595–1598 (1983).

[68] A. de Visser, N. H. van Dijk, K. Bakker, J. J. M. Franse, A. Lacerda, J. Flouquet, Z. Fisk, and J. L. Smith, Phys. Rev. B **45**, 2962 (1992).

[69] H. Q. Yuan, F. M. Grosche, M. Deppe, C. Geibel, G. Sparn, and F. Steglich, Science **302**, 5653 (2003).

[70] F. de Boer, J. C. P. Klaasse, P. A. Veenhuizen, A. Bohm, C. D. Bredl, U. Gottwick, H. M. Mayer, L. Pawlak, U. Rauchschwalbe, H. Spille, and F. Steglich, J. Magn. Magn. Mat. **63**, 91 (1987).

[71] R. Felten, G. Weber, and H. Rietschel, J. Magn. Magn. Mat. **63**, 383 (1987).

[72] G. R. Stewart, Z. Fisk, J. O. Willis, and J. L. Smith, Phys. Rev. Lett. **52**, 679–682 (1984).

[73] R. A. Fisher, S. Kim, B. F. Woodfield, N. E. Phillips, L. Taillefer, K. Hasselbach, J. Flouquet, A. L. Giorgi, and J. L. Smith, Phys. Rev. Lett. **1989**, 1411 (Phys. Rev. Lett.).

[74] T. T. M. Palstra, A. A. Menovsky, J. van den Berg, A. J. Dirkmaat, P. H. Kes, G. J. Nieuwenhuys, and J. A. Mydosh, Phys. Rev. Lett. **55**, 2727–2730 (1985).

[75] N. K. Sato, N. Aso, K. Miyake, R. Shiina, P. Thalmeier, G. Varelogiannis, C. Geibel, F. Steglich, P. Fulde, and T. Komatsubara, Nature **410**, 340 (2001).

[76] T. R. Kirkpatrick and D. Belitz, Phys. Rev. B **67**, 024515 (2003).

[77] V. P. Mineev, Advances in theoretical physics: Landau Memorial Conference **1134**, 68 (2009).

[78] V. P. Mineev and T. Champel, Phys. Rev. B **69**, 144521 (2004).

[79] V. P. Mineev, arXiv: 1002.3510v1 (unpublished).

[80] Oxford Instruments, *Heliox VL*, http://www.oxford-instruments.com/.

[81] Oxford Instruments, *Kelvinox MX100*, http://www.oxford-instruments.com/.

[82] J. C. P. Klaasse, Rev. Sci. Instrum. **68**, 89 (1997).

[83] J. C. P. Klaasse, I. H. Hagmusa, and E. Brück, Rev. Sci. Instrum. **68**, 4208 (1997).

[84] National Instruments, http://www.ni.com/labview/.

[85] Z. Koziol, Ph.D. thesis, University of Amsterdam, 1994, unpublished.

[86] A. F. Deutz, R. Hulstaman, and F. J. Kranenburg, Rev. Sci. Instrum. **60**, 113 (1988).

[87] D. Martien, Introduction to ac Susceptibility, Quantum Design, San Diego (2002).

[88] F. R. Kroeger and C. A. Swenson, J. Appl. Phys. **48**, 853 (1977).

[89] G. K. White, Cryogenics **1**, 151 (1961).

[90] A. de Visser, Ph.D. thesis, University of Amsterdam, 1986, unpublished.

[91] M. Nazih, Master's thesis, Universiteit van Amsterdam, 2002, unpublished.

[92] N. T. Huy, Ph.D. thesis, University of Amsterdam, 2008, unpublished.

[93] K. Alberta, H. v. Löhneysen, W. Sandera, and H. J. Schinka, Cryogenics **22**, 417 (1982).

[94] W. Montfrooij, M. C Aronson, B. D. Rainford, J. A. Mydosh, A. P. Murani, P. Haen, and T. Fukuhara, Phys. Rev. Lett. **91**, 087202 (2003).

[95] M. B. Fontes, M. A. Continentino, S. L. Bud'ko, M. El-Massalami, L. C. Sampaio, A. P. Guimaraes, E. Baggio-Saitovitch, M. F. Hundley, and A. Lacerda, Phys. Rev. B **53**, 11678 (1996).

[96] H. Rietschel, B. Renker, R. Felten, F. Steglich, and G. Weber, J. Magn. Magn. Mat. **76**, 105 (1988).

[97] L. C. Gupta, D. E. MacLaughlin, Cheng Tien, C. Gordart, M. A. Edwards, and R. D. Parks, Phys. Rev. B **28**, 3673 (1983).

[98] C. A. King and G. G. Lonzarich, Physica B **171**, 161 (1991).

[99] A. Loidl, K. Knorr, G. Knopp, A. Krimmel, R. Caspary, A. Böhm, G.Sparn, C. Geibel, F. Steglich, and A. P. Murani, Phys. Rev. B **46**, 9341 (1992).

[100] A. Loidl, G. Knopp, H. Spille, F. Steglich, and A. P. Murani, Physica B **156**, 794 (1989).

[101] Z. Ban and M. Sikirica, Acta Crystallogr. **18**, 594 (1965).

[102] M. J. Besnus, J. P. Kappler, P. Lehmann, and A. Meyer, Solid State Commun. **55**, 779 (1985).

[103] S. Raymond, P. Haen, R. Calemczuk, S. Kambe, B. Fåk, P. Lejay, T. Fukuhara, and J. Flouquet, J. Phys.: Condens. Matter **11**, 5547 (1999).

[104] H. Wilhelm, K. Alami-Yadri, B. Revaz, and D. Jaccard, Phys. Rev. B **59**, 3651 (1999).

[105] Y. Uwatoko, G. Oomi, T. Graf, J. D. Thompson, P. C. Canfield, H. A. Borges, C. Godart, and L. C. Gupta, Physica B **206**, 234 (1995).

[106] J. D. Thompson, Y. Uwatoko, T. Graf, M. F. Hundley, D. Mandrus, C. Godart, L. C. Gupta, P. C. Canfield, A. Migliori, and H. A. Borges, Physica B **199**, 589 (1994).

[107] S. Süllow, M. C. Aronson, B. D. Rainford, and P. Haen, Phys. Rev. Lett. **82**, 2963 (1999).

[108] H. Wilhelm and D. Jaccard, Physica B **256**, 78 (1999).

[109] H. Wilhelm and D. Jaccard, Phys. Rev. B **69**, 214408 (2004).

[110] W. Montfrooij, M. C. Aronson, B. D Rainford, J. A. Mydosh, R. Heindrikx, T. Gortenmulder, A. P. Murani, P. Haen, I. Swainson, and A. de Visser, Phys. Rev. B **73**, 140401 (2006).

[111] F. Givord, J.-X. Boucherle, E. Lelievre-Berna, and P. Lejay, J. Phys.: Condens. Matter **16**, 1211 (2004).

[112] W. Montfrooij, J. Lamsal, M. Aronson, M. Bennett, A. de Visser, H. Ying Kai, N. T. Huy, M. Yethiraj, M. Lumsden, and Y. Qiu, arXiv:cond-mat/0606703 (unpublished).

[113] N. T. Huy et al. (unpublished).

[114] T. Ebihara, K. Motoki, H. Toshima, M. Takashita, N. Kimura, H. Sugawara, K. Ichihashi, R. Settai, Y. Onuki, Y. Aoki, and H. Sato, Physica B **260**, 219 (1995).

[115] A. de Visser, P. Haen, P. Lejay, and J. Flouquet, Journal de Physique **C8**, 767 (1988).

[116] M. J. Besnus, A. Essaihi, N. Hamdaoui, G. Fischer, J. P. Kappler, A. Meyer, J. Pierre, P. Haen, and P. Lejay, Physica B **171**, 350 (1991).

[117] I. Felner, I. Mayer, A. Grill, and M. Schieber, Solid State Commun. **16**, 1005 (1975).

[118] M. B. Fontes, S. L. Bud'ko, M. A. Continentino, and E. M. Baggio-Saitovitch, Physica B **270**, 255 (1999).

[119] K. Kadowaki and S. B. Woods, Solid State Commun. **58**, 507 (1986).

[120] P. Gegenwart, J. Custers, Y. Tokiwa, C. Geibel, and F. Steglich, Phys. Rev. Lett. **94**, 076402 (2005).

[121] F. Bouquet, Y. Wang, H. Wilhelm, D. Jaccard, and A. Junod, Solid State Commun. **113**, 367 (2000).

[122] Y. Tokiwa, T. Radu, C. Geibel, F. Steglich, and P. Gegenwart, Phys. Rev. Lett. **102**, 066401 (2009).

[123] P. Thalmeier and P. Fulde, Europhys. Lett. **1**, 367 (1986).

[124] A. Lacerda, A. de Visser, P. Haen, P. Lejay, and J. Flouquet, Phys. Rev. B **40**, 8759 (1989).

[125] P. Gegenwart, Y. Tokiwa, T. Westerkamp, F. Weickert, J. Custers, J. Ferstl, C. Krellner, C. Geibel, P. Kerschl, K.H. Müller, and F. Steglich, New J. Phys. **8**, 171 (2006).

[126] S. Sakarya, N.H. van Dijk, N.T. Huy, and A. de Visser, Physica B **378-380**, 970 (2006).

[127] J. G. Sereni, T. Westerkamp, R. Küchler, N. Caroca-Canales, P. Gegenwart, and C. Geibel, Phys. Rev. B **75**, 024432 (2007).

[128] T. Westerkamp, M. Deppe, R. Küchler, M. Brando, C. Geibel, P. Gegenwart, A. P. Pikul, and F. Steglich, Phys. Rev. Lett. **102**, 206404 (2009).

[129] M. Brando, T. Westerkamp, M. Deppe, P. Gegenwart, C. Geibel, and F. Steglich, Journal of Physics: Conference Series **200**, 012016 (2010).

[130] D. A. Sokolov, M. C. Aronson, W. Gannon, and Z. Fisk, Phys. Rev. Lett. **96**, 116404 (2006).

[131] V. H. Tran, R. Troć, and G. Andrè, J. Magn. Magn. Mat. **186**, 81 (1998).

[132] G. G. Lonzarich and L. Taillefer, J. Phys. C: Solid State Phys. **18**, 4339 (1985).

[133] F. Lèvy, I. Sheikin, B. Grenier, and A. D. Huxley, Science **309**, 1343 (2005).

[134] S. Sakarya, N. H. van Dijk, A. de Visser, and E. Brück, Phys. Rev. B **67**, 144407 (2003).

[135] S. Sakarya, N. T. Huy, N. H. van Dijk, A. de Visser, M. Wagemaker, A. C. Moleman, T. J. Gortenmulder, J. C. P. Klaasse, M. Uhlarz, and H. v. Löhneysen, J. Alloys Compd. **457**, 51 (2008).

[136] V. Sechovský and L. Havela, in *Handbook of Magnetic Materials, vol 11, pp. 1-289*, edited by K. H. J. Buschow (Elsevier, North Holland, 1998).

[137] R. Troc̀ and V. H. Tran, J. Magn. Magn. Mat. **73**, 389 (1988).

[138] C. Pfleiderer, S. R. Julian, and G. G. Lonzarich, Nature **414**, 427 (2001).

[139] S. Sakarya, Ph.D. thesis, Delft University of Technology, 2007, unpublished.

[140] K. Prokeš, T. Tahara, Y. Echizen, T. Takabatake, T. Fujita, I. H. Hagmusa, J. C. P. Klaasse, E. Brück, F. R. de Boer, M. Diviš, and V. Sechovský, Physica B **311**, 220 (2002).

[141] I. H. Hagmusa, K. Prokeš, Y. Echizen, T. Takabatake, T. Fujita, J.C.P. Klaasse, E. Brück, V. Sechovský, and F. R. de Boer, Physica B **281**, 223 (2000).

[142] An equal volume for the broadened and idealized contributions is imposed when integrating $\alpha(T)$ or $\beta(T)$ with respect to the background signal.

[143] Hercules (different authors), in *Neutron and Synchrotron Radiation for Condensed Matter Studies*, edited by J. Baruchel J.L. Hodeau M.S. Lehmann J.R. Regnard C. Schlenker (Les Edition de Physique and Springer-Verlag, Berlin, 1994).

[144] H. Duijn, Ph.D. thesis, University of Amsterdam, 2000, unpublished.

[145] J. G. Sereni, R. Küchler, and C. Geibel, Physica B **378–380**, 648–649 (2006).

[146] R. Küchler, P. Gegenwart, J. Custers, O. Stockert, N. Caroca-Canales, C. Geibel, J. G. Sereni, and F. Steglich, Phys. Rev. Lett. **96**, 256403 (2006).

[147] M. Garst and A. Rosch, Phys. Rev. B **72**, 205129 (2005).

[148] H. v. Löhneysen, T. Pietrus, G. Portisch, H. G. Schlager, A. Schröder, M. Sieck, and T. Trappmann, Phys. Rev. Lett. **72**, 3262 (1994).

[149] P. Pedrazzini, M. Gómez Berisso, N. Caroca-Canales, M. Deppe, C. Geibel, and J. G. Sereni, Physica B **312**, 406 (2002).

[150] R. Küchler, P. Gegenwart, K. Heuser, E.-W. Scheidt, G. R. Stewart, and F. Steglich, Phys. Rev. Lett. **93**, 096402 (2004).

[151] R. Küchler, P. Gegenwart, K. Heuser, E.-W. Scheidt, G.R. Stewart, and F. Steglich, Physica B **359**, 53 (2005).

[152] B. Lloret, Ph.D. thesis, University Bordeaux I, 1988, unpublished.

[153] K. H. J. Buschow, E. Brück, R. G. Wierst, F. R. de Boer, L. Havela, V. Sechovsky, and P. Nozar, J. Appl. Phys. **67**, 5215 (1990).

[154] N. T. Huy and A. de Visser, Solid State Comm. **149**, 703 (2009).

[155] F. Canepa, P. Manfrinetti, M. Pani, and A. Palenzona, J. Alloys Compd. **234**, 225 (1996).

[156] E. P. Wohlfarth, Physica **91B**, 305 (1977).

[157] N. H. van Dijk, A. de Visser, J. J. M. Franse, and A. A. Menovsky, Phys. Rev. B **51**, 12665 (1995).

[158] N. H. van Dijk, A. de Visser, J. J. M. Franse, S. Holtmeier, L. Taillefer, and J. Flouquet, Phys. Rev. B **48**, 1299 (1993).

[159] N. H. van Dijk, A. de Visser, and J. J. M. Franse, J. Low Temp. Phys. **93**, 101 (1993).

[160] A. de Visser, N. T. Huy, A. Gasparini, D. E. de Nijs, D. Andreica, C. Baines, and A. Amato, Phys. Rev. Lett. **102**, 167003 (2009).

[161] T. Ohta, T. Hattori, K. Ishida, Y. Nakai, E. Osaki, K. Deguchi, N. K. Sato, and I. Satoh, J. Phys. Soc. Jpn. **79**, 023707 (2010).

[162] D. Aoki, A. Huxley, F. Hardy, D. Braithwaite, E. Ressouche, J. Flouquet, J. P. Brison, and C. Paulsen, Acta Phys. Pol. B **34**, 503 (2003).

[163] A. P. Mackenzie and Y. Maeno, Rev. Mod. Phys. **75**, 657 (2003).

[164] N. Kikugawa, A. P. Mackenzie, and Y. Maeno, J. Phys. Soc. Jpn. **72**, 237 (2003).

[165] N. T. Huy, Y. K. Huang, and A. de Visser, J. Magn. Magn. Mat. **321**, 2691 (2009).

[166] F. Hardy, Ph.D. thesis, University Joseph Fourier, Grenoble, 2004, unpublished.

[167] E. Yamamoto, Y. Haga, T. D. Matsuda, Y. Inada, R. Settai, Y. Tokiwa, and Y. Onuki, Acta Phys. Pol. **34**, 1059 (2003).

[168] A. J. Millis, S. Sachdev, and C. M. Varma, Phys. Rev. B **37**, 4675 (1988).

[169] A. A. Abrikosov and L. P. Gor'kov, Zh. Eksp. Teor. Fiz. **39**, 1781 (1960).

[170] A. A. Abrikosov and L. P. Gor'kov, Soviet Phys. JETP **12**, 1243 (1961).

[171] A. P. Mackenzie, R. K. W. Haselwimmer, A. W. Tyler, G. G. Lonzarich, Y. Mori, S. Nishizaki, and Y. Maeno, Phys. Rev. Lett. **80**, 161 (1998).

[172] D. Aoki, T. D. Matsuda, V. Taufour, E. Hassinger, G. Knebel, and J. Flouquet, J. Phys. Soc. Jpn **78**, 113709 (2009).

[173] M. Sigrist and K. Ueda, Rev. Mod. Phys. **63**, 239 (1991).

[174] C. M. Varma, Comm. Solid State Phys. **11**, 221 (1985).

[175] G. Oomi, K. Nishimura, Y. Ōnuki, and S. W. Yun, Physica B **186**, 758 (1993).

[176] D. Belitz and T. R. Kirkpatricks, Phys. Rev. B **69**, 184502 (2004).

[177] J. J. M. Franse, A. Menovsky, A. de Visser, C. D. Bredl, U. Gottwick, W. Lieke, H. M. Mayer, U. Rauchschwalbe, G. Sparn, and F. Steglich, Z. Phys. B **59**, 15 (1985).

[178] R. A. Fisher, S. Kim, B. F. Woodfield, N. E. Phillips, L. Taillefer, K. Hasselbach, J. Flouquet, A. L. Giorgi, and J. L. Smith, Phys. Rev. Lett. **62**, 1411 (1989).

[179] The value of dTs/dp in ref. [29] should read 0.020 K/kbar. Notice, this value and dT_C/dp = -0.25 K/kbar refer to uniaxial pressure dependencies, since they are evaluated using $\Delta\alpha$ rather than $\Delta\beta$.

[180] D. Bitko, T. F. Rosenbaum, and G. Aeppli, Phys. Rev. Lett. **77**, 940 (1996).

[181] M. A. Schwartz, Journal of Cell Science **121**, 1771 (2008).

Summary

The Grüneisen parameter has been shown to be a powerful detection tool for quantum criticality, shortly after Zhu *et al.* [23] predicted its divergence $\Gamma(T) \propto T^{-\nu z}$ at every QCP. The temperature exponent νz of the diverging Γ provides important information regarding the type of quantum criticality, giving the product of ν, the critical exponent of the correlation length, and z, the critical exponent of the correlation time. Therefore the goal of this thesis was to focus on different types of QCPs, such as FM and AFM QCPs. Moreover, the discovery of superconductivity coexisting with ferromagnetism in UCoGe [29] and the evidence of FM QCPs in systems with Si-doping [40] or under pressure [42] gave the possibility to study other FM QCPs with the help of the Grüneisen ratio. Here we reported the thermal properties of pure UCoGe at ambient pressure, which presented the first evidence of bulk SC and FM.

In *chapter 3* different experimental techniques are presented. In particular the dilatometry technique is implemented over a wide temperature range (30 mK -150 K) for two different cells. Cell-1 was calibrated to be used in the Heliox and Kelvinox systems (30 mK-20 K) and cell-2 for the glass-dewar system (2-150 K). At very low temperatures ($T < 100$ mK) a minimum in the calibration function is found. Its origin is still unclear, but it is possibly related to a two level Schottky system. Experiments carried out in field corroborated this hypothesis.

Chapter 4 is devoted to the AFM QCP in $Ce(Ru_{0.24}Fe_{0.76})_2Ge_2$. The single crystalline sample is shown to have a Fe-concentration $x \sim 0.75$, which is lower than the nominal one, and $T_N \sim 1.2$ K, therefore AFM order is still present in the sample. The AFM was suppressed by applying a small magnetic field. From magnetostriction and magnetoresistance measurements, we consider $B_c \sim 0.8$ T. The resistivity exponent n from the data fitted by $\rho(T) = \rho_0 + aT^n$ showed a minimum $n = 1.3$ at $B \sim B_c$. The result is lower than the one predicted for a SDW AFM QCP, which is n=3/2, possibly due

to crystallographic disorder.

Thermal expansion and specific heat were studied in several applied magnetic fields and the Grüneisen ratio was calculated. The thermal expansion data fitted by a power law function $\beta = aT^n$ present a minimum $n = 1$ for $B \sim B_c$. For the specific heat divided by the temperature c/T at $T = 0.5$ K we reported the highest value $\gamma = 0.83$ J/mol K^2 for $B \sim B_c$. Both parameters deviate from the prediction for a SDW AFM QCP. At the critical field, the Grüneisen ratio reaches high values at low temperatures ($\Gamma_{mag} = 50$ at 0.5 K). Nevertheless the specific heat and the thermal expansion at $B \sim B_c$ are not compatible with the prediction for a SDW AFM QCP and Γ does not diverge. This was not unexpected since (i) the system presents competing local and long-range fluctuations at the QCP, (ii) the system is above the upper critical dimension and (iii) if different Γ ratio's do not couple due to the presence of more than one energy scale, only Γ_{mag} is predicted to diverge when the magnetic field is used as control parameter.

The thermal expansion and specific heat experiments on a FM SDW QCP are reported in *chapter 5*. The thermal expansion data on the polycrystalline U(Rh,Ru)Ge series ($x = 0.10, 0.20$ and $x_c = 0.38$) are combined with specific heat data taken previously on the same samples in order to obtain the Grüneisen ratio Γ towards the QCP. The transition temperatures obtained by thermal expansion are in very good agreement with the ones of the previously reported phase diagram. Although no diverging Γ is reported for $x = 0.38$, a steady rise of the Grüneisen ratio is observed in the paramagnetic regime on approach of the FM transition.

We then investigated the thermal properties of single crystalline samples of $URh_{0.62}Ru_{0.38}Ge$. AC-susceptibity revealed that the samples under study were still ferromagnetic and therefore the Ru-concentration was lower than x_{cr}. Moreover, a typical variation of 2% in the Rh/Ru ratio was observed along the crystal pulling direction applied during the Czochralski growth. The thermal expansion results of one $URh_{0.62}Ru_{0.38}Ge$ sample (nominal critical concentration) are compared with the specific heat data on the same sample. In both data sets the FM transition is observed. The calculated Grüneisen ratio presents a large plateau to drop at $T \sim 1$ K due to FM. We showed that this behaviour is not inconsistent with the theory proposed by ref. [23].

In *chapter 6* we reported thermal expansion measurements on polycrystalline UCoGe, which provided the first evidence of coexistence of SC and FM in the bulk of the sample. This was concluded since the steps at the transitions were large and the total length associated to SC was small compared to

the one associated to FM. High temperature thermal expansion revealed the formation of a Kondo lattice state for $T < 80$ K. The FM and SC transition temperatures, $T_C = 3$ K and $T_{sc}^{bulk} = 0.45$ K, are in good agreement with resistivity and ac-susceptibility data and the SC transition in thermal expansion and the specific heat appears when the resistivity drops to zero.

An annealing study of the single crystalline samples was performed in order to improve their quality. The single crystals with the highest quality that were previously obtained were two bar-shaped samples with $RRR = 30$ and 40. From our study it is clear that the SC transition temperature will not increase much further when increasing the RRR, but the width of the SC transition can decrease with improving samples quality. The thermal expansion data confirmed bulk FM and SC at $T_C = 2.6$ K and $T_{sc}^{bulk} = 0.42$ K. An additional contribution is present below ~ 1.5 K, just before superconductivity sets in, as it was already observed in other SCFMs. This shoulder-like feature indicates the presence of a second energy scale, most likely related to an enhancement of the spin fluctuations. A qualitative analysis using the Ehrenfest relation showed that T_{sc} increases while T_C decreases when pressure is applied along the b axis, and vice-versa for pressures applied along the a and c axes. Thermal expansion on single crystalline UCoGe revealed a very anisotropic response to magnetic field. For an external magnetic field $B \| \Delta L$, T_C is suppressed in a small magnetic field when $B \| m_0$ while T_C stays around the same value up to a magnetic field of 8 T when $B \perp m_0$. The step size considerably increased when a field $B \perp m_0$ was applied. It would be of high interest to use these results in order to study the Grüneisen parameter in a field tuned QCP in UCoGe.

Samenvatting

In 2003 voorspelden Zhu et al. dat de Grüneisenparameter $\Gamma(T)$, de experimentele maat voor de verhouding van de coëfficient van de thermische uitzetting, $\alpha(T)$, en de soortelijke warmte, $c(T)$, divergeert bij elk kwantum kritisch punt. De divergentie wordt gegeven door $\Gamma(T) \propto T^{-\nu z}$, waarbij ν de kritische exponent van de correlatielengte is en z van de correlatietijd. Dit maakt de Grüneisenparameter een zeer krachtig instrument om kwantum kritikaliteit te bestuderen. Het doel van dit proefschrift is dan ook om de Grüneisenparameter te onderzoeken voor magnetische kwantum kritische punten, zowel voor een antiferromagnetische (AFM) als ferromagnetische (FM) grondtoestand. Daarnaast gaf de ontdekking van coëxistentie van supergeleiding en ferromagnetisme in UCoGe, een systeem dat vlak bij een FM kwantum kritisch punt is, aanleiding om de thermische eigenschappen van diverse preparaten in detail te bestuderen.

In *hoofdstuk 3* worden de gebruikte experimentele technieken beschreven. Met name de techniek om thermische uitzetting te meten komt aan bod. Om over een breed temperatuurgebied te meten zijn twee capacitieve uitzettingscellen gebruikt. Cel-1 werd geijkt voor de Heliox en Kelvinox systemen (T=0.03-20 K) en cel-2 voor gebruik in een glazen bad-cryostaat (T=2-150 K). Bij zeer lage temperatuur ($T < 0.1$ K) werd een minimum in de cel-functie gevonden. De exacte oorzaak hiervan is nog onduidelijk, maar de analyse duidt op de aanwezigheid van een twee-niveau Schottky systeem. Metingen in een extern magneetveld ondersteunen deze hypothese.

Hoofdstuk 4 beschrijft een experimentele studie aan het AFM kwantum kritisch punt in $Ce(Ru_{0.24}Fe_{0.76})_2Ge_2$. De experimenten uitgevoerd aan éénkristallijne preparaten tonen aan dat de werkelijke concentratie Fe (geschat op 75 at.%) een fractie lager is dan de nominale concentratie (76 at.%), waardoor het preparaat nog AFM ordent met een Néel temperatuur $T_N \sim 1.2$ K. De AFM ordening kan onderdrukt worden met behulp van een klein uitwendig magneetveld. Het kritische veld, $B_c \sim 0.8$ T, is bepaald door middel van

magnetostrictie- en magnetoweerstandsmetingen. De temperatuurexponent n in de electrische weerstand, $\rho(T) = \rho_0 + aT^n$, vertoont een minimum n=1.3 bij $B \sim B_c$. Deze waarde is kleiner dan n=1.5 voorspeld voor een itinerant (spin density wave) AFM kwantum kritisch punt. Dit is toe te schrijven aan het feit dat het preparaat een quasi-ternaire verbinding is met een hoge restweerstand ρ_0.

De volume thermische uitzettingscoefficient, $\beta(T)$, en soortelijke warmte werden gemeten in verschillende magneetvelden en de Grüneisenparameter bepaald. De thermische uitzettingsdata werden gefit aan een machtswet-functie $\beta = aT^n$, met een minimum n=1 voor $B \sim B_c$. De lineaire coëfficient in de soortelijke warmte heeft een maximum bij $B \sim B_c$: $c/T|_{0.5\ \mathrm{K}} = 0.83\ \mathrm{J/mol\ K^2}$. Beide parameters wijken af van de voorspellingen voor een itinerant AFM kwantum kritisch punt. De Grüneisenparameter bereikt zeer hoge waarden bij lage temperaturen ($\Gamma_{\mathrm{mag}} = 50$ bij 0.5 K), maar divergeert niet. Dit is niet onverwacht omdat: (i) neutronenverstrooiingsexperimenten tonen aan dat het $Ce(Ru,Fe)_2Ge_2$ systeem met elkaar wedijverende lokale en lange-afstandsfluctuaties vertoont bij het kwantum kritisch punt, (ii) het systeem is boven de bovenste kritische dimensie, en (iii) de aanwezigheid van meer dan één energieschaal kan er toe leiden dat de verschillende Γ parameters niet koppelen; Γ_{mag} divergeert dan alleen wanneer het magneetveld wordt gebruikt als *tuning* parameter.

Thermische uitzettingsmetingen aan een FM spin density wave kwantum kritisch punt worden gepresenteerd in *hoofdstuk 5*. De thermische uitzettingsdata van een reeks van polykristallijne $URh_{1-x}Ru_xGe$ preparaten ($x = 0.10, 0.20$ en $x_c = 0.38$) worden gecombineerd met eerder verkregen soortelijke warmte data, teneinde de Grüneisenparameter te berekenen. De gemeten magnetische overgangstemperaturen (Curie temperatuur, T_C) komen zeer goed overeen met het eerder gerapporteerde $T_C(x)$ fasediagram. Voor de kritische concentratie, $x_c = 0.38$, van het polykristallijne preparaat werd geen divergerende $\Gamma(T)$ gevonden. Wel neemt de Grüneisenparameter gestaag toe bij de nadering van de ferromagnetische overgang vanuit het paramagnetische regime.

Vervolgens werden de thermische eigenschappen van diverse éénkristallen met nominale samenstelling $URh_{0.62}Ru_{0.38}Ge$ onderzocht. Susceptibiliteitsmetingen onthullen dat alle bestudeerde kristallen ferromagnetische ordening vertonen en dat de werkelijke Ru-concentratie lager is dan $x_c = 0.38$. Dit is een gevolg van de variatie van de Rh/Ru verhouding van ongeveer 2% langs de Czochralski groeirichting van het kristal. Thermische uitzettingsdata aan een dergelijk $URh_{0.62}Ru_{0.38}Ge$ éénkristal zijn vergeleken met de soortelijke warm-

te data van hetzelfde preparaat. In beide datasets wordt de FM-overgang waargenomen. De Grüneisenparameter vertoont een breed plateau bij lage temperatuur en valt abrubt weg bij $T \sim 1$ K vanwege de ferromagnetisch ordening. Dit gedrag kan de theorie van Zhu et al. niet bevestigen, maar is ook niet in tegenstrijd daarmee.

Hoofdstuk 6 is gewijd aan de supergeleidende ferromagneet UCoGe. Diverse experimenten zijn uitgevoerd aan poly- en éénkristallijne preparaten. Thermische uitzettingsmetingen aan polykristallijne preparaten UCoGe vormden het eerste bewijs dat supergeleiding en ferromagnetisme daadwerkelijk coëxisteren in de bulk van het preparaat. Deze conclusie kon worden getrokken aan de hand van de grootte van de stappen in de thermische uitzettingscoëficient bij de overgangstemperaturen. De ferromagnetische en supergeleidende overgangstemperaturen, $T_{\rm C} = 3$ K en $T_{\rm sc}^{\rm bulk} = 0.45$ K komen goed overeen met weerstands- en ac-susceptibiliteitsdata. Thermische uitzettingsmetingen bij hoge temperatuur onthullen de formatie van een Kondo-rooster bij temperaturen $T < 80$ K.

Teneinde de kwaliteit van diverse éénkristallijne preparaten te verbeteren is het effect van verschillende warmtebehandelingen (gloeien) bestudeerd. Eerder was aangetoond dat een warmtebehandeling van 1 dag bij 1250 °C en 21 dagen bij 880 °C resulteert in aanzienlijke toename van de kwaliteit en een restweerstandsverhouding RRR =30-40. Echter, gelijksoortige warmtebehandelingen aan nieuw gegroeide éénkristallen leidden niet tot de gewenste hoge RRR waarden. Aan de kristallen met RRR =30-40 zijn thermische uitzettingsmetingen uitgevoerd. De data laten een sterke anisotropie in $\alpha(T)$ zien, met de grootste lengteveranderingen voor de orthorhombische b as. De grote waarden van de stappen in $\alpha(T)$ bij $T_{\rm sc}^{\rm bulk} = 0.42$ K en $T_{\rm C} = 2.6$ K tonen bulk supergeleiding en magnetisme aan. Interessant is dat een extra bijdrage in $\alpha(T)$ vlak boven $T_{\rm sc}^{\rm bulk}$ werd gevonden. Deze bijdrage duidt op de aanwezigheid van een tweede energie-schaal, die hoogst waarschijnlijk verband houdt met een versterking van spin fluctuaties, zoals waargenomen in de supergeleidende ferromagneten UGe2 en URhGe. Tot slot is het effect van een longitudinaal magneetveld op $\alpha(T)$ bestudeerd: de thermische uitzetting neemt sterk toe, hetgeen duidt op een verandering van het karakter van de magnetische faseovergang van tweede naar eerste orde in veld.

List of publications

Papers by the author related to this thesis:

Chapter 5

Evidence for a ferromagnetic quantum critical point in URhGe doped with Ru
N. T. Huy, D. E. de Nijs, A. Gasparini, J. C. P. Klaasse, A. de Visser and N. H. van Dijk
Physica B **403** (2008) 1260-1261

Ferromagnetic quantum critical point in URhGe doped with Ru
N. T. Huy, A. Gasparini, J. C. P. Klaasse, A. de Visser, S. Sakarya, and N. H. van Dijk
Phys. Rev. B **75** (2007) 212405-1:4

Chapter 6

Thermal expansion of the superconducting ferromagnet UCoGe
A. Gasparini, Y. K. Huang, J. Hartbaum, H. v. Löhneysen, and A. de Visser
Phys. Rev. B **82** (2010) 052502

The superconducting ferromagnet UCoGe
A. Gasparini, Y. K. Huang, N. T. Huy, J. C. P. Klaasse, T. Naka, E. Slooten, and A. de Visser
to be published in Journal of Low Temperature Physics (Special issue: Quantum Phase Transitions 2010) doi: 10.1007/s10909-010-0188-1

Enhancement of superconductivity near the ferromagnetic quantum critical point in UCoGe
E. Slooten, T. Naka, A. Gasparini, Y. K. Huang, and A. de Visser
Phys. Rev. Lett. **103** 097003 (2009)

Muon spin rotation and relaxation in the superconducting ferromagnet UCoGe
A. de Visser, N. T. Huy, A. Gasparini, D. E. de Nijs, D. Andreica, C. Baines, and A. Amato
Phys. Rev. Lett. **102**, 167003 (2009)

Superconductivity on the border of weak itinerant ferromagnetism in UCoGe
N. T. Huy, A. Gasparini, D. E. de Nijs, Y. Huang, J. C. P. Klaasse, T. Gortenmulder, A. de Visser, A. Hamann, T. Görlach, and H. v. Löhneysen
Phys. Rev. Lett. **99**, 067006 (2007)

Other papers by the author:

New details of the Fermi surface of 2H-$NbSe_2$ revealed by quantum oscillation in the magnetostriction
V. Sirenko, A. Gasparini, A. de Visser, V. Emerenko, V. Ibulaev and V. Bruk
J. Phys.: Conference Series **150** (2009) 042185-1:4

Thermal expansion of $LaFeAsO_{1-x}F_x$: Evidence for high temperature fluctuations
L. Wang, U. Köhler, N. Leps, A. Kondrat, M. Nale, A. Gasparini, A. de Visser, G. Behr, C. Hess, R. Klingeler and B. Büchner
Phys. Rev. B **80** (2009) 094512-1:5

Acknowledgements

Omg, a phase separation!

anonymus nerd
watching the whipped cream
turning into butter

you can keep walking all over me,
I am not getting any shorter

vale

[...] Cerco introvabili risposte
dentro ogni emozione

ela

Many people have to be thanked for the realization of this thesis work and for making this stay in Amsterdam a joyful 'Chihiro's journey'. Despite the well known lack of memory of the author, a great effort will be done in this section in order to break some tradition and (try to) name who (person or group) has to be mentioned. Nevertheless, my deeply apologies for possible mistakes and oversights.

Anne, you have been a unreplaceable guide and advisor during my PhD project. Your presence (actual or by phone) and experience in the lab was very important. Although sometimes very tough, your accuracy in presenting the work thought me a lot. Thank you very much. Mark, the enthusiasm you showed was always very important for me, as much as your sincere curiosity and you questions (always right to the point). Thanks for your precious suggestions and guidance. Thanks to both of you for proof-reading this manuscript.

Gianni, Huy and Fendy, with you guys the group was a enjoyable *'gabbia di matti'*. Overworking was never heavy when you were around. I happy you all found your own way now. Meena, thanks for being such a wonderful office mate and friend. Thanks to Maitreyi and Uttam as well, you guys are a wonderful family. Erik, kleine broertje, the best keyboard-head-banging-physicist, aka 'the kid' when Meena and I were talking about you, thanks for your calm sarcasm and your consistency in sandwiches. Leonid and Dennis, it was short but I am glad to have met you when I started my PhD. Chiron and Nick, thanks for being the fresh wind of the group. Takashi, I learned a lot with you and your precious pressure cell (and with the delicious and funny-looking Japanese food). Thanks to the extended group for the good time during the weekly group meetings on Wednesdays. The "under-40-question-time", although sometimes silent, was really helpful, as much as the comments and questions. Thanks to Jeroen, Freek, Sanne, Thuy, Stan, Iman, Wing Kiu, Jesse, Anton, Marco, Rein, Jesse, Jochem, Erik, Huib. Jacques, your specific heat system is amazing, I was lucky to experience you affection to it. Thanks to Ying Kai for making all the single crystals used in this thesis work and for the useful discussion about crystal growing and Chinese culture, as much as for passionately discovering Beijing and Shenyang together with a group of curios western physicists.

Thanks to Prof. von Lönheysen and his group at the University of Karlsruhe, for taking me as a visiting member of their group. Thanks to Pau and Carles, my cheerful flatmates in Germany. Thanks to Frank de Boer and all the China group, for unforgettable great time, and to the Chinese universities in Shenyang and Beijing for their amazing hospitality.

Thanks to the WZI Workshops (Technologie Centrum UvA), to Wim, Cees, Joost, Johan and the Instrumentmakerij, to Ron, Matthijs and the Ontwerp centrum, to Hans, Ben (my programming guru), Frans, Piet, Johan and the Elektronica team, always ready to help and solve problems, as well as to answer my (sometimes silly) questions. To the WZI technicians, Bert, Ton G., Ben, Willem, Hugo, Ton R. and Gertjan, thanks for your kind help. Moreover, thanks a lot for coffee breaks, insights in the Dutch culture, discussion about sailing and photography. Thanks to Renè for ordering helium (even when I was late with emailing). Thanks to the WZI management, Mariet, Rita, Ineke, Luuk, and to the FOM people. Thanks to Harry Linders, your moral and technical support was important, every FOM student should have the opportunity to count upon your help. To the students of the thermal physics classes and Gerard, thanks, I learned a lot! To Dini and Dirk, always smiling at the front door. Thanks to the WZI and ITFA Social clubs, I enjoyed organizing events, and to Joost, the bier man, and Richard, for fun time when

shopping in Hanos.

Of course many other people from WZI and ITFA contributed to make lunch/coffee/tea/dinner/party/conference/holiday a nice time at the UvA: Ekkes, Cam Thanh, Trung, Ou, Lian, Tom, Wieteke, Ha, Dolf, Saba, Kateřina, Vinh, Manuel, Henk, Daniel, Peter, Rudolf, Tracy, Javier, Oleg, Abdoulaye, Kinga, Antina, VJ, Mounir, Sanli , Duc, Sebastian, Tom, Tobias, Jan-Joris, Carolijn, Antje, Piotr, Srdjan, Mischa, Rob, Raoul, David, Jérémie, Gerardo (and his scooter at the world cup semifinal), Raoul, Liza, Bahar, Johannes, Alex, Xerxes, J-S, Ingmar, Keiichi, Sheer, Amir, Marco (for accomplishing the mission), João, Thomas, Sasha. Thanks to the head of the institutes, Mark and Kareljan, for the intense table tennis final match WZI-ITFA.

Thanks to the NKI group (Jan-Jakob, Marcel and all my current colleagues), I am glad I can be part of such a highly scientific as well as incredibly amusing working environment. Bedankt aan mijn kamergenoot Johan, die altjid de moeite neemt om Nederlands tegen mij te praten. Thanks to the italian coffee company (Yenny, Edo, Alize, Angelo, Maddalena) for their constant (not only caffeine related) support and fun activities.

In order of appearance: Salvo, you know always the most right and the most wrong thing to tell me at the moment. I miss our five-minutes arguments for meaningless reasons. Balt, whose office was the best chocolate-hiding-place and who was always a good excuse for tea break, especially the final rush of this thesis would not have been so much fun without you. Thanks for soften that pressure and for letting me bother you at any time. Paolino, thanks for monopolizing our phone calls, how would I do without our endless chats? You have always been there to support me. Richard, bla-bla-bla, the best BE-vocabulary-beer-drinker, thanks for letting me un-collect your atoms, for reminding me to thank you and for proving that also a British guy can cook (but will not bake cakes). Some of you guys are (or will soon be) away from Amsterdam. Maybe it is how is supposed to be, maybe I should see it as an opportunity for travelling a lot.

In Amsterdam there are the best conditions/friends for parties, dinner, Friday beers, cooking Sundays, festivals, barbecues, improvised pic-nics, random meetings and whatever else. Needless to say, these helped the author to rest after a day in the lab or provided motivation for a fruitful working day-after. Irene, the paranimf colleague, we made it!, Bea for helping me with your sweetness, Mario perché ci abbiamo creduto, Luana you always have a thought, Yenny for biking in the rain but getting my bike lights, Kuba for your polish-texan pierogi, Sara thanks for your contagious smile, Pasquale for knowing more than the devil, Nancy for your graceful dancing skills, Kara for the flat tires.

Using a peculiar random name collection program (my memory), thanks to: Carlo, Salima, Nazly, Nacho with his Italian from the 19th century, Mirandita (ms. Hula Hoop), PG (materassino rosa), Manu, Diego, Beike, Alessandro, Paola, Nanda, Merolli, Yuri, Lianne, Dave, Samia, Valeriu, Atakan and all the API people, Silvia de Roma la cara vicina, the flatmate Phil (or how I learned to catch a frisbee), Suchitra, the invited speaker/crazy backpacker, Alessandro&Marieke and EdoSil for the cooking sessions, Alessandra, Sandra SLVM, Agata, Stefano lo Sbocconi (who should play the bass), Michele, Fabrizio G., Yulia, lo ZZio, Andrea, Laurè, Martijn, Annemarieke, Jordi, Alessandro V., Fabrizio M. and the chemists, Sher, Francesca, Emiliano, Fabio, Gianluigi (and the guitar player from Capossela), Karol, Tommaso, Stefania, Fangni, Paulus, Jean-Louis and his parachutist suite, Viney, Francesca, Gerda, Martine, Franco, Verena, Tora, Stefania's, Sergio and the dutch-time with the prof, Vero, ... Life (or work) might bring us more or less further apart, but we always create the conditions to meet. This means a lot to me.

Thanks to the Oosterpark Thai chi class (Sifu Chan, Simu and all the crew) for teaching me thai chi and much more. To the football guys, for good time in the field and in front of a beer. A bit back in time: thanks to the Maranteghe group (Angi, Benny, Ela, Ele, Eli, Mara, Vale, e consorti) which is now spread around Europe but still manages to be loud and have *grasse risate* every time and everywhere. For the last twenty years (or in graspa style 20 ± 8) you have been the best antidepressant and effective 'belly exercise'. Thanks to my teachers, Dinelli, Fiorin and Martella, things are more clear now. Thanks to the Marcon crew that did not forget me, even though things have changed. Thanks to the D&D and *vampiri* crew, your Amsterdam invasions are always appreciated. Thanks to the president and the P.A.P.A., and to my university-mates in Padova. Thanks to my italian neighbours, Sissi, Lucia and Ricki (the bro), we shared a lot.

This thesis is dedicated to my family, for their strong support and their interest, in their own way. Ai miei genitori, che mi hanno sempre lasciato scegliere la mia strada e mi hanno insegnato molto piú di quel che credono. Grazie papà per aver guardato tutta la tesi con interesse, grazie mamma per aver fatto il tifo per me ad ogni passo. A Vale, the only person that can get on my nerves and that I deeply appreciate, grazie sorellina, anche per la tua super organizzazione. Alla zia Fausta, a Fabio Monica e Eugenia, a Pino Deicy Gabriella Marco e Nana, agli zii Lalli e Franco. E ovviamente anche ai miei adoratissimi nonni Bruno e Rosaria, Gino e Anna, al caro zio Oscar e alla dolce Nadia.

Ik zou ook de familie van Fendy van harte willen danken. Jullie zijn altijd zo lief en vol van aandacht met mij, ik voel net als ik bij mijn zelfe familie

ben. And, Fendy, here you are again. Thanks for your stupidity [181] and your (sometimes very focused) enthusiasm. Thanks for bearing with me and not letting me go in the last year, it was important. Thanks for showing me home and a different way of being.

Citations

First page: Looked up from below, from this new prospective, the olive tree seemed to him to be bigger and more tangled. He saw the complexity of branches he could not see before from within (detective Montalbano, sitting for once outside its beloved *olivo saraceno*).

Chapter 2: No ladies and gentlemen. According to me, I am the one you believe I am (from *So it is (if you like it)*).

Chapter 3: Their ideas walk on our legs (commemorative poster for judges G. Falcone and P. Borsellino, killed in 1992).

Chapter 5: the revisited laboratory is source of joy and radiate an intense charm (from *The periodic table*, Uranium).

Chapter 6: so every right thing reveals its opposite.